



UNIVERSITÀ  
DEGLI STUDI  
FIRENZE

UNIVERSITÀ DEGLI STUDI DI FIRENZE  
DIPARTIMENTO DI INGEGNERIA DELL'INFORMAZIONE (DINFO)  
CORSO DI DOTTORATO IN INGEGNERIA DELL'INFORMAZIONE  
CURRICULUM: ELECTRONICS AND ELECTROMAGNETISM ENGINEERING

---

ADVANCED 2D/3D IMAGING TECHNIQUES  
FOR ISAR AND GBSAR

*Candidate*

Rojhani Neda

*Supervisor*

Prof. Pieraccini Massimiliano

*PhD Coordinator*

Prof. Chisci Luigi

---

CICLO XXXI, 2015-2018

Università degli Studi di Firenze, Dipartimento di Ingegneria  
dell'Informazione (DINFO).

Thesis submitted in partial fulfillment of the requirements for the degree of  
Doctor of Philosophy in Information Engineering. Copyright © 2019 by  
Rojhani Neda.

*October 2018*

## Acknowledgments

I would like to express my sincere gratitude to my supervisor, Prof. Massimiliano Pieraccini, for sincere guidance, encouragement, and advice he has provided throughout my time as his student. I have been extremely lucky to have a supervisor who cared so much about my work, and who responded to my questions and queries so promptly. In particular, I would like to thank all members and my colleague of the Radar System Design (RSD-LAB) who were of great help during my research. Here, I would like to thank my coordinator Prof. Luigi Chisci for his kind support during my research, as well as I would like to thank the Department of Engineering of Information (DINFO) providing the funding which allowed me to undertake this research, but also for giving me the opportunity to attend conferences and meet so many interesting people. In addition, I would like to extend my warmest thank to my special friend who supported me during these years.

Finally, My thanks go to my parents and siblings for their confidence and their love during all these years. They have always supported me and helped me overcome the difficulties without complaining.

# Contents

<b>Contents</b>	<b>v</b>
<b>1 Introduction</b>	<b>1</b>
1.1 Objective . . . . .	1
1.2 Contributions . . . . .	5
<b>2 Radar Overview</b>	<b>9</b>
2.1 Definition of Radar . . . . .	9
2.2 Radar Block Diagram . . . . .	10
2.3 Radar Classifications . . . . .	11
2.4 Radar Equation . . . . .	12
2.5 Radar Frequencies . . . . .	14
<b>3 Radar Cross Section of Quadcopter and Its Basic Theory</b>	<b>17</b>
3.1 Definition Of Radar Cross Section . . . . .	18
3.2 RCS Dependence on Sight Angle and Frequency . . . . .	20
3.3 Target Scattering Matrix . . . . .	21
3.4 RCS of Simple Form Objects . . . . .	24
3.5 RCS of Complex form Objects . . . . .	24
3.6 RCS Fluctuation and Statistical Models . . . . .	26
3.6.1 Swerling I Target . . . . .	27
3.6.2 Swerling II Target . . . . .	27
3.6.3 Swerling III Target . . . . .	27
3.6.4 Swerling IV Target . . . . .	28
3.6.5 Swerling V Target . . . . .	28
3.7 Relationship Between RCS and Inverse Synthetic Aperture Radar . . . . .	28
3.8 RCS Measurement . . . . .	29

3.9	Conclusion . . . . .	35
<b>4</b>	<b>2D And 3D Inverse Synthetic Aperture Radar Imaging of a Small Quadcopter and Its Basic Concepts</b>	<b>37</b>
4.1	Synthetic Aperture Radar (SAR) and Inverse Synthetic Aperture Radar (ISAR) Concepts . . . . .	38
4.2	The Relation of Electromagnetic (EM) Scattering Field to the Image Function in ISAR . . . . .	41
4.3	Point Spread Function in ISAR Imaging . . . . .	43
4.4	ISAR Imaging Resolution . . . . .	43
4.4.1	Range Resolution . . . . .	44
4.4.2	Cross-Range Resolution . . . . .	44
4.5	Two-Dimensional ISAR Image Processing . . . . .	44
4.6	Three-Dimensional ISAR Image Processing . . . . .	48
4.7	The Measurement Equipment . . . . .	51
4.8	The UAV under Test . . . . .	52
4.9	Two-Dimensional ISAR Result . . . . .	53
4.10	Three-Dimensional ISAR Result . . . . .	56
4.11	Aperture windowing . . . . .	57
4.12	Conclusion . . . . .	61
<b>5</b>	<b>Bistatic 3D Ground Based Synthetic Aperture Radar</b>	<b>63</b>
5.1	Synthetic Aperture Radar (SAR) and SAR Geometry . . . . .	63
5.2	Ground Based Synthetic Aperture Radar . . . . .	64
5.3	Bistatic SAR and Bistatic SAR Geometry . . . . .	65
5.4	Bistatic Radar Equation . . . . .	65
5.5	The Bistatic GB-SAR Working Principle . . . . .	66
5.6	Bistatic Range and Cross-Range Resolution . . . . .	67
5.7	Radar Interferometry . . . . .	69
5.8	The Bistatic Focusing Algorithm . . . . .	71
5.9	The Bistatic Radar Prototype . . . . .	73
5.10	Experimental Test . . . . .	74
5.11	Conclusion . . . . .	82
<b>6</b>	<b>Compressive Sensing Applied To Ground Based Synthetic Aperture Radar</b>	<b>83</b>
6.1	Shannon-Nyquist theorem . . . . .	83
6.2	Compressive Sensing . . . . .	84

---

6.2.1	Sparsity and Compressible Signals . . . . .	84
6.2.2	Incoherence . . . . .	85
6.3	Compressive Sensing Algorithm . . . . .	86
6.3.1	Basis Matrix . . . . .	87
6.3.1.1	Wavelet Families . . . . .	87
6.3.2	Measurement Matrix . . . . .	90
6.3.3	Compressive Sensing Recovery Algorithm . . . . .	91
6.3.3.1	$l_1$ -Minimization . . . . .	92
6.3.3.2	Orthogonal Matching Pursuit (OMP) . . . . .	92
6.4	Compressive Sensing Applied To Radar . . . . .	95
6.5	Implementation of Compressive Sensing to SAR Imaging . . . . .	95
6.6	The radar prototype . . . . .	96
6.7	The CS Theory and Focusing Algorithm . . . . .	97
6.8	Experimental Test . . . . .	98
6.9	Conclusion . . . . .	118
<b>7</b>	<b>Conclusion</b>	<b>119</b>
<b>A</b>	<b>Publications</b>	<b>121</b>
	<b>Bibliography</b>	<b>123</b>





# Chapter 1

## Introduction

### 1.1 Objective

The term “remote sensing”, first used in the United States in the 1950s by Ms. Evelyn Pruitt of the U.S. Office of Naval Research. In general, the word remote sensing is used for the acquisition of information about an object or phenomenon without making physical contact with the object and thus in contrast to on-site observation. Remote sensing is used in numerous fields, including geography, land surveying, hydrology, ecology, oceanography, glaciology, geology, military, intelligence, commercial, economic, planning, and humanitarian applications. The instruments involved in remote sensing science can be divided into two groups: (1) passive known as radiometers and (2) active known as radars. In an active case, a signal is emitted by a satellite or aircraft and its reflection by the object is detected by the sensor and in the passive case, the radiation emitted by the object being observed. The popular and the most attractive active sensor is Radar. The word radar is an abbreviation for Radio Detection and Ranging, where the time delay between emission and return is measured, establishing the location, speed, and direction of an object. Radar is capable of detecting, tracking and imaging targets with high accuracy at long range distance, day and night, and in all-weather condition. Mainly because of these reasons, radar has been widely used for military and civil purposes, such as, surveillance, air defense and weapon control, high-resolution imaging, remote sensing of the environment, weather and earth observation, air traffic control, vehicle collision avoidance and cruise control, harbor and river traffic surveillance, and industry automation. Synthetic-aperture radar (SAR) is a

form of radar that is used to create two- or three-dimensional images of objects, such as landscapes. SAR is typically mounted on a moving platform, such as an aircraft or spacecraft, and has its origins in an advanced form of side-looking airborne radar. The distance the SAR device travels over a target in the time taken for the radar pulses to return to the antenna creates the large synthetic antenna aperture (the size of the antenna). Typically, the larger aperture, the higher image resolution will be, regardless of whether the aperture is physical (a large antenna) or synthetic (a moving antenna) –this allows SAR to create high-resolution images with comparatively small physical antennas. Radars can be classified as ground-based, airborne, space borne, or ship-based radar systems. During my Ph.D. course I have been working on ground based radars. In the course of my work, I have been involved in Ground-based synthetic aperture radar (GB-SAR), Inverse synthetic aperture radar (ISAR), Ground penetrating radar (GPR), and using compressive sensing for GB-SAR and GPR. Besides, I have worked on another topic that depends on radar field such as: designing antenna for GPR radar.

#### **Ground-Based Synthetic Aperture Radar(GB-SAR):**

Ground-based synthetic aperture radar (GB-SAR) systems are popular remote sensing instruments operated on the ground to obtain high-resolution 2D images. A linear GB-SAR with transmitting and receiving antennas uses the movement of an antenna along a linear rail for synthesizing a large aperture. GB-SAR is used for detecting small displacements of large structures as bridges, dams. These radars capable of detecting the displacement only in a long range direction.

#### **Inverse synthetic Aperture Radar(ISAR):**

Inverse Synthetic Aperture Radar (ISAR) is a radar technique using radar imaging to generate a 2D high-resolution image of a target. ISAR utilizes the rotation of target for synthesizing a high-resolution image while the radar remains stationary. Images of the target region produced by ISAR can be a useful tool in locating scattering regions on the target. ISAR images are often produced by rotating the target and processing the resultant Doppler histories of the scattering centers. If the target rotates in azimuth at a constant rate through a 'small' angle, scatterers will approach or recede from the radar at a rate depending only on the cross range position- the distance

normal to the radar line of sight with the origin at the target axis of rotation. For small angles, an ISAR image is the 2-dimensional Fourier transform of the received signal as a function of frequency and target aspect angle. If the target is rotated through 'large' angles, the Doppler frequency history of a scatterer becomes non-linear, following a sine-wave trajectory.

**Ground penetrating radar (GPR):**

Ground Penetrating Radar (GPR) investigates the subsurface and detects buried objects using electromagnetic wave. The ground penetrating radar system is a nondestructive method which works by sending a pulse of energy into a material such as concrete and recording the strength and the time required for the return of any reflected signal. GPR uses high-frequency radio waves, usually in the range 10 MHz to 2.6 GHz.

**Antenna design for Ground penetrating radar:**

Various antennas are used in GPR application such as the horn antenna. In GPR application the antenna is close to the ground. This is a difficult limitation in their design. There is a trade-off between the penetration depth and desirable resolution with the operative band of an antenna which works in GPR radars. It means that the GPR radars have more penetration depth at low frequencies but the possible problem is the big size of the antenna. Therefore, the aim of this study was designing a small size horn antenna with a low-cut off frequency.

**Compressive Sensing (CS):**

Compressive sensing is a common process in many aspects of modern life. The Shannon/ Nyquist theorem is the basis for sampling signals or images, through which the sampling rate should be at least twice the maximum frequency available in its bandwidth. CS, however, is a new approach which promises to recover images and signals from a small number of random samples or measurements data better than the traditional way. Compressive sensing is able to compress data when the signal is sparse.

This Ph.D. thesis is only focused on some of these topics. These selected topics concentrate exactly on radar imaging, which is in along the lines of the research subject of the Ph.D. candidate. Furthermore, the innovations in both radar configuration and radar processing methods are the bases of

these topics, which are presented in detail in separate chapters. While in the subject of ground penetrating radar(GPR) the activity which has done is focused on the technology of this kind of radar and its equipment such as its antenna. Hence, this thesis is as follows:

**Chapter 1:** The concept of the radar system has been introduced based on radar block diagram. As well as, there are discussions about radar equation, radar classification, and frequency of radar.

**Chapter 2:** The fundamentals of radar cross-section have been presented. Afterward, the RCS of two quadcopters is estimated by Electromagnetic Simulation Software (FEKO). In order to confirm the work, the real measurement results which are computed by Inverse synthetic radar (ISAR) has been provided.

**Chapter 3:** The 2D and 3D inverse synthetic aperture radar (ISAR) image processing has been carried out for imaging small UAVs. The two-dimensional (2D) ISAR image is made by collecting scattered fields from different angles, while a 3D image can be measured by integrating backscatter data in two spatial coordinates of the 2D aperture (cross-range in azimuth and elevation). Another topic that has been introduced is windowing in ISAR. In Synthetic Aperture Radar (SAR) processing the windowing in range and cross-range is a standard and its aim is to reduce the side-lobes of the Point Spread Function. In ISAR when the rotation is smaller than  $180^\circ$ , the aperture windowing does not cause any estimation problems; it works exactly as for standard SAR. Problems occur when the rotation angle exceeds the  $180^\circ$  and especially when the rotation is complete. So for improving cross-range resolution in ISAR a new technique has been proposed, before focusing the rotation circle should be divided into 4 arcs of  $180^\circ$ , and a Kaiser window is applied on the chords of each of the arcs separately. Finally, the 4 resulting images are combined into one image.

**Chapter 4:** A new GBSAR system has been presented, that is capable of generating both monostatic and bistatic images. Whereas the bistatic images need several hours to prepare the 3D information, the monostatic images are acquired in a few minutes by providing only 2D information about the targets in its field of view. Accordingly, the 3D measurement in conven-

tional SAR radars is a computationally complex and time-consuming process but they can be interesting when the radar is used to image in a complex scenario. Due to this structure, it is able to create two images taken from different points of view with respect to the antenna system along an x-axis and the second channel along the z-axis. A superior advantage of proposed radar is that it can be operated as 2D interferometric images for each horizontal scan, moreover by varying the second channel height the 3D images are produced. It is worth mentioning that as a 3D image is obtained in bistatic condition, the angular resolution is worse of factor two with respect to a monostatic radar that scans a plate.

**Chapter 5:** All concepts of compressive sensing have been discussed. The types of basic matrix and recovery methods are presented. Finally, the use of the CS algorithm in the real scenario is carried out based on three different data. The first test is carried out with a corner reflector (CAR) in front of the radar, the second one is performed for a seven-story building, and the last one is accomplished in a natural scenario which is conducted on the "Belvedere Glacier" that located on Alpine mountains.

## 1.2 Contributions

### *Conference Proceedings*

- **Rojhani N.**, Pieraccini M., Sarbazi Golazari S., "A Compact TEM Horn Antenna for Ground Penetrating Radar", IEEE ICACCI-18 IEEE International Conference on Advances in Computing, Communications Informatics,2018.
- Pieraccini M.,**Rojhani N.**, Miccinesi L., "Ground Based Synthetic Aperture Radar with 3D Imaging Capability", 15th European Radar Conference, EuRAD-2018.
- Miccinesi L.,**Rojhani N.**, Pieraccini M., "Compressive Sensing for No-Contact 3D Ground Penetrating Radar", 2018 41st International Conference on Telecommunications and Signal Processing (TSP), Athens, Greece,August-2018.
- Pieraccini M., **Rojhani N.**, "Testing of bridges and towers through interferometric radar", 3rd International and 7th National Conference on Modern Materials and Structures in Civil Engineering, Iran-2018.

- Pieraccini M., Miccinesi L., **Rojhani N.**, “Comparison between Horn and Bow-tie Antennas for Through-the-Wall Applications”, 2018 IEEE Conference on Antenna Measurements Applications (CAMA)-2018.
- Pieraccini M., Miccinesi L., **Rojhani N.**, “A free-space technique for measuring the complex dielectric constant of sawdust”, 2018 IEEE Conference on Antenna Measurements Applications (CAMA)-2018.
- **Rojhani N.**, Sarbazi Golazari S., Nasrin Amiri., Farrokh Hojjat Kashani., “CPW-Fed Circular Polarized Square Slot Antenna for GPS Applications”, 2018 IEEE International RF and Microwave Conference (RFM)-2018.
- Pieraccini M., **Rojhani N.**, Miccinesi L., “Comparison between horn and bow-tie antennas for Ground Penetrating Radar”, 9th international workshop on advanced ground penetrating radar, IWAGPR 2017, July 2017.
- Pieraccini M., **Rojhani N.**, Miccinesi L., “2D and 3D-ISAR Images of a Small Quadcopter”, 14th European Radar Conference, EuRAD 2017.
- Pieraccini M., **Rojhani N.**, Miccinesi L., “Ground Penetrating Radar with Contact Horn Antennas”, proceeding at 32nd URSI GASS, Montreal, August 2017, conference abstract.
- Sarbazi Golazari S., **Rojhani N.**, Amiri N., “Multiband low profile printed monopole antenna for future 5G wireless application with DGS”, 2017 IEEE 4th International Conference on Knowledge-Based Engineering and Innovation (KBEL), December 2017.

### *Journal papers*

- Pieraccini M., **Rojhani N.**, Miccinesi L., “Compressive Sensing for Ground Based Synthetic Aperture Radar”, Remote Sensing, 2018.
- Pieraccini M., Miccinesi L., **Rojhani N.** “A GBSAR Operating in Monostatic and Bistatic Modalities for Displacement Vector”, IEEE Geoscience and Remote Sensing Letters, July 2017.
- Pieraccini M., Miccinesi L., **Rojhani N.** “RCS and ISAR of small UAVs”, IEEE Aerospace and Electronic Systems Magazine, September 2017.

*Patent*

- Radar ad apertura sintetica basato a terra (GBSAR) con antenne multiple in trasmissione e ricezione (MIMO) e facente uso della tecnica di elaborazione detta Compressive Sensing (CS), [ numero di brevetto per invenzione : n. 10201800006797].
- Radar Terrestre Tridimensionale Interferometrico ad Apertura Sintetica, [numero di brevetto per invenzione : n.102017000145769].





# Chapter 2

## Radar Overview

*Radar is an electromagnetic system that uses radio waves to determine the range, angle, or speed of objects. It can be used to detect aircraft, ships, spacecraft, motor vehicles, weather formations, and natural environment. In fact, the radar abbreviation stands for “radio detection and ranging”. Modern radars are advanced transducer/computer systems that not only detect targets and determine the target range, but also track, identify, image, and classify targets while repressing potentially unwanted interference like a reflection from the environment (known as clutter) and countermeasures (jamming). A radar system includes a transmitter that generates an electromagnetic wave in the radio or microwaves range, a transmitting antenna, a receiving antenna (often the same antenna for transmitting and receiving), and a receiver and a processor to determine the properties of the objects. Radio waves (pulses or continuous) which are reflected from a transmitter and coming back to the receiver, provide some information about the location and speed of the target.*

### 2.1 Definition of Radar

A radar is an electrical device that operates by radiating electromagnetic energy and detecting the echo returned from reflecting objects (targets). The echo signal provides information about the target. Range or distance to the

target is found by the time when radiation energy travels to the target and the rear. The angular position of the target is found with an antenna (one with a narrow beam width) to sense the angle of arrival of the echo signal. If the target is moving, a radar can find its path or trajectory and anticipate the future position. Radar can discriminate moving targets (such as aircraft) from stationary targets (likes land and sea clutter) by Doppler shift. The stationary echo may be many orders of magnitude greater than the moving target. Operating at a high enough resolution, a radar can gather information about the size and shape of the target. Radar resolution can be obtained from either range or angle or both. Range resolution needs a large bandwidth. Angular resolution needs large antennas. Usually, the resolution in cross-range direction is not as good as the resolution along the range. When there is a relative movement between the individual components of a target and the radar, it is possible to use the inherent resolution of the Doppler frequency, for resolving the cross-range resolution. The cross range resolution in SAR radar during the imaging of scenario, such as the ground, can be measured due to resolution in Doppler, Even though a SAR is a technique to generate a large "synthetic" antenna by storing an echo signal. Hence, the synthetic antenna and Doppler resolution are synonymous.

The Doppler resolution is a natural way of acquiring the cross-range resolution which is obtained by the inverse aperture radar (ISAR) applied to generate an image of a target. Radar can detect fairly small targets at near or far distances. It can accurately measure the range of targets in all weather, which is a major advantage compared to other sensors. Initially, the radar was developed to meet the military's requirements for surveillance and weapons control, but most recently radar has been seen as a significant civilian equipment for the safe flight of aircraft, ships, and spacecraft; the remote sensing of the environment, particularly the climate; and law enforcement and many other programs [1].

## 2.2 Radar Block Diagram

The basic components of a radar are demonstrated in the simple chart of Figure 2.1, With regard to the radar block diagram, a radar consists of the following components: Transmitter and Receiver part, Oscillator, Duplexer, Antenna, Mixer, Amplifier and Matched Filter.

The radar signal, commonly a repetitive part of a short pulse, is produced by the transmitter antenna and radiated into space. The duplexer allows to a

single antenna to be time-shared for both transmission and receiver antenna. Targets reflect a part of the radar signal and return a small amount of it into the radar direction. The echo signal is gathered by the radar antenna and amplified by the receiver. Detection of a target occurs if the output of the radar receiver is large enough. Generally, a radar can determine the position of a target in range and azimuth direction, but the echo signal can provide other information about the nature of the target. The output of the receiver is presented on a display to an operator which makes the decision as to whether or not a target exists. Otherwise, the receiver output can be automatically processed by electronic means to detect the presence of the target or to establish a track of the target [2].

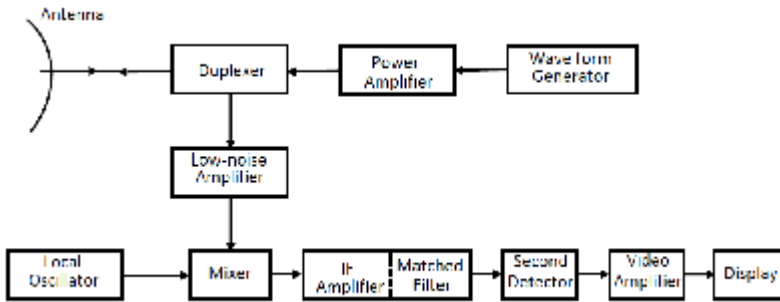


Figure 2.1: A simple block diagram of a radar

### 2.3 Radar Classifications

Radars have different categorizations. The first classification is according to their location such as arranged as ground-based, airborne, space borne, or ship-based radar systems. The second classification is based on the specific radar characteristics, such as the frequency band, type of antenna and waveforms utilized. Another classification that is available is radar mission or its functionality, such as weather, acquisition and search, tracking, track-while-scan, fire control, early warning, over the horizon, terrain following, and terrain avoidance radars. One of the important classifications of radars is based on waveform types which they use or by their operating frequency. With regard to the waveforms, radars can be divided into Continuous Wave

(CW) or Pulsed Radars (PR). CW radars are those that continuously broadcast electromagnetic energy and the echo signal is received and processed constantly. Unmodulated CW radars can accurately measure target radial velocity (Doppler shift) and angular position. Pulsed radars use a string of pulsed waveforms (mainly with modulation). In this class, radar systems can be categorized on the basis of the Pulse Repetition Frequency (PRF), as low PRF, medium PRF, and high PRF radars. High PRF radars are mostly used to measure target speed. Low PRF radars are primarily used for ranging where target velocity (Doppler shift) is not of desired. Continuous wave, as well as pulsed radars, can measure both targets range and radial velocity by employing different modulation scheme [3].

## 2.4 Radar Equation

The radar equation is related to the range of a radar and the characteristics of the transmitter and receiver antenna, target, and environment. It is useful not only for determining the maximum range that a particular radar can identify a target but also it can serve as a means for understanding the factors affecting radar performance. It is also an important tool to help design a radar system. When the transmitter power  $P_t$  is radiated by an isotropic antenna, the power density at a distance  $R$  from the radar is equal to the radiated power divided by the surface area  $4\pi R^2$  of an imaginary sphere of radius  $R$  and it can express as follow. It has units of watts per square meter:

$$\text{Power density at range } R \text{ from an isotropic antenna} = \frac{P_t}{4\pi R^2} \quad (2.1)$$

Radars use the directive antennas (with narrow beam-widths) to concentrate the radiated power  $P_t$  in a specific direction. The gain of an antenna is a measure of the increased power density which is radiated in some direction as compared to the power density that would appear in that direction from an isotropic antenna. The maximum gain  $G$  of an antenna may be defined as below:

$$G = \frac{\text{maximum power density radiated by a directive antenna}}{\text{power density radiated by a lossless isotropic antenna with the same power input}} \quad (2.2)$$

Therefore, the power density at the target from a directive antenna with a

transmitting gain  $G$  is computed as follows:

$$\text{Power density at range } R \text{ from a directive antenna} = \frac{P_t G}{4\pi R^2} \quad (2.3)$$

The target intercepts a part of the incident signal and re-radiates it in different directions. It is only the power density re-radiated in the direction of the radar (the echo signal) which is desired. The power density returned to the radar for a specific power density which transmits to the target is determined by a radar cross section (RCS) of a target. It is indicated by  $\sigma$  and is mostly named, with brief, target cross-section, radar cross section or simply cross-section. The radar cross section is illustrated by the following equation:

$$\text{Reradiated power density back at the radar} = \frac{P_t G}{4\pi R^2} \cdot \frac{\sigma}{4\pi R^2} \quad (2.4)$$

The RCS has a unit of area. It can be misleading to use the radar cross section directly with the target's physical size. Radar cross section is more dependent on the shape of the target than on its physical size. The radar antenna receives a part of the echo energy incident on it. The power received by the radar is obtained as an incident power density product of the effective area  $A_e$  of the receiving antenna. The effective area is dependent on the physical area  $A$  by the relationship  $A_e = \rho_a A$  where  $\rho_a$  denotes antenna aperture efficiency. The received signal power  $P_r$  (watts) is as follows:

$$P_r = \frac{P_t G}{4\pi R^2} \cdot \frac{\sigma}{4\pi R^2} \cdot A_e = \frac{P_t G A_e \sigma}{(4\pi)^2 R^4} \quad (2.5)$$

The distance beyond which the target cannot be detected is defined as the maximum range of a radar ( $R_{\max}$ ). It occurs when the received signal power  $P_r$  just equals the minimum detectable signal  $S_{\min}$ . Substituting  $S_{\min} = P_r$  in Eq.2.5 causes to write the  $R_{\max}$  as follows:

$$R_{\max} = \left[ \frac{P_t G A_e \sigma}{((4\pi)^2 S_{\min})} \right]^{\frac{1}{4}} \quad (2.6)$$

It is the basic form of the radar range equation. The significant antenna parameters are the transmitting gain and the receiving effective area. The transmitting power  $P_t$  has not been determined as either the average or the peak power. It depends on how  $S_{\min}$  is determined. In this data, however,

$P_t$  indicates the peak power. Antenna theory shows the relation between the transmitting gain  $G$  and the receiving effective area  $A$  as follows:

$$G = \frac{4\pi A_e}{\lambda^2} = \frac{4\pi \rho_a A}{\lambda^2} \quad (2.7)$$

Where  $\lambda$  denotes wavelength which is  $\lambda = \frac{c}{f}$ .  $c$  denotes the speed of propagation and  $f$  denotes frequency. Eq.2.7 can be substituted in Eq.2.6 for both  $A_e$  and  $G$ , to obtain [1]:

$$R_{\max} = \left[ \frac{P_t G^2 \lambda^2 \sigma}{(4\pi)^3 S_{\min}} \right]^{\frac{1}{4}} \quad (2.8)$$

## 2.5 Radar Frequencies

Any device that detects a target by radiating electromagnetic energy and uses an echo scattered from a target can be classified as a radar regardless of its frequency. Nevertheless, commonly radars operate at frequencies from a few megahertz to a few Terahertz. The basic principles at each frequency are the same, but practical implementation is very different. Traditional radar generally acts in what is named the microwave zone, but there are significant exceptions. Radar operates at frequencies ranging from 100 MHz to 36 GHz, which covers more than eight octaves. Operational HF over the horizon radars acts at frequencies as low as a few megahertz. At the other end of the spectrum. Experimental millimeter wave radars have been at frequencies higher than 240 GHz. During World War II, letters codes such as *S*, *X*, and *L* were used to determine the distinctive frequency band in which the microwave radar was in development. The main aim was to maintain military confidentiality, but after the war, naming letters continued as a convenient shorthand -term to readily indicate the area of the spectrum at which a radar operated. Table I shows the list of radar frequency bands that are approved as IEEE standards. Figure 2.2, demonstrates the typical frequency range of radar where it operates, in the electromagnetic spectrum [1]. It should be noted that the radar frequency range is also one of the characteristics of radar classification. In Table 2.1, radar classifications are shown based on the frequency of operation.

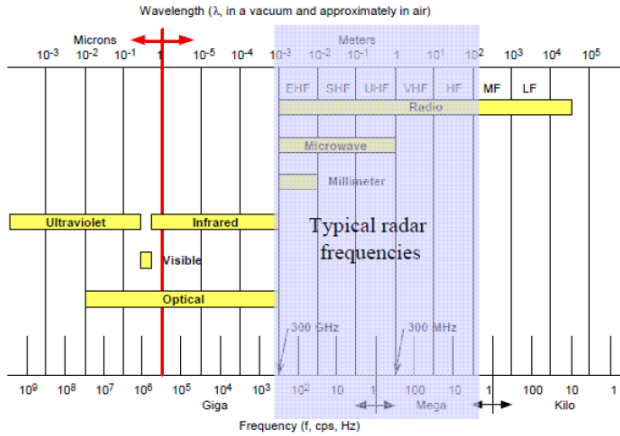


Figure 2.2: Electromagnetic Spectrum

Table 2.1: Radar frequency bands

Letter designation	Nominal Frequency Range	Specific Frequency Ranges for Radar based on ITU
HF	3-30 MHz	
VHF	30-300 MHz	138-144 MHz ; 216-225 MHz
UHF	300-1000MHz	420-450 MHz ; 850-942 MHz
L-band	1-2 GHz	1215-1400
S-band	2-4 GHz	2300-2500 MHz ; 2700-3700 MHz
C-band	4-8 GHz	5250-5925 MHz
X-band	8-12 GHz	8500-10.680 MHz
Ku-band	12-18 GHz	13.4-14 GHz ; 15.7-17.7 GHz
K-band	18-27 GHz	24.05-24.25 GHz
Ka-band	27-40 GHz	33.4-36 GHz
V	40-75 GHz	59-64 GHz
W	75-110 GHz	76-81 GHz ; 92-100 GHz
mm	110-300 GHz	126-142 GHz ; 144-149 GHz ; 231-235 GHz ; 238-248 GHz





# Chapter 3

## Radars Cross Section of Quadcopter and Its Basic Theory

*The radar cross section (RCS) characterizes the scattering properties of a radar's target. RCS depends on the size of a target and its ability to reflect radar signal. It has a unit of square meters  $m^2$ . The RCS area is not a physical area, but an evaluation of a target's ability to reflect radar signals in the direction of the receiving antenna. RCS is an area which defines the amount of power that, when isotropically scattered, generates at the receiver a density which is equivalent to the scattered by the actual target. RCS is the essential parameter in the detection of tanks, airplanes, ships or other military targets. Low-visibility (or hide) airplanes are designed to achieve very low RCS amount, therefore, they cannot be identified by the radar. On the other hand, the large airplanes like the passenger plane may have a big RCS amount because of shiny metal surfaces that reflects approximately all of the incident signal. A rounded shape design which distributes the EM signal in nearly all directions and canonical shapes and cavities (like as engine channel) scatter the incident field in the backside direction. General speaking, the RCS of a target is defined as a function which depends on a polarization of the incident signal, the angle of incidence, the angle of observation, the electrical characteristic of the target, the shape of the target, and the operation frequency. The RCS has a significant role in radar imaging. In this chapter, the fundamentals of radar*

*cross section measurements are presented. After that, the RCS of two quadcopters is estimated by Electromagnetic Simulation Software such as FEKO. For verifying the simulated results of RCS, the real measurement results which are computed by Inverse synthetic radar (ISAR) are illustrated.*

### 3.1 Definition Of Radar Cross Section

Electromagnetic waves in each polarization, are usually scattered in all directions when hitting on a target. These scattered signal are divided into two components. The first part is constructed of signals which polarization is similar to the receiving antenna. The other part of the scattered signals has a different polarization, which does not respond to the receiving antenna. These two polarization are orthogonal, which point to the Principle Polarization (PP) and Orthogonal Polarization (OP), respectively. The back scattered signal whose polarization is similar to the receiving antenna is used to measure the RCS of a target. When the target is illuminated by RF signal, the RCS can be defined as the effective back scattering area of a target as shown in Figure 3.1. In the other words, RCS which is expressed by the unitary term,  $\sigma$ , can be considered as measuring the ability of an object to reflect radar signal in the direction of the radar receiver [3].

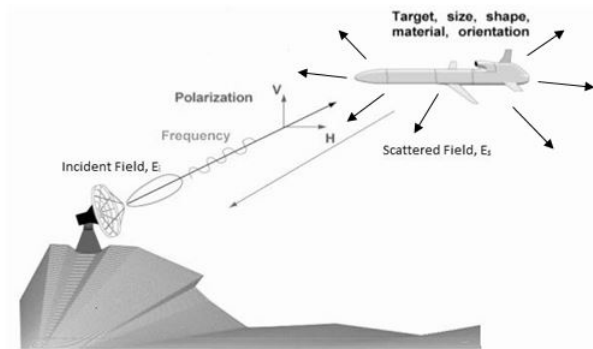


Figure 3.1: The EM signal scatters in all directions when it incidents a target

The formula of RCS can be written with respect to the Figure 3.1. When the target is placed at  $R$  distance from the radar, the transmitting signal from the radar generates a power density of  $P_{Di}$  at the target. The target

has an RCS area of  $\sigma$ , Hence, the amount of reflected power from the target is equivalent to:

$$P_r = \sigma.P_{Di} \tag{3.1}$$

Where  $\sigma$  indicates the target cross section, therefore, the power density of the reflected signal,  $P_{Dr}$ , at the receiving antenna is defined as follows:

$$P_{Dr} = \frac{P_r}{4\pi R^2} \tag{3.2}$$

Eq.3.1 and Eq.3.2 yield:

$$\sigma = 4\pi R^2 \left( \frac{P_{Dr}}{P_{Di}} \right) \tag{3.3}$$

By ensuring that the radar receiving antenna is in the far field, the formal equation of RCS can be modified as the following:

$$\sigma = 4\pi R^2 \lim_{R \rightarrow \infty} \left( \frac{P_{Dr}}{P_{Di}} \right) \tag{3.4}$$

The RCS is measured by Eq.3.4 is used for monostatic RCS. The backscattered RCS is computed from all signal scattered in the direction of the radar which it has the same polarization likes the receiving antenna. It is a part of all scattered target RCS,  $\sigma_t$ , where  $\sigma_t > \sigma$ .

For a spherical coordinate system,  $(\rho, \theta, \phi)$ , in the range  $\rho$ , the target scattered cross section depends on  $(\theta, \phi)$ . The angles  $(\theta_i, \phi_i)$  are shown the direction of propagation of an incident signal and the angles  $(\theta_s, \phi_s)$  are shown the direction of propagation of the scattered signal. Therefore in the spherical case when  $\theta_i = \theta_s$  and  $\phi_i = \phi_s$ , the RCS indicates monostatic RCS, while, the bistatic RCS is measured when  $\theta_i \neq \theta_s$  and  $\phi_i \neq \phi_s$ .

All amount target scattered RCS is calculated as follows:

$$\sigma_t = \frac{1}{4\pi} \int_{\phi_s=0}^{2\pi} \int_{\theta_s=0}^{\pi} \sigma(\theta_s, \phi_s) \sin \theta_s d\theta d\phi_s \tag{3.5}$$

Since the value of the reflected signal from a target is related to the ratio of the size of the target to the wavelength,  $\lambda$ , of the incident signal, hence the

radar cannot detect targets much smaller than its operational wavelength. The measurement of RCS in the frequency zone, in which the target size and wavelength are comparable, are mentioned as the Rayleigh zone. Instead, the frequency region where the target size is much bigger than the wavelength of radar is called the optical area. In fact, most of the radar applications are inside the optical zone.

### 3.2 RCS Dependence on Sight Angle and Frequency

Radar cross section changes as a function of radar frequency and viewing angle. It is defined by assuming isotropic point scatterers which are transmitting signal in all directions. In order to demonstrate how RCS depends on viewing angle, there are two aligned isotropic scatterers, which are set along the radar line of sight. It means they are at zero viewing angle at  $R$  distance in the far field. The distance between the two scatterers equals,  $d$ , and the radar viewing angle is changed from zero to 180 degrees. Suppose the scatterer-1 is a phase reference when the viewing angle is varied, the RCS is modified by the phase, which corresponds to the electrical spacing between the two scatterers. The electrical spacing is measured as follows [3]:

$$D_e = \frac{2 \times d \times \cos \alpha}{\lambda} \quad (3.6)$$

Where  $D_e$  electrical spacing,  $\alpha$ , is the angle between the radar line of sight and the distance between the two separate scatterers and  $\lambda$  is the radar operating wavelength. RCS is dependent on the radar viewing angle as shown in Figure 3.2. The constructive and destructive interference between the two separate scatterers is critical when a radar is measured RCS of complex targets. In fact, it is important due to the two reasons. First, the viewing angle can be continuously changing. Second, the RCS of complex targets can be distinguished from the participation of many individual scattering points distributed on the target surface. These scattering points are mostly named scattering centers. Some approximate prediction methods of the RCS generate a set of scattering centers that describe the back-scattering characteristics of these complex targets.

In the next step, it is demonstrated RCS dependency on frequency. With regard to Figure 3.3, two far field unity isotropic scatterers are aligned with

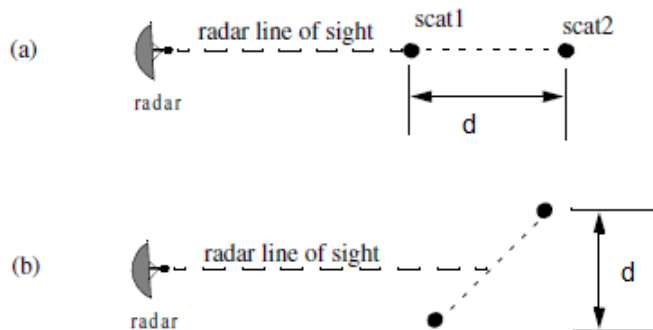


Figure 3.2: RCS dependency on aspect angle. (a) Zero viewing angle, zero electrical spacing.(b) 45 viewing angle,  $1.414\lambda$  electrical spacing

radar line of sight. RCS dependence on frequency is explained by two graphs that are calculated at radar frequencies 8 to 12.5 GHz. Figure 3.4 shows two RCS dependency to the frequency which are calculated for scatterer spacing of 0.1 and 0.7 meters. With respect to these figures, RCS fluctuation as a function of frequency is obvious. Changing the small frequency may result in a sharp fluctuation in RCS when the scatterer distance is large. On the other hand, there are more frequency changes to generate significant RCS fluctuations, when scattering centers are relatively nearby.

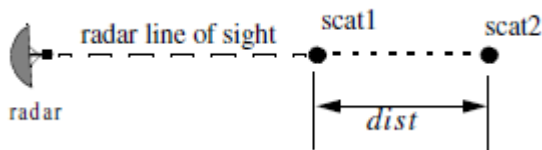


Figure 3.3: RCS dependency on frequency in two different distance ;  $dist = 0.1, \text{ or } 0.7 \text{ m}$

### 3.3 Target Scattering Matrix

Target back scattered RCS is usually defined by a matrix, which is called the scattering matrix. It shows with  $[s]$  symbol. When an arbitrarily linearly polarized signal is hit to a target, the back scattered field is as follows [3]:

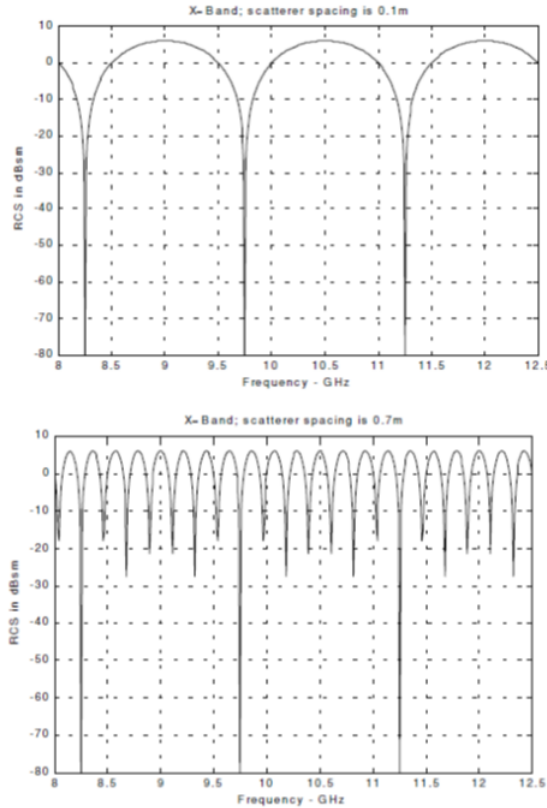


Figure 3.4: Illustration of RCS dependency on frequency at dist. 0.1 m and 0.7 m

$$\begin{bmatrix} E_1^s \\ E_2^s \end{bmatrix} = [S] \begin{bmatrix} E_1^i \\ E_2^i \end{bmatrix} = \begin{bmatrix} S_{11} & S_{12} \\ S_{21} & S_{22} \end{bmatrix} \begin{bmatrix} E_1^i \\ E_2^i \end{bmatrix} \quad (3.7)$$

The superscripts  $s$  and  $i$  show incident and scattered fields. Generally, the values of  $S_{ij}$  are complex numbers and the indexes 1 and 2 show each combination of orthogonal polarizations. Consider that  $1 = H, R$  and  $2 = V, L$ . Therefore in Eq 3.3, the backscattered RCS is depended to the scattering matrix components, as follows:

$$\begin{bmatrix} \sigma_{11} & \sigma_{12} \\ \sigma_{21} & \sigma_{22} \end{bmatrix} = 4\pi R^2 \begin{bmatrix} |S_{11}|^2 & |S_{12}|^2 \\ |S_{21}|^2 & |S_{22}|^2 \end{bmatrix} \quad (3.8)$$

It means that when the scattering matrix is determined, the target back scattered RCS can be estimated for any composition of transmitting and receiving polarizations. Here, Eq.3.8 is rewriting in terms of the different possible orthogonal polarizations.

$$\begin{bmatrix} E_H^s \\ E_V^s \end{bmatrix} = \begin{bmatrix} S_{HH} & S_{HV} \\ S_{VH} & S_{VV} \end{bmatrix} \begin{bmatrix} E_H^i \\ E_V^i \end{bmatrix} \quad (3.9)$$

$$\begin{bmatrix} E_R^s \\ E_L^s \end{bmatrix} = \begin{bmatrix} S_{RR} & S_{RL} \\ S_{LR} & S_{LL} \end{bmatrix} \begin{bmatrix} E_R^i \\ E_L^i \end{bmatrix} \quad (3.10)$$

where  $E_V$  and  $E_H$  are vertical and horizontal polarization.  $E_R$  and  $E_L$  are right and left polarization. By using the matrix transformation  $[T]$  can be written:

$$\begin{bmatrix} E_R \\ E_L \end{bmatrix} = [T] \begin{bmatrix} E_H \\ E_V \end{bmatrix} \quad (3.11)$$

Therefore, the circular scattering elements can be calculated from the linear scattering elements:

$$\begin{bmatrix} S_{RR} & S_{RL} \\ S_{LR} & S_{LL} \end{bmatrix} = [T] \begin{bmatrix} S_{HH} & S_{HV} \\ S_{VH} & S_{VV} \end{bmatrix} \begin{bmatrix} 1 & 0 \\ 0 & -1 \end{bmatrix} [T]^{-1} \quad (3.12)$$

Therefore, each component is equal:

$$\begin{aligned} S_{RR} &= \frac{-S_{VV} + S_{HH} - j(S_{HV} + S_{VH})}{2} \\ S_{RL} &= \frac{S_{VV} + S_{HH} + j(S_{HV} - S_{VH})}{2} \\ S_{LR} &= \frac{S_{VV} + S_{HH} - j(S_{HV} - S_{VH})}{2} \\ S_{LL} &= \frac{-S_{VV} + S_{HH} + j(S_{HV} + S_{VH})}{2} \end{aligned} \quad (3.13)$$

And in a similar way, for linear scattering elements can write:

$$\begin{bmatrix} S_{HH} & S_{HV} \\ S_{VH} & S_{VV} \end{bmatrix} = [T]^{-1} \begin{bmatrix} S_{RR} & S_{RL} \\ S_{LR} & S_{LL} \end{bmatrix} \begin{bmatrix} 1 & 0 \\ 0 & -1 \end{bmatrix} [T] \quad (3.14)$$

Finally, each component can be written as follows:

$$\begin{aligned} S_{HH} &= \frac{-S_{RR} + S_{RL} + S_{LR} - S_{LL}}{2} \\ S_{VH} &= \frac{j(S_{RR} - S_{LR} + S_{RL} - S_{LL})}{2} \\ S_{HV} &= \frac{-j(S_{RR} + S_{LR} - S_{RL} - S_{LL})}{2} \\ S_{VV} &= \frac{S_{RR} + S_{LL} + jS_{RL} + S_{LR}}{2} \end{aligned} \quad (3.15)$$

### 3.4 RCS of Simple Form Objects

Due to the great interest in the formation of scattered fields and RCS from simple objects such as a sphere, cylinder, ellipsoid, or plate, RCS analysis of such objects is archived in [1, 4–7], but only some of them, which are in Radar imaging is important are listed in Figure 3.5. Radar Cross Section of these simple objects is calculated with respect to the parameters such as size, frequency, and aspect angle. Investigating the RCS of the simple objects is essential for extending to complex shapes. Therefore, in some popular complex targets like planes, ships, and tanks, their physical forms include canonical structures such as corner reflectors, cylinder structures, and flat and curved surfaces are considered [8, 9].

### 3.5 RCS of Complex form Objects

In the complex target case, RCS is usually calculated by coherently combining the cross sections of the simple shapes which makes target. It means that a complex target RCS can be measured as a group of the discrete scattering centers. The scattering centers can be modeled as isotropic point scatterers (N-point model) or as simple shape scatterers (N-shape model). As it



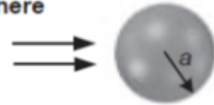
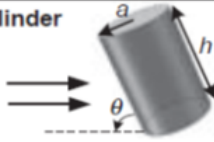
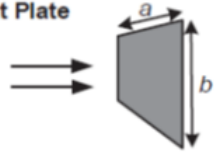
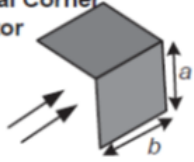
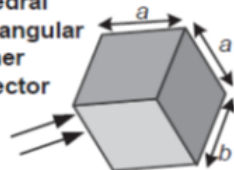
Object	RCS
<b>Sphere</b> 	$\sigma = \pi a^2$ $(a \gg \lambda)$
<b>Cylinder</b> 	$\sigma = \frac{a\lambda}{2\pi} \frac{\cos \theta \sin^2(kh \sin \theta)}{\sin^2 \theta}$ $\sigma = \frac{2\pi a h^2}{\lambda} \quad (\theta = 90^\circ)$
<b>Flat Plate</b> 	$\sigma_{max} = 4\pi \left(\frac{ab}{\lambda}\right)^2$ $(ab \gg \lambda)$
<b>Dihedral Corner Reflector</b> 	$\sigma_{max} = 8\pi \left(\frac{ab}{\lambda}\right)^2$ $(ab \gg \lambda)$
<b>Trihedral Rectangular Corner Reflector</b> 	$\sigma_{max} = 12\pi \left(\frac{ab}{\lambda}\right)^2$ $(ab \gg \lambda)$

Figure 3.5: RCS values for perfectly conducting simple objects (all objects are taken as perfect electrical conductors)

mentioned in section 3.2, the relative distance and viewing angles of the individual scattering center sharply effect on the overall RCS. Therefore, the complex target can be modeled by some equivalent scattering centers are often named Swerling 1 or 2 targets, while the targets have one dominant scattering center and some smaller scattering center are investigated as Swerling 3 or 4 targets. In narrow band (NB) radar applications, by participating all scattering centers is created only a single value for the RCS of the target at any viewing angle. However, in wide band (WB) applications, a target

may spread on many domains. For each range, the average RCS extracted by the radar represents the participation of all the scattering centers which happened within the domain [3].

### 3.6 RCS Fluctuation and Statistical Models

In most radar applications, there is a relative movement between the radar and the observed target. Thus, the RCS measured by the radar changes over a period of time as a function of the frequency and viewing angle of the target. This observed RCS is known as the radar dynamic cross-section. Dynamic RCS may have fluctuated in amplitude or in phase, where phase fluctuation is called glint and amplitude fluctuation is called scintillation. The far-field back scattered wave fronts from a target can be non-planar, because of Glint. Almost in the most radar application, glint generates linear errors in the measurement of radar, which is not really the main concern. However, in cases which require high accuracy, glint may be detrimental. To express a few examples of precision instrumentation tracking radar systems, automated aircraft landing systems and missile seekers can be named. The reflected signal fluctuation is based on the complex diagram of the relative radar cross section (RCS). In a forward motion, the RCS chart of the aircraft is placed in the reference to the radar set. The reason for time variations during the target period is the change in amplitude and phase, which outcome a strong fluctuation of the reception field strength in the radar antenna. Therefore, the Swerling models were introduced to be used to describe the statistical properties of the radar cross section of objects with a complexly formed surface. Given the Swerling models, the RCS acts as a reflection object based on the probability density of a certain amount of freedom. These models are very important theoretically radar technology. There are five different Swerling models, which named with Roman numerals from I to V. The selection of a specific model depends on the nature of the target under investigation [3]. At the first, the chi-squared distribution is presented. The chi-square distribution is a specific case of the gamma distribution which is one of the most widely used possibility distributions in inferential statistics in hypothesis testing or in the construction of confidence intervals. The Chi-square of degree  $2m$  distribution exerts to a wide range of targets; so its pdf is the following:

$$f(\sigma) = \frac{m}{\Gamma(m)\sigma_{av}} \left(\frac{m\sigma}{\sigma_{av}}\right)^{m-1} e^{-\frac{m\sigma}{\sigma_{av}}} \quad \sigma \geq 0 \quad (3.16)$$

Where  $\Gamma(m)$  is the gamma function with argument  $m$ , and  $\sigma_{av}$  shows the average value. As the degree becomes larger, the distribution matches to constrained RCS values (narrow range of values). The limit of  $m \rightarrow \infty$  relates to a fixed RCS target (stable-target case).

### 3.6.1 Swerling I Target

This case shows a target which magnitude of the back scattered signal is relatively constant throughout the dwell time. In Swerling I, the RCS samples which are measured by radar are correlated from pulse to pulse, but independent of scan to scan (slow fluctuation). The density of probability of the RCS is given by the Rayleigh-Function, so the pdf is:

$$f(\sigma) = \frac{1}{\sigma_{av}} \exp\left(-\frac{\sigma}{\sigma_{av}}\right) \quad \sigma \geq 0 \quad (3.17)$$

Where  $\sigma_{av}$  indicates the average RCS overall target fluctuation.

### 3.6.2 Swerling II Target

The Swerling II target is similar to Swerling I, using the same equation, but Swerling II target fluctuation is more rapid than Swerling I, and the measurements are the pulse to pulse uncorrelated. The Swerling I and II apply to a target that is made up of many independent scatterers of nearly equal areas, such as aircraft. However, in the Swerling case II, there is no rotational surveillance antenna but a focused on a target tracking radar.

### 3.6.3 Swerling III Target

The Swerling III target is depicted like Swerling I, but with four degrees of freedom ( $m = 2$ ). The scan-to-scan fluctuation follows a density of probability is shown by pdf as follows:

$$f(\sigma) = \frac{4\sigma}{\sigma_{av}^2} \exp\left(-\frac{2\sigma}{\sigma_{av}}\right) \quad \sigma \geq 0 \quad (3.18)$$

### 3.6.4 Swerling IV Target

The Swerling case IV is similar to Swerling III, but the RCS varies from pulse to pulse rather than from scan to scan and follows as the same pdf in Swerling III. In the situation of III and IV approximates a large scattering surface of an object with several other small scattering surfaces.

### 3.6.5 Swerling V Target

The Swerling case V is a reference value with a fixed radar cross section (also recognize as Swerling 0). It describes an ideal target without any fluctuation. Figure 3.6 shows the radar returns from targets with different Swerling fluctuations. The Swerling V related to a steady RCS target case.

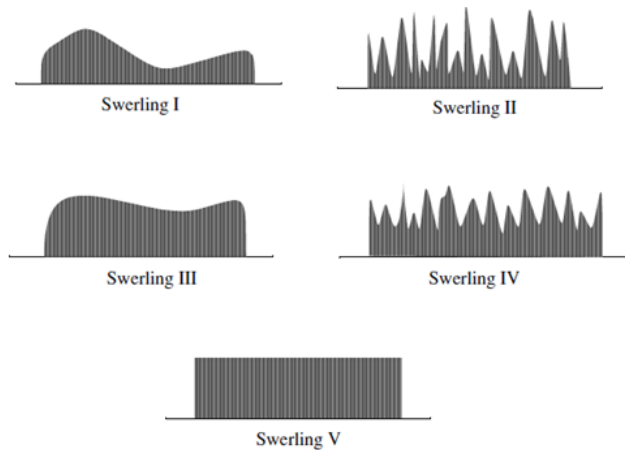


Figure 3.6: Different Swerling fluctuations of radar returns from targets

## 3.7 Relationship Between RCS and Inverse Synthetic Aperture Radar

By using the Inverse Synthetic Aperture Radar (ISAR), it is possible to achieve a high spatial resolution of a target. ISAR basic principle is that the target is rotated to achieve a variation in viewing angle to the stable radar. Therefore, the ISAR image is a display of the spatial distribution

of the reflectivity of a target. The reflectivity of a target is plotted onto a range versus cross range which has shown the radar image of the target. The image contains very small picture elements (pixels) that represent the distributed radar cross-section of the target. The imaging of radar cross section can be considered as a map of scattered signal, as RCS is directly related to the amount of radiation scattered from the lighted target. Since the RCS measurements provide global information about a target, but they do not provide information about the features that are primarily responsible for radar response such as the observation angle, the angle of incidence, the geometry of target and the operation frequency, therefore, the RCS of the scatterer is obtained from Inverse Synthetic Aperture Radar (ISAR) images. In general terms, RCS is shown by different shadow colors and usually, the bright colors represented largely radar cross section. It means that an object is more easily detected with a big RCS. But one of the important matter in the ISAR images is scattered energy from the surrounding background which is named clutter. Clutter echoes are visible in radar images and it causes to complicate their interpretation. Another cause of incorrect interpretation of images ISAR is the unavoidable side-lobe effect of the Fourier transform process. The side lobes of the transform tend to eliminate the RCS of bright scatterers. Therefore, before producing the ISAR image the effect of side lobes can be removed by filtering the processed information [10].

### 3.8 RCS Measurement

In order to investigate RCS, two different types of drones, a toy drone (SYMA) and a professional UAV (AirVison), were taken into account. RCS of both of drones was computed by radar experiments, the RCS results are compared with simulated results of drones which were modeled by FEKO (Electromagnetic Simulation Software). Figure 3.7 and Figure 3.8 show a toy and professional UAVs respectively.

For radar cross section (RCS) measurement the quadcopter has been situated on the circular platform as demonstrated in Figure 3.9. The spacing between the antennas and rotation center of the platform was  $156\text{cm}$ . A complete measurement with antennas in vertical polarization has been done for angular step equal  $1\text{deg}$ . The bandwidth used was 4 GHz that used a Kaiser window with  $\beta = 5$ , it gives  $FWHM = 0.54\text{m}$ .



Figure 3.7: SYMA quadcopter

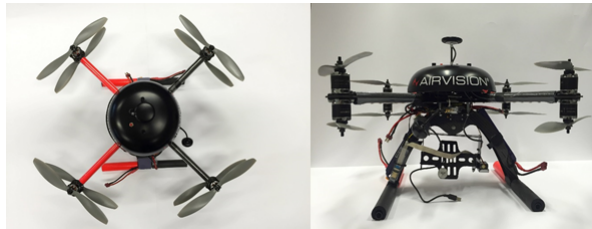


Figure 3.8: AirVision quadcopter

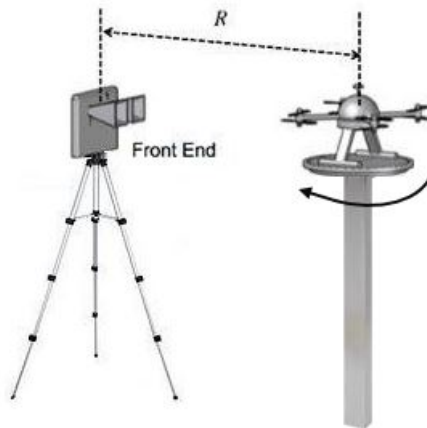


Figure 3.9: Sketch of the measurement equipment

The measurement angular pattern of RCS of a toy drone is shown in Figure 3.10. Regarding the Figure 3.10, the largest values are in correspondence of the four motors. The measured main value of the RCS has been  $0.0312 \text{ m}^2$ .

The measured RCS has been compared with swirling distribution which

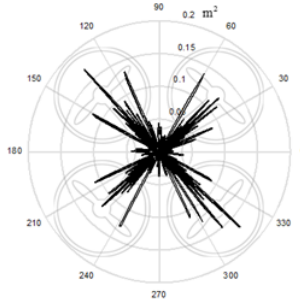


Figure 3.10: RCS angular pattern of SYMA quadcopter

is computed as follows:

$$p(\sigma) = \frac{1}{\bar{\sigma}} e^{-\frac{\sigma}{\bar{\sigma}}} \tag{3.19}$$

Where  $\sigma$  is the mean value of RCS. Figure 3.11 illustrated the statistical distribution of RCS of a toy drone during the 3D scan. Hence, there are a lot of points compared to the theoretical result. It is worth to note that there is a good agreement between swirling and statistical distribution. The RCS of SYMA quadcopter has been measured also in horizontal polarization, by rotating the antennas. The acquired main value has been  $0.0229 \text{ m}^2$ . There are no considerable differences respecting to the RCS pattern in vertical polarization, also the agreement with Swerling distribution is equally good.

The same measurements have been carried out with the AirVision quadcopter. The measured angular pattern of RCS in vertical polarization is shown in Figure 3.12. The largest RCS values related to in front and back of drone in this case. The main value is  $0.271 \text{ m}^2$ . It should also be noted that for AirVision there is a good agreement between the simulated and measured result.

Figure 3.13 displays the good agreement between RCS distribution of the professional UAV, which is computed in 3D scan, and Swerling model. The RCS of AirVision quadcopter has been measured also in horizontal polarization by rotating the antennas. The obtained value has been  $0.2759 \text{ m}^2$ .

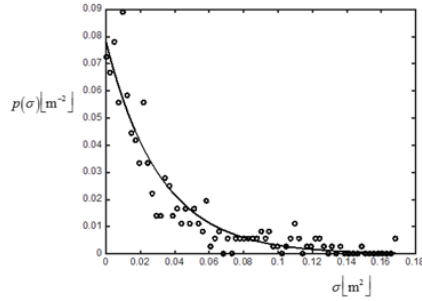


Figure 3.11: RCS distribution of SYMA quadcopter. The full line is the Swerling distribution

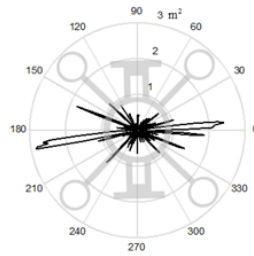


Figure 3.12: RCS distribution of AirVision quadcopter

There are no essential differences with respect to the RCS pattern in vertical polarization, also the agreement with Swerling distribution is equally good.

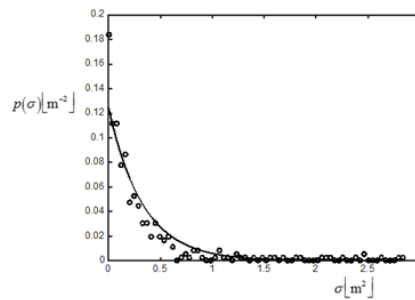


Figure 3.13: RCS distribution of AirVision quadcopter. The full line is the Swerling distribution



Table 3.1 presents the obtained results.

Table 3.1: Measured RCS

	Vertical pole	Horizontal pole
SYMA X5SC-1	$0.0312 \text{ m}^2$	$0.0229 \text{ m}^2$
AIRVISION NT4CONTRAS	$0.271 \text{ m}^2$	$0.276 \text{ m}^2$

In the second stage, both drones were modeled by FEKO (Electromagnetic Simulation Software). Figure 3.14 and Figure 3.15 show the simulated a toy and professional UAVs respectively.

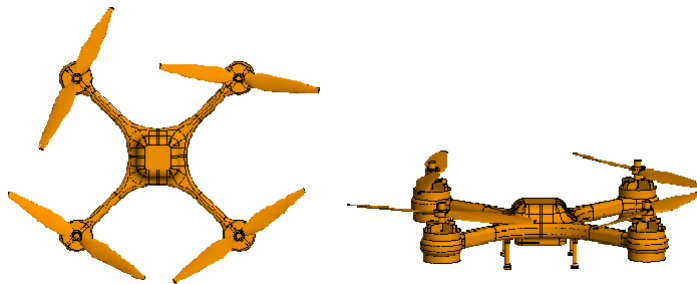


Figure 3.14: Simulated Small Quadcopter

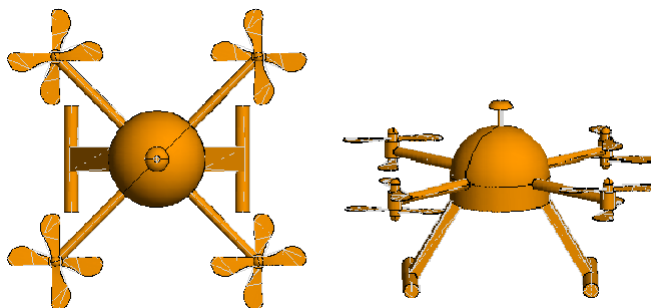


Figure 3.15: Simulated AirVison Quadcopter

Simulation has done at frequency 10 GHz for  $\phi = 0-360 \text{ deg}$  and  $\Theta = 90 \text{ deg}$ . The angular step was  $1 \text{ deg}$ . The simulated angular pattern of RCS of a toy drone is illustrated in Figure 3.16. The largest values are in correspondence of four motors.

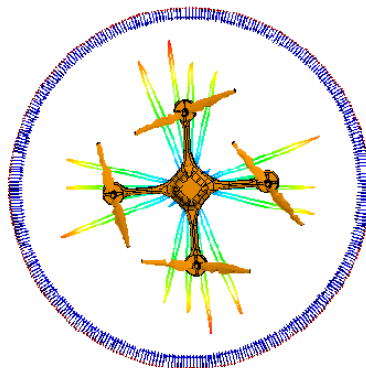
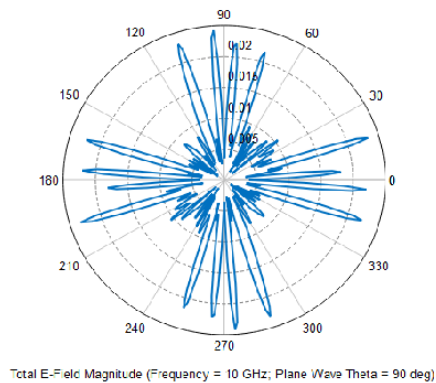


Figure 3.16: RCS angular pattern of small quadcopter

The simulated angular pattern of RCS of the professional drone is illustrated in Figure 3.17. The largest values are in correspondence of front and back of quadcopter.

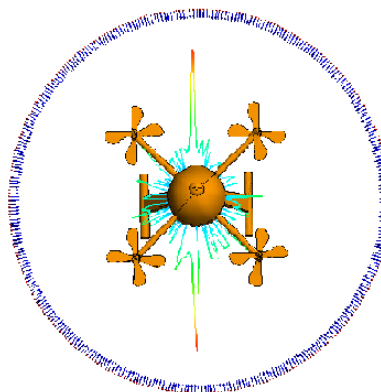
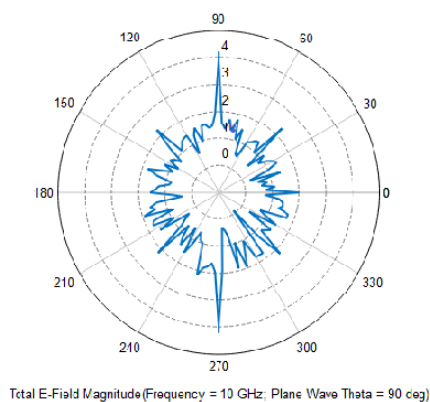


Figure 3.17: . RCS angular pattern of AirVison quadcopter

By comparing the radar measurements and simulated results, it is obvious a good agreement between simulated results and measurement results.

### 3.9 Conclusion

The RCS measurement of a toy drone and a professional drone has been performed by using radar equipment and simulation. According to the results, a professional quadcopter has an RCS at least ten times larger than a toy drone. A considerable result of this study is that Swerling distribution has good agreement with the RCS statistical distribution of the drones we

tested, as well as the simulated results are compatible with experimental results. Another significant result is that the mean value of RCS in vertical and horizontal polarization is approximately equal.

# Chapter 4

## 2D And 3D Inverse Synthetic Aperture Radar Imaging of a Small Quadcopter and Its Basic Concepts

*Inverse synthetic aperture radar (ISAR) is a powerful and well-established technique for obtaining both 2D and 3D images of radar targets. ISAR processing is commonly used for the identification and classification of targets. The range resolution is defined as the parallel axis in the direction of propagation from radar into the target which depends on the effective bandwidth  $B_w$  of the transmitted signals. On the other hand, cross-range resolution is defined along the orthogonal axis to the range direction which is related to the angle  $\Delta\Theta$  through which the target rotates relative to the radar-line-of sight. In this chapter, 2D and 3D ISAR image processing have been carried out for imaging small UAVs. The two-dimensional (2D) ISAR image is made by collecting scattered fields from different angles, while a 3D image can be measured by integrating backscatter data in two spatial coordinates of the 2D aperture (cross-range in azimuth and elevation).*

#### 4.1 Synthetic Aperture Radar (SAR) and Inverse Synthetic Aperture Radar (ISAR) Concepts

Synthetic Aperture Radar (SAR) processing coherently combines signals acquired from sequences of small apertures get at diverse viewing angles to synthesize a large aperture. Generally speaking, the transmitting antenna is mounted on a moving platform, often, an aircraft or satellite, or other moving platforms, like helicopters and ground-based rails. The SAR denotes the case where the radar platform is moving, whereas the target stays stationary [8, 11, 12]. The modes of SAR operation can be divided into the strip-map mode and the spotlight mode. As demonstrated in Figure 4.1(a), when the antenna beam travels in a fixed direction relative to the moving direction of a platform, this mode is named strip -map SAR. The strip-map mode can produce a long strip of the flight path. In the spotlight mode, the radar tracks and focuses its illumination on a particular area of attention, as illustrated in Figure 4.1(b). This mode generates good resolution images of tiny scenes [8, 13, 14].

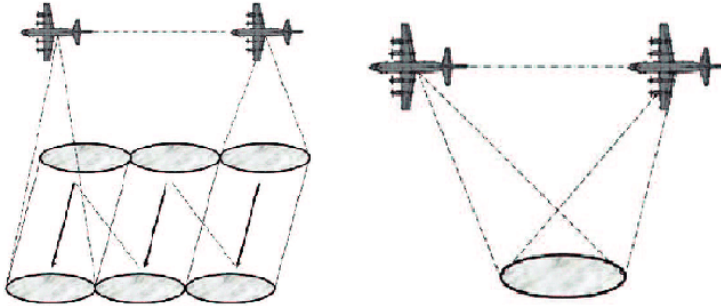


Figure 4.1: Common modes of SAR (a) Strip-map SAR and (b) Spotlight SAR

For reconstructing the radar image of a target from echo signal, it is needed that each returned signal must be procured with a distinct view of the target. Therefore, a relative rotation between the radar and the target is necessary for generating different sight-view of the target, so that each signal transmitted by radar will capture a different view of the target. Hence the relative movement between the radar platform and the target must be noticed. It means that the motion is not necessarily produced by a moving platform; in fact, a development in cross-range resolution can also be achieved by moving

target regard to the static radar [15, 16]. The position of the reference coordinate system is important in the concept of relative movement, actually, it can be argued that whether a configuration named a fixed target and a moving platform or fixed platform and a moving target. The usual procedure accomplishes by placing the reference system on the target and the latter by placing the reference system on the radar. According to the mentioned expression, the differences between SAR and ISAR would depend just on where the reference system is set. Such a concept express that, where the configuration of SAR spotlight is configured as ISAR, by moving the reference system from target to radar. Accordingly, the term ISAR is used for scenarios when the radar is stationary and the target is in motion, such as with airplanes, drones, as shown in Figure 4.2 [13]. The required range resolution of ISAR is obtained by using the finite frequency bandwidth of the transmitted signal, such as SAR.

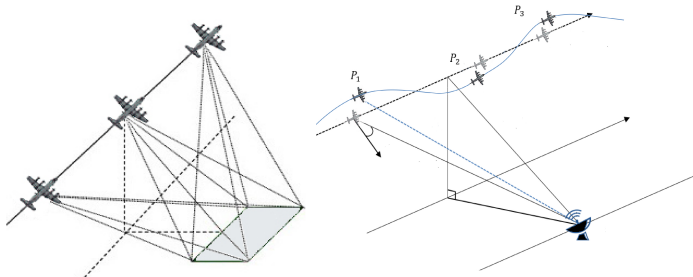


Figure 4.2: (a) Spotlight SAR and (b) ISAR configuration

In contrast, the same concept may be discussed by starting with a controlled ISAR configuration, such as a turntable experiment. In the rotary configuration, the radar antenna is stood on the ground and the target is placed on a rotary table, as depicted in Figure 4.3(a) based on collected data from echo, actually, can also be thought the ISAR is similar to spotlight SAR geometry with circular flight paths as illustrated in Figure 4.3(b). In the other words, as depicted in Figure 4.4, where the radar moving along a circular path gathers the back scattered field data from the stationary target for an angular width of  $\Theta$  for the spotlight SAR geometry. On the other hand, the standing radar gathers the back scattered field data from a rotating target. The same reflectivity data can be obtained if the target rotates in the same angular width of  $\Theta$  provided that of the radar.

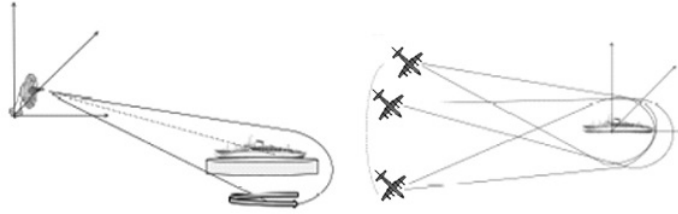


Figure 4.3: (a) ISAR and (b) circular SAR configuration

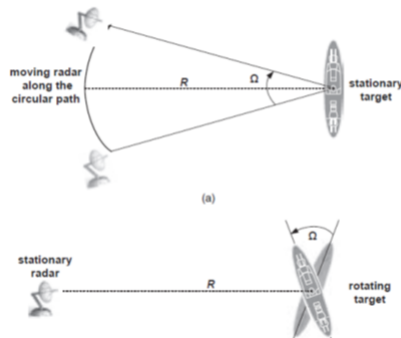


Figure 4.4: SAR to ISAR transition: (a) spotlight SAR with circular flight path, (b) ISAR

For more details, where the reference system is placed determines the type of configuration (i.e. SAR or ISAR configuration), but in practice, there is an important detail which does not depend on positioning the reference system but it depends on the target. For the better explanation of this concept, one may set the reference system on the target and if it moves with respect to the radar with unknown motion parameters. This is a non-cooperative target. Hence, the synthetic aperture formed during the coherent processing interval differs from that constructed by an expected controlled motion of the platform, like a rotary experiment. Figure 4.4. shown a non-cooperative motion of the movement of target, where the unknown and non-cooperative motion of the target generates an unpredictable synthetic aperture. At this time, it is very important to say this fact whether the target is cooperative because it presents a number of issues, which ISAR is important to determine the relative motion between the radar and the target, and thus, to



form radar images of non-cooperative targets. In fact, the synthetic aperture formed by an arbitrary target's movement with respect to the radar is also unknown. It means that the positions of the synthesized aperture components are not known in advance. Since SAR image processing is based on such a knowledge, it should say that any SAR image formation algorithm may not be successfully applied to form a focused image of a non-cooperative target [13,17].

#### **4.2 The Relation of Electromagnetic (EM) Scattering Field to the Image Function in ISAR**

Scattering is a physical phenomenon that occurs when an EM wave causes a non-conformance an object. The path deviation of the wave trajectory is generally known as scattering. The classification of scattering phenomena can be based on the size of the scattered object (or the scatterer) according to the wavelength of the EM wave. Radar signals are scattered in different ways according to the EM wavelength and the form of the object (scatterer). If the wavelength of the EM wave is extremely tiny than the size of the reflected wave, the EM wave reflection backs in a similar way to the degree the light reflects from a large surface. This sort of scattering is named scattering in the optical region [18]. If EM wavelengths are comparable to the size of the scatterer, some resonances may happen, and the scattering severity can fluctuate considerably for variant frequencies. This type of scattering is named resonant region where the direction of scattering is affected by the incident wave direction [19]. The wave is dispersed around the scatterer if the wavelength of the EM wave is longer then the size of the scatterer. This reflection is called Rayleigh scattering [20]. It is worth noting that, there is another category for type of scattering which is based on the wave's trajectory from different structures, such as planar surfaces, curved surfaces, corners, edges, or tips.

The main matter for radar theory and radar imaging is EM scattering. Actually, the imaging of radar is the reflected signal from target or scene. In the following, the scattered electric field at the far - field region along the viewpoint of  $r$  is determined by:

$$E^p(r) = -\frac{j k_0 E_0}{4\pi r} e^{-j k_0 r} \iint_{S_{lit}} 2\hat{n}(\hat{r}) \times (\hat{k}^i \times \hat{u}) e^{-j(k^p - k^i)\hat{r}} d^2\hat{r} \quad (4.1)$$

Where  $k^p = k_0 \hat{r}$  is the wave number vector in the scattering direction. This is the scattered electric field in the far field which is constituted a basis for the derivation of ISAR imaging of objects. Hereon,  $k^i$  and  $k^p$  are the incident and scattered wave number vectors,  $\hat{n}(\vec{r})$  is the outside surface unitary common vector,  $\hat{k}^i$  is the unit vector in transmitted wave,  $E_0$  and  $\hat{u}$  are the magnitude and the polarization unit vector of the transmitted wave, and  $S_{lit}$  demonstrate the portion of the surface of an object. It is noteworthy, the receiving antenna has a special direction which it can gather the reflected signal in the  $\hat{v}$  direction, which is the perpendicular direction to the direction of propagation of the waves. Therefore the Equation can rewrite, by following:

$$\hat{v} \cdot \vec{E}^p(\vec{r}) = -\frac{j k_0 E_0}{4\pi r} e^{-j k_0 r} \iiint_{-\infty}^{\infty} O(\vec{r}') e^{j(\vec{E}^p - \vec{E}^i) \cdot \vec{r}'} d^3 \vec{r}' \quad (4.2)$$

Where  $O(\vec{r}')$  can be told as the scalar object shape function (OSF) which is the argument of the impulse function:

$$P(\vec{r}') = \begin{cases} \neq 0, & \vec{r}' \in S_{lit} \\ 0, & \vec{r}' \in S_{shadow} \end{cases} \quad (4.3)$$

The surface integral in Eq.4.1 is substituted by a volume integral over the whole three - dimensional (3D) space as given in Eq.4.1. By using the 3D Fourier transform (FT) of the OSF in the  $\hat{v}$  direction, the scattered electric field can be written as:

$$\hat{v} = \vec{E}^p(\vec{r}) = \left(-\frac{j k_0 E_0}{4\pi r}\right) e^{-j k_0 r} \tilde{O}(\vec{E}^p - \vec{E}^i) \quad (4.4)$$

Therefore, the ISAR image can display the OSF onto the 2D or 3D dimensions. It is also worthwhile to mention that OSF varies with respect to the viewing angle and the frequency of operation. ISAR image is directly related to the 2D or 3D inverse Fourier transforms(IFT) of the scattered electric field, alike OSF [21, 22].

### 4.3 Point Spread Function in ISAR Imaging

In general, the imaging of an object of interest is the exploitation of the impulse response of back scattered signal from an electromagnetic wave (EM) which is propagated to the object. The most significant factor of an imaging system is its spatial resolution, which is defined as the Minimum distance at which two similar objects are detected by the system as two different images of objects. The spatial resolution of a radar imaging system is specified by the length of the transmitted pulse and the antenna beam-width. In other words, the pulse length limits the range resolution in the direction of radar to the target and the antenna pattern determines the cross-range (or azimuth) resolution in the direction perpendicular to the line of sight of radar. Therefore, the radar images are determined by a range and a cross-range resolution. It should be noted that the high-resolution images can be obtained by a transmitted pulse with very short duration and high power pick. Finally, we can say that the reflected signal is processed through the pulse compression technique by convolving the signal with the matched filter to compress the pulse length. The mathematical function of a radar imaging system is expressed as follows:

$$I(x, y) = \iint O(u, v).h(x - u, y - v) du dv \quad (4.5)$$

Where  $O(u, v)$  is the object function,  $I(x, y)$  is the resulting reconstructed image of the object, and  $h(x, y)$  is the radar system impulse response function. If the system impulse response becomes at 2D delta Dirac function,  $h(x, y) = \delta(x, y)$ , then the expected output of radar system,  $I(x, y)$ , is equal to the object reflectivity function, or in the other words, if the reflectivity function becomes 2D delta Dirac function, then the image  $I(x, y)$  becomes the Point Spread Function (PSF) [13].

### 4.4 ISAR Imaging Resolution

ISAR image resolution is the ability to resolve scatterers in the ISAR image. It means the assessment of the quality of imaging. To derive the resolution, let refer to the Range and the cross - range resolutions in ISAR, which determine the quality of the outcome image. The definition of the radar imaging resolution parameters is presented as follows.

#### 4.4.1 Range Resolution

Radar range resolution is an important characteristic of radar which is the capability of a radar system to distinguish between two or more targets in the same direction but at different distances. The important factor in range resolution is the bandwidth of the signal. The theoretical range resolution of a radar system can be expressed as follows [23,24]:

$$\Delta R = \frac{c}{2B_w} \quad (4.6)$$

Where  $B_w$  is the bandwidth of the transmitted signal,  $c$  is the speed of space and the constant “2” indicates the two - way propagation between the radar and the point scatterers. So, the higher frequency bandwidth, the better the resolution would be in the range direction.

#### 4.4.2 Cross-Range Resolution

Generally, cross-range resolution is the direction orthogonal to the flight path of radar. In the other words, radar cross-range resolution is an ability of radar to distinguish the minimum distance between two equal large targets at the same range [24]. A good cross-range resolution in the SAR system is obtained by forming a synthetic aperture antenna by moving the radar antenna along the flight path. The cross-range resolution is computed as following when there is a single antenna.

$$\Delta s = \frac{R\lambda}{2D} \quad (4.7)$$

Where  $\lambda$  is bandwidth and  $D$  is the antenna aperture size. It should be noted that the effective synthetic aperture size is twice more than a real aperture. The Eq.4.7 shows that the higher angle width presented the better resolution in azimuth direction [8].

### 4.5 Two-Dimensional ISAR Image Processing

Here, the basic 2D ISAR imaging theory is presented. The ISAR processing would make it possible to obtain a 2D high-resolution image, which displays the location of a target in a 2D coordinate system. The scattered field should be collected for different frequencies and aspects to be capable of producing

the 2D ISAR image, as demonstrated in Figure 4.5(a). The result of the collected data set is generated in the spatial-frequency domain, which is to say  $k_x$  and  $k_y$ . The 2D process occupies a nonuniform grid in the  $k_x - k_y$  space. If the transmitted signals are combined in the narrow bandwidth of frequencies,  $B_w$ , and within a narrow width of angles,  $\phi$ , as illustrated in Figure 4.5(b) [8].

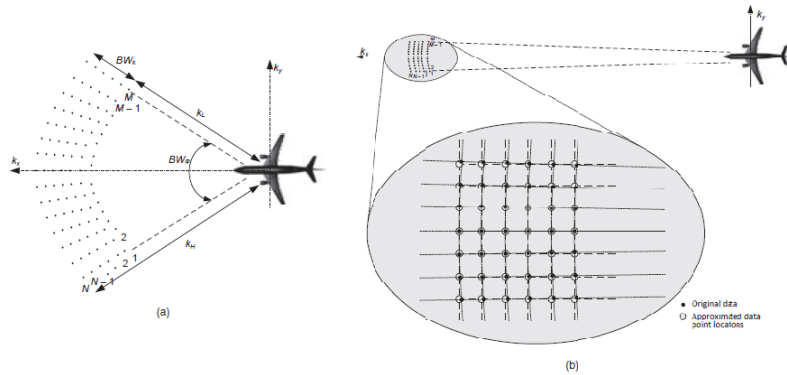


Figure 4.5: (a) ISAR raw data (b) ISAR data collection

It is worth noting that the data grid in  $k_x - k_y$  space approximates to an equally spaced linear grid if the bandwidth  $B_w$  and  $\phi$  both are small. It means that it is possible to use a fast inverse Fourier transform for generating the ISAR images. Let's assume the target is a point scatterer  $p(x_0, y_0)$  as depicted in Figure 4.6, the received signal from the point scatterer at an azimuth angle  $\phi$  can be approximated as:

$$E^p(k, \phi) = A e^{-j2\vec{k}\vec{r}} \quad (4.8)$$

Where  $A$  is the amplitude of the back scattered,  $k$  is the vector wave number in the propagation direction and  $r$  is the vector from center to the scatterer point  $p$ . The center point is the phase center of geometry. Factor 2 indicates the two-way path between the radar and target. The  $k$  vector can be written in  $x$  and  $y$  directions, as the following:

$$\vec{k} = k \cdot \hat{k} = k \cdot (\hat{x} \cos \phi + \hat{y} \sin \phi) \quad (4.9)$$

Where  $\hat{k}$ ,  $\hat{x}$ , and  $\hat{y}$  are the unit vectors in  $k$ ,  $x$ , and  $y$  directions. Therefore, the Eq.4.8 can be written as follows:

$$E^P(k, \phi) = A e^{-j2k \cos \phi x} \cdot e^{-j2k \sin \phi y} \quad (4.10)$$

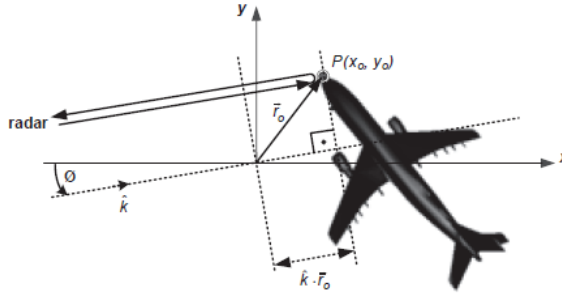


Figure 4.6: Geometry of 2D ISAR Imaging

Eq.4.10 provides two separate phase terms as the function of both the frequency variables,  $k$ , and the angle of view of  $i$  antenna position. Therefore, this equation can be written for each  $f_k$  frequency and for each  $i$  antenna position with complex numbers as below:

$$E(k, i) = I_{k,i} + jQ_{k,i} \quad (4.11)$$

Where  $I$  indicates the in-phase and  $Q$  indicates the quadrature components of the received signal. Then the basic formula for radar image  $I(P_n)$  in a generic point  $p(x_0, y_0)$  is acquired by summing all signal contribution relating to the points, as shown in Figure 4.6 [25, 26]

$$I(P_n) = \frac{1}{(n_f n_p)} \sum_{i=1}^{n_p} \sum_{k=1}^{n_f} E_{ik} e^{\frac{4\pi f_k}{c} R_i} \quad (4.12)$$

Where  $n_f$  is the number of frequencies and  $n_p$  is number of position of the radar antenna and  $c$  is the speed of light. The distance between the image point  $P_n$  and the  $i$  position of antenna is  $R_i$ . Eq.4.12 requires considerable

amount of processing time and its computational is so heavy. Therefore, it can be evaluated faster by applying inverse Fast Fourier transform of the measured data. The ISAR image can be obtained in range and cross-range domains by the convenience of the 2D IFFT. For each antenna position, the first step has been to focus on the matrix  $E$  in range. By applying a suitable window the side-lobes are lowered (in particular a Kaiser window with  $\beta = 5$ , is applied which reduces side-lobes lower than 40 dB). Afterward, the signal is extended by zero-padded of factor,  $F$ , to prevent resolution degradation. It means that each column of echo matrix will have  $F n_f$  elements of which the last  $(F-1)n_f$  zeros). So, the resulting step in the range is  $\Delta R = \frac{n_f-1}{F n_f} \frac{c}{2B_w}$  where  $F n_f$  is the expanded signal length. At the end by regard to Figure 4.7, the focused image in a generic point identified by  $p(x_0, y_0)$  is obtained by:

$$I = \frac{1}{n_p} \sum_i u_i(R_i(x_0, y_0)) \quad (4.13)$$

$$u_i(R_i(x_0, y_0)) = e^{j \frac{4\pi}{c} f_1 R_i(x_0, y_0)} IFFT_{n(R_i(x_0, y_0))}(E_{ki}, F n_f) \times e^{j \frac{4\pi}{c} \frac{B_w}{2} (R_i(x_0, y_0) - (n(R_i(x_0, y_0)) - 1) \Delta R)} \quad (4.14)$$

$$u_i(R_i(x_0, y_0)) = integer\left(\frac{R_i(x_0, y_0)}{\Delta R}\right) \quad (4.15)$$

Where  $f_1$  is the lower frequency and  $B_w$  is the bandwidth [27].

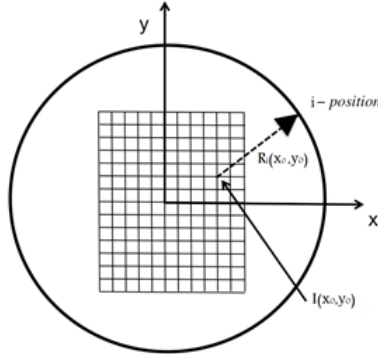


Figure 4.7: Geometry of 2D ISAR focusing algorithm

### 4.6 Three-Dimensional ISAR Image Processing

In 2D ISAR operations, radar usually tracks a target which has a rotary motion to gather different reflected frequency from different view angles. 2D images show in range and cross-range direction of the target. In a similar manner, a 3D image of a target can be captured by carrying out radar measurement for two different orthogonal viewing angles of the target. In fact, a 3D ISAR image shows a 3D profile in range direction and two cross-range domains (Azimuth and Elevation direction).

Therefore, the scattered signal should be collected for various frequencies and different azimuth and elevation direction as depicted in Figure 4.8 [8].

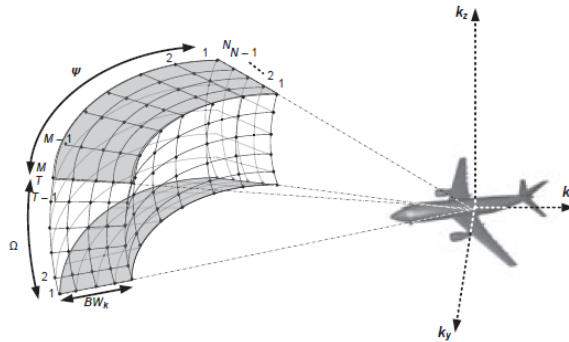


Figure 4.8: Collection of raw ISAR data in 3D

With regard to the Figure 4.8, the collected data occupy a space in  $k_x$ ,  $k_y$ , and  $k_z$  domains, within a small bandwidth of frequencies,  $B_w$ , and width of viewing angles,  $BW_\phi = \Omega$  and  $BW_\Theta = \psi$ . So, the data grid in  $k_x - k_y - k_z$  space approaches an equally spaced linear grid. Thus, by taking this assumption into account, it possible to use IFFT in forming the 3D ISAR image. The 3D algorithm is based on the model in which a target point scatterer  $p(x_0, y_0, z_0)$ . The received signal in 3D case from the point scatterer in an angle of  $\Theta$  with the z-axis can be approximated as:

$$E^p(k, \phi, \Theta) = A e^{-j2\vec{k}\vec{r}} \quad (4.16)$$

Here,  $A$  is the amplitude of the back scattered signal,  $\vec{k}$  is the vector wave number in  $k$  direction,  $\vec{r}$  is the vector from center to point  $p$ . The "2" represents the two-way propagation between the radar and the image-point.



It is noteworthy, such as the 2D ISAR processing, the vector  $\vec{k}$  can be written in terms of the wave numbers in  $x$ ,  $y$ , and  $z$  directions as:

$$\vec{k} = k \cdot \hat{k} = k \cdot (\hat{x} \cdot \cos \alpha \cos \phi + \hat{y} \cdot \sin \alpha \sin \phi + \hat{z} \cdot \sin \alpha) \quad (4.17)$$

Similar to the previous section, Eq.4.17 provides three separate phase sentences as the function of the frequency variable,  $k$ , and the angle  $\Theta$  of view of  $i$  antenna position in horizontal-direction and the angle  $\phi$  of view of  $m$  antenna position in vertical-direction. Hence, this equation can be written for each  $f_k$  frequency and for each  $i$  and  $m$  antenna positions with complex numbers as below:

$$E(k, i, m) = I_{k,i,m} + jQ_{k,i,m} \quad (4.18)$$

It is obvious, the scatterer points  $p$  in the 3D ISAR image are located at  $(x_0, y_0, z_0)$ . So, the basic formula for radar image  $I(P_n)$  in a generic point  $p(x_0, y_0, z_0)$  is acquired by summing all signal contribution relating to the points as shown in Figure 4.9.

$$I(P_n) = \frac{1}{n_f n_p n_z} \sum_{i=1}^{n_p} \sum_{k=1}^{n_f} \sum_{m=1}^{n_z} E_{i,k,m} e^{\frac{4\pi f_k}{c} R_{i,m}} \quad (4.19)$$

Where  $n_f$  is the number of frequencies and  $n_p$  is the number of position in horizontal direction of the radar antenna and  $n_m$  is the number of position in vertical direction of the radar antenna.  $c$  is the speed of light. The distance between the point  $P_n$  and the  $i$  positions of the antenna in horizontal and  $m$  positions of the antenna in a vertical direction is  $R_{i,m}$ .

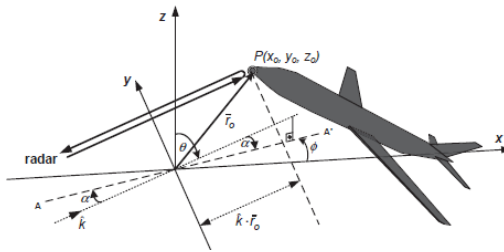


Figure 4.9: Geometry of 3D ISAR Imaging

As said in the section 2D ISAR processing, to avoid of longtime processing, a developed smarter algorithm has been used to focus on the image. As illustrated in Figure 4.10, the focusing algorithm can be extended to a 3D case, by accomplished radar measurement at different height of radar position. Therefore, the focused image in a generic point identified by  $p(x_0, y_0, z_0)$  is obtained by:

$$I(x_0, y_0, z_0) = \frac{1}{n_p n_z} \sum_{i,m} u_{i,m}(R_{i,m}(x_0, y_0, z_0)) \quad (4.20)$$

With

$$u_{i,m}(R_{i,m}(x_0, y_0, z_0)) = e^{j \frac{4\pi}{c} f_1 R_{i,m}(x_0, y_0, z_0)} IFFT_{n(R_{i,m}(x_0, y_0, z_0))}(E_{k,i,m}, F n_f) e^{j \frac{4\pi}{c} \frac{B_{3D}}{2} (R_{i,m}(x_0, y_0, z_0) - (n(R_{i,m}(x_0, y_0, z_0)) - 1) \Delta R)} \quad (4.21)$$

And

$$n(R_{i,m}(x_0, y_0, z_0)) = integer\left(\frac{R_{i,m}(x_0, y_0, z_0)}{\Delta R}\right) \quad (4.22)$$

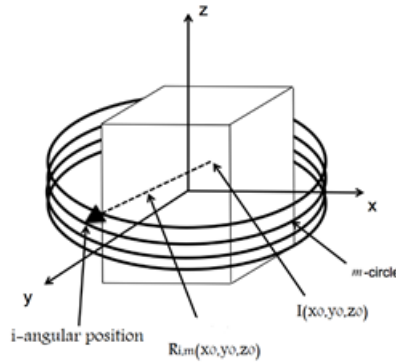


Figure 4.10: Geometry of 3D ISAR focusing algorithm

#### 4.7 The Measurement Equipment

In this section, the equipment used in ISAR measurements is introduced. A sketch of the measurement equipment is illustrated in Figure 4.11. A vector network analyzer (VNA-HP 8720A) operates as Continuous Wave Step Frequency (CWSF) transceiver. It is linked through microwave cables to a radar front-end kept on a tripod. As can be seen in Figure 4.12, the front-end radar consists of a TX amplifier with a gain of 10 dB, a RX amplifier with a gain of 20 dB, and a pair of single-pole double-throw (SPDT) switches that supply a direct path (through a  $-40$  dB attenuator) between the transmitter and the receiver in order to perform calibrated measurements not affected by the movements of the cables. The antennas are two equal horns linearly polarized, with rectangular aperture  $5.5\text{ cm} \times 7.5\text{ cm}$ , designed for operating in the band  $8\text{--}12\text{GHz}$ . A Band Pass Filter in the same band defines the noise bandwidth. The front-end can be rotated for obtaining measurements both in vertical and in horizontal polarization. Finally a Low Pass Filter at the end of the receiver chain cuts possible harmonic frequencies that amplifiers can introduce.

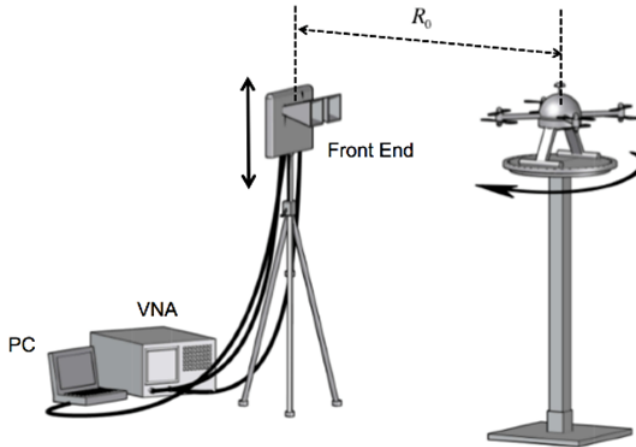


Figure 4.11: Sketch of the measurement equipment

With respect to the Figure 4.12, the target under test is located on the rotary platform exactly in front of the radar at  $R_0$  distance. It can be rotated step by step. The equipment performed a sweep of  $n_f$  frequency between 8 to

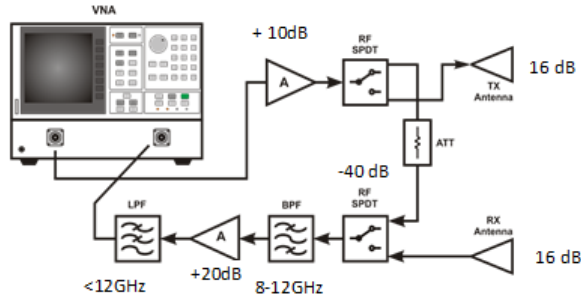


Figure 4.12: Block scheme of the radar-front-end

12 GHz with the switches connected to antennas and the second sweep with the switches connected to the attenuator ( $-40\text{ dB}$ ) in each  $i$  angular position. The final result is a normalized ratio relative to the calibration path for each frequency. At the end of a complete acquisition, a result is a matrix with complex numbers,  $E_{k,i,m}$ , where  $k$  index shows the numbers of frequency and  $i$  index related to the angular position and  $m$  shows vertical position.

#### 4.8 The UAV under Test

In this part, two different UAVs that have been tested, are described. The first is a toy drone, a SYMA X5SC-1 quadcopter, as shown in Figure 4.13. It is designed as a low-cost toy and not for professional use. It is powered by a built-in 500 mAh Li-Poli battery. The distance between motors is 16 cm and their height from the ground are 4.5 cm. The frame and the blades are a plastic material. The second one is a professional UAV, which is manufactured by Air-Vision, Figure 4.14. It has four pairs of motors with counter-rotating blades. Its body is carbon. It is powered by two 4600 mAh Li-Poli batteries which are housed in the leg. There is a dock for a camera below the head. The distance between the motors is 36 cm and the height of the motors from the ground is 22 cm.



Figure 4.13: SYMA quadcopter



Figure 4.14: Air Vision quadcopter

#### 4.9 Two-Dimensional ISAR Result

With the aim of obtaining the 2D image of SYMA quadcopter (Figure 4.13), the toy quadcopter was put on the rotary table. The antennas act in vertical polarization. The distance between the antennas and the rotation center was  $202\text{ cm}$ . The bandwidth was  $BW = 4\text{ GHz}$ , which used a Kaiser window with  $\beta = 5$ , gives an FWHM in a range equal to  $0.136\text{ m}$ . The angular step was  $1\text{ deg}$ . Figure 4.15 shows the 2D ISAR images in both logarithmic and numeric value. As shown in Figure 4.15, the shape of quadcopter can be easily detected and the four motors have a high signal.

The same measurements have been executed with the professional drone (Air Vision). Figure 4.16 shows the 2D ISAR images of Air Vision quadcopter in both logarithmic and numeric value. The shape of quadcopter can be easily identified but the highest signal is related to the motors, unlike the SYNA quadcopter.

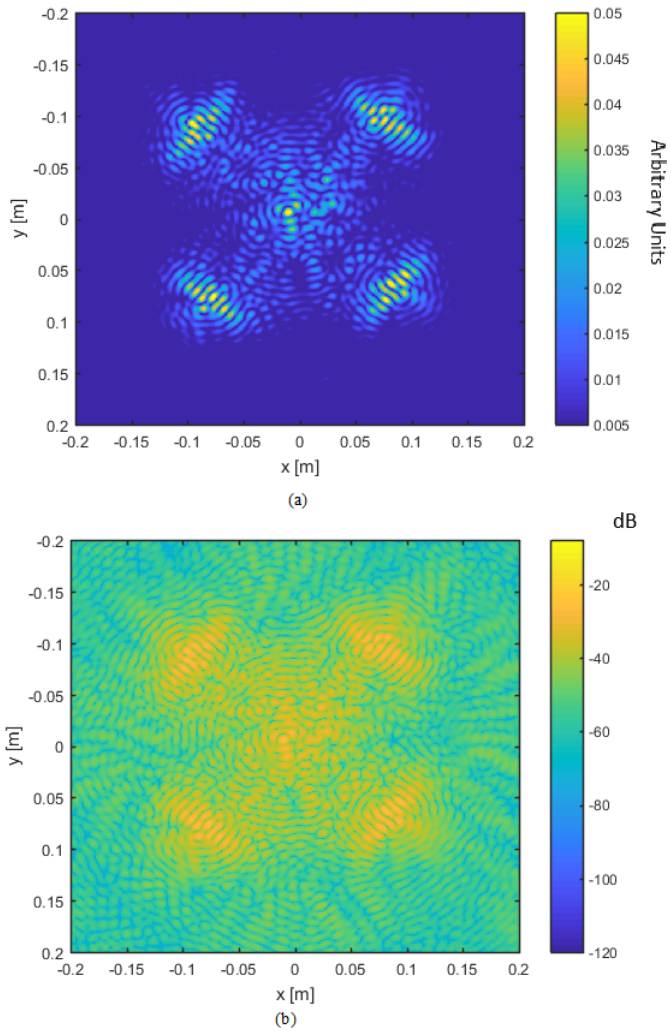


Figure 4.15: 2D-ISAR image of SYMA quadcopter (a)numeric (b)logarithmic

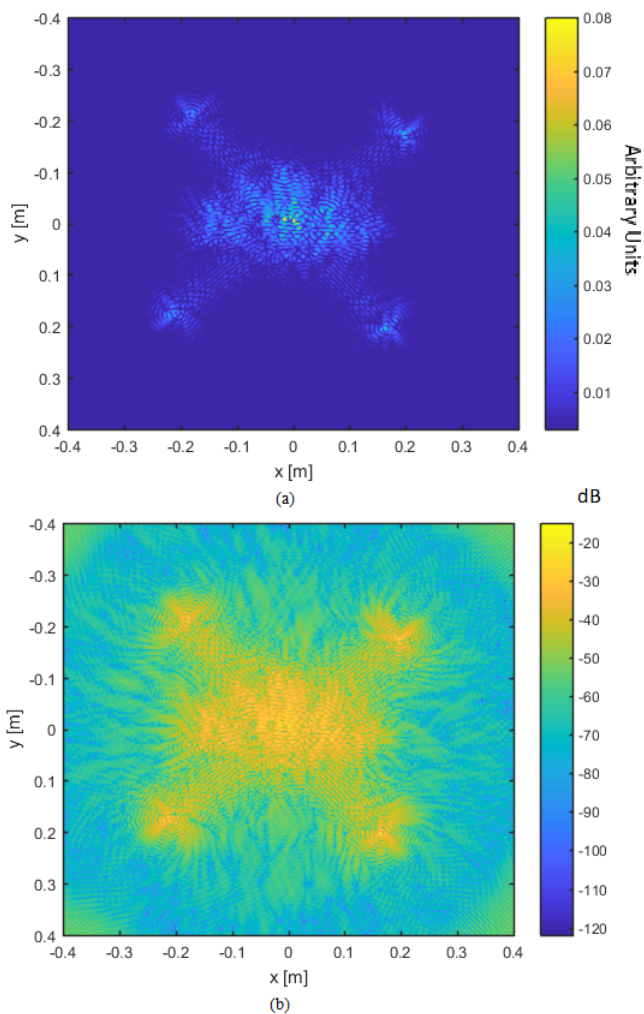


Figure 4.16: 2D-ISAR image of Air Vision quadcopter (a)numeric (b)logarithmic

It is important to note that there is a ripple due to cross range lobes in both 2D ISAR images of SYMA and Air Vision. The proposed solution to remove this ripple is to use the aperture windowing, which will be presented in the following.

#### 4.10 Three-Dimensional ISAR Result

With the aim of obtaining a 3D image of both quadcopter, the radar acquisition must be done at the different height of the rotation plane. The bandwidth was  $BW = 4\text{ GHz}$  and the distance between the antennas and the rotation center was  $150\text{ cm}$ . Figure 4.17 shows the 3D image of SYMA quadcopter when it is located on the rotary table in front of the radar. The height of the radar platform varied of  $18\text{ cm}$  at steps of  $1\text{ cm}$ . The four blades are clearly recognizable, as well as the central body.

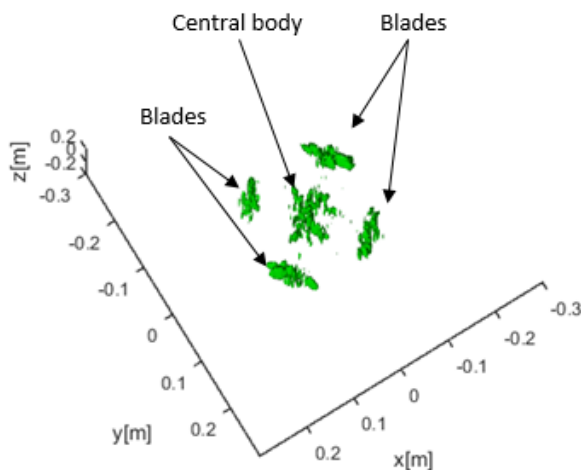


Figure 4.17: 3D-ISAR image of SYMA quadcopter

For obtaining the 3D image of Air vision the radar platform was varied of  $26\text{ cm}$  at steps of  $1\text{ cm}$ . Figure 4.18 shows the contour plot of the 3D image of the Air Vision. The shape of the motors are clearly recognizable, as well as the legs and the head of the quadcopter.

As mentioned in the 2D result section, there is ripple due to the cross-range lobes in both images of drone, which is removed by using aperture windowing.



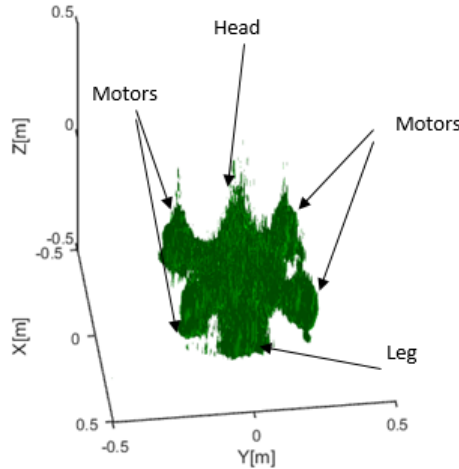


Figure 4.18: 3D-ISAR image of Air Vison quadcopter

#### 4.11 Aperture windowing

The basic idea of the windowing procedure, which has been used in this study is shown in Figure 4.19. Windowing procedure is carried out before focusing image. The rotation circle is divided into four arcs of  $180^\circ$  that are partially overlapping (to preserve the highest possible resolution). Afterward, at each arc is applied a Kaiser window separately in the chord of it. As illustrated in Figure 4.19, the chords are parallel to the x and y-axes. Finally, the ISAR images  $I(x_0, y_0, z_0)$  is obtained by summing the incoherently of four images. It means that The ISAR image is obtained by the amplitudes of four images and it is discharged the phase. The ISAR image after windowing is represented as follows:

$$I_w(x_0, y_0, z_0) = |I_1(x_0, y_0, z_0)| + |I_2(x_0, y_0, z_0)| + |I_3(x_0, y_0, z_0)| + |I_4(x_0, y_0, z_0)| \quad (4.23)$$

In the following, the effect of the aperture window is investigated by means of the point function of the Point Spread Function (PSF) of a single point. (Figure 4.20). The blue line is related to PSF which is calculated without any angular window. The red line is the PSF which is achieved by applying 4 windows. The black and green lines are PSF with 8 and 16 windows re-

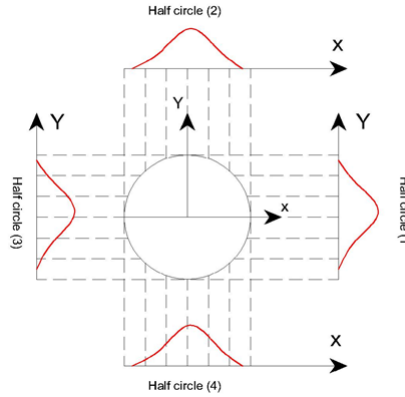


Figure 4.19: Windowing procedure

spectively. It should be noted that the result of PSF in 8 and 16 windows quite match with together. Please consider that the PSF of 8 windows (black line) is a bit better (a bit lower) than the 4 windows (red line), but due to a double-time increase in the computing time, there is no significant advantage to use it.

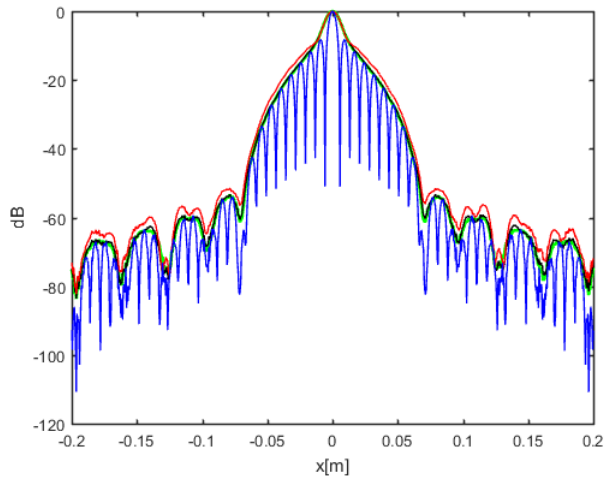


Figure 4.20: PSF with no window (blue line), with 4 windows (red line), 8 windows (black line), and with 16 windows (green line)

Figure 4.21 and Figure 4.22 show the obtained 2D ISAR images of the UAVs by applying 4 windows in both logarithmic and linear scale. The typical ripple due to the cross-range lobes is decreased. Its quality appears better.

To further investigate the effect of the aperture window to reduce the ripple, it has also been investigated in the 3D ISAR image of Air Vision. Finally, the Figure 4.23 demonstrates the 3D ISAR image Air Vision which is obtained with cross-range windowing.

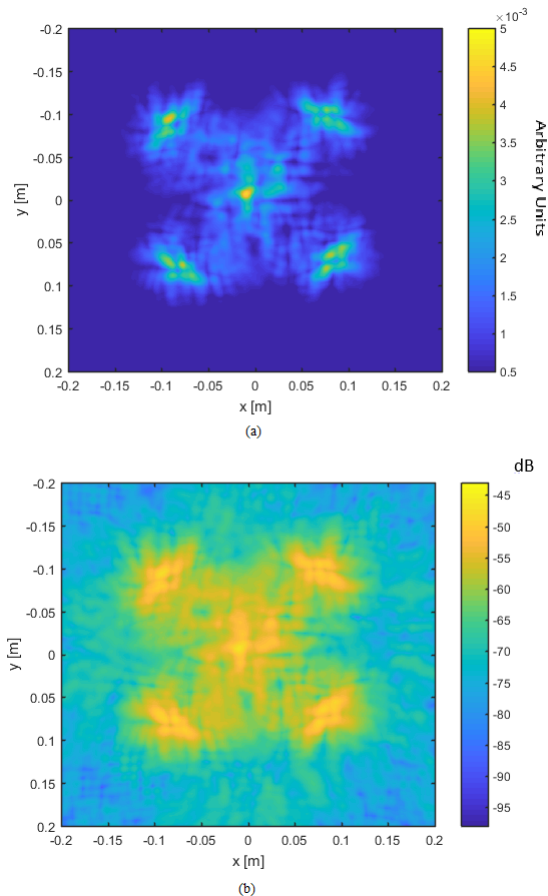


Figure 4.21: 2D-ISAR image of the SYMA using the windowing procedure (a)numeric (b)logarithmic

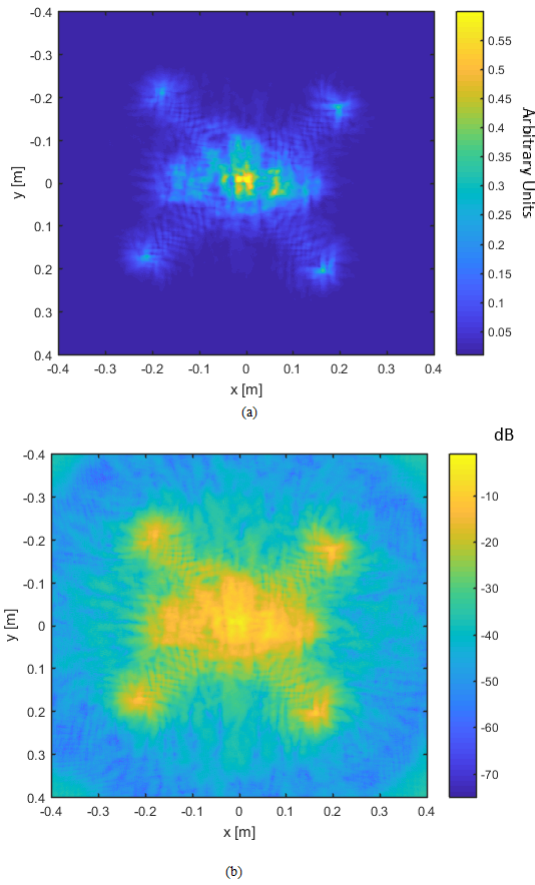


Figure 4.22: 2D-ISAR image of the Air Vision using the windowing procedure (a)numeric (b)logarithmic

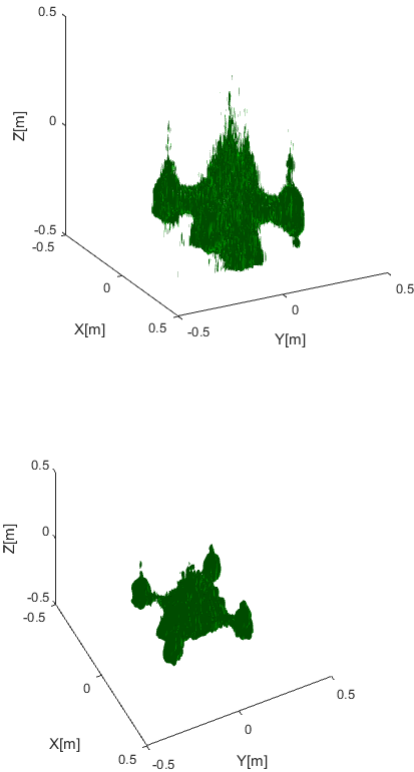


Figure 4.23: Views of the 3D-ISAR image of the Air Vision. The upper image is without windowing, while the lower is with windowing

#### 4.12 Conclusion

ISAR technique has been investigated to provide a detailed 2D and 3D processing. A 2D and 3D ISAR images of a toy drone and a professional quadcopter has been obtained, which captured images are clear and well-defined. Another finding that is noteworthy, is that by applying the aperture window, the ripple due to the cross-range lobes has been removed. Higher quality images have been created for 2D and 3D images.



# Chapter 5

## Bistatic 3D Ground Based Synthetic Aperture Radar

*Ground-Based Synthetic Aperture Radar (GB-SAR) systems are popular remote sensing instruments for detecting the ground changes of landslides, glaciers, snow avalanches, volcanoes, open pits, as well as for detecting small displacements of a large structure as bridges, dams. GB-SAR system can operate in both monostatic and bistatic configurations. In this chapter, a new GB-SAR system is presented, that is capable of generating both monostatic and bistatic images. Monostatic images are acquired in short times but they provide only 2D information about the targets. Bistatic images need long times (about several hours) but they provide 3D information of targets. It is worth noting that this new radar configuration can be considered as an upgrade of a linear monostatic GB-SAR. The bistatic 3D system shares the radar head and the horizontal mechanical axis with the conventional linear monostatic GB-SAR. This innovative solution has been patented by the author of this PhD thesis with her tutor and now it is a property of the University of Florence.*

### 5.1 Synthetic Aperture Radar (SAR) and SAR Geometry

Synthetic aperture radar (SAR) is a particular implementation of coherent radar imaging, which employs the movement of the radar platform and sig-

nal processing to produce high-resolution images. It was first considered by Wiley [28].

SAR system can operate into the modes of strip-map and spotlight. As shown in Figure 4.1(a), when the radar gathers the electromagnetic signal (EM) along the flight path, it detects a strip of a ground parallel to the flight path, which is known as strip - map. As shown in Figure 4.1(b), in the spotlight mode, the radar tracks and focuses its shining on a specific area of attention.

Figure 5.1 shows monostatic SAR geometry. In monostatic SAR configuration the transmitting and receiving antennas are placed at the same position. A signal propagates from the antenna that illuminates the surface of the earth. As shown in Figure 5.1, the earth region lighted by the signal is called the antenna's footprint. The bright ground area included a large number of small point targets where each point target reflects the back scattered signal to the antenna. The direction of azimuth is defined as the direction aligned with the speed vector of platform (Figure 5.1). The range direction is along the distance from the antenna to the point target and it is perpendicular to the azimuth direction. Range is measured by the round trip propagation delay of the radar signal [29, 30].

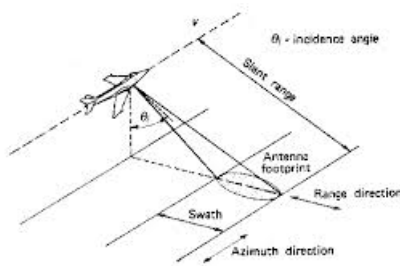


Figure 5.1: SAR Geometry

## 5.2 Ground Based Synthetic Aperture Radar

There are several types of SAR systems based on their own platform. They are divided into space borne, airborne and ground-based SAR (GB-SAR) systems. Space borne and airborne systems are commonly used for a wide range of applications, but nonetheless, the ground-based systems also have



many applications and are used in research activities [31–33]. General speaking, the space borne systems work at a far distance, so when the observation zone is small, the GB-SAR is more useful than the space systems. One of the applications of the GB-SAR system is to measure the displacement of a target such as a ground movement. Performing these measurements allow to understand the dynamic changes of landslides for preventing natural disasters [34].

### 5.3 Bistatic SAR and Bistatic SAR Geometry

In general, the bistatic radar consists of one transmitting antenna and one receiving antenna at different locations. It is an evident difference between the bistatic and monostatic case and the use of a bistatic configuration is more useful than the monostatic in some applications. For instance, the classification of objects is improved in bistatic SAR images [35, 36]. One of the significant features in bistatic systems is using receivers in different locations which are leading to scenes from different points of view [37–39]. Figure 5.2 shows the bistatic SAR geometry with a target, and it is known as the bistatic triangle. Bistatic SAR geometry illustrates the transmitter (Tx), receiver (Rx) and the target. The distance  $L$  between transmitter and receiver is called baseline. Generally, in the case of a monostatic radar  $L = 0$  and in the bistatic case is  $L \neq 0$ .  $R_1$  and  $R_2$  indicate the target-transmitter and target-receiver distance respectively. The angles,  $\Delta_T$ , and  $\Delta_R$  are transmitter and receiver viewing angles, respectively.  $\beta$  denotes bistatic angle which is  $\beta = \Delta_T - \Delta_R$ , and its limits are from zero up to  $180^\circ$ ,  $0^\circ \leq 180^\circ$ . The line that bisects the bistatic angle is the bistatic bisector [39–41].

### 5.4 Bistatic Radar Equation

Bistatic radar equation is computed as follows:

$$P_R = P_T \cdot \frac{G_T}{4\pi R_1^2} \cdot \sigma_b \cdot \frac{G_R}{4\pi R_2^2} \cdot \frac{\lambda^2}{4\pi} \quad (5.1)$$

Where  $P_R$  is the transmit power and  $P_T$  is the received signal power,  $G_T$  is the transmit antenna gain,  $G_R$  is the receive antenna gain.  $R_1$  denotes the transmitter-target distance while  $R_2$  is the target-receiver distance.  $\lambda$  is the radar wavelength and  $\sigma_b$  is the bistatic RCS of target [39].

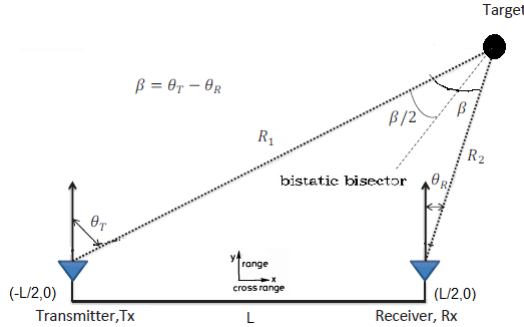


Figure 5.2: Bistatic SAR Geometry

### 5.5 The Bistatic GB-SAR Working Principle

Given the bistatic geometry, the most evident difference of a bistatic radar with respect to a monostatic radar is the separate positions of the transmitter and the receiver. Figure 5.3, shows the sketch of the bistatic GB-SAR we have designed. A linear monostatic GB-SAR with transmitting and receiving antennas moves along a horizontal rail (along the x-axis) obtaining interferometric 2D images. For operating in bistatic mode, the radar head has a second transmitting channel. By using the second channel, the radar transmits to a complementary antenna that moves vertically (z-direction) along a mechanical rail. The vertical rail is located at distance  $y_0$  behind the horizontal rail in correspondence of its central point. The lower position of the antenna which moves vertically is at  $z_0$  over the x-axis. There is a link between the radar head and the complementary antenna through an RF cable of length  $L_0$ . In this bistatic configuration, the radar system is able to obtain data with spatial diversity in both direction (x and z) therefore, it is able to obtain a 3D image of the targets in its field of view.

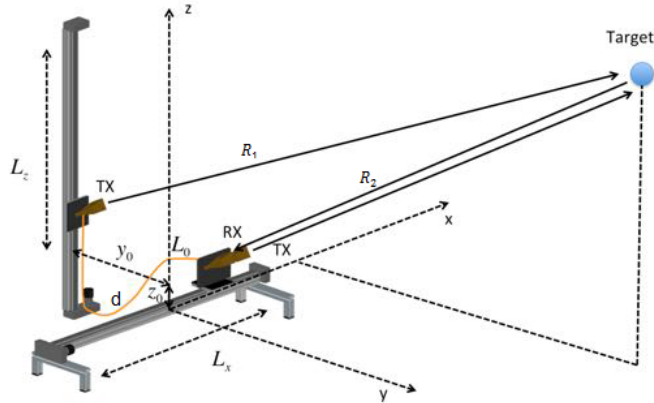


Figure 5.3: Working principle of the Bistatic / Monostatic GB-SAR

## 5.6 Bistatic Range and Cross-Range Resolution

Figure 5.4, refers to the resolution in bistatic geometry.

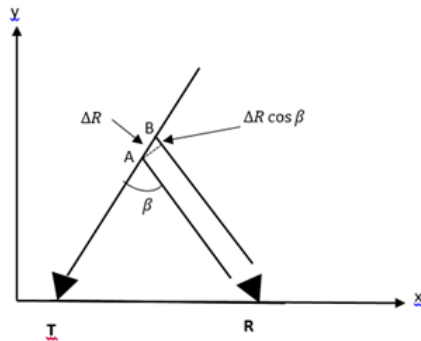


Figure 5.4: Bistatic range Resolution

By considering the path of TAR and TBR, the separation between two target echoes at the receiver is conventionally taken bigger than time resolution of  $\frac{c}{B_w}$  where  $B_w$  is the bandwidth of the transmitted signal. So, the bistatic range can be expressed as follows:

$$\Delta R + \Delta R \cos \beta = \frac{c}{B_w} \quad (5.2)$$

That can be rewritten as:

$$\Delta R = \frac{c}{2B_w} \cdot \frac{1}{\cos^2 \frac{\beta}{2}} \quad (5.3)$$

The Eq.5.4, shows that the bistatic range resolution degrades by  $\cos^2 \frac{\beta}{2}$  compared to the equivalent monostatic radar. When  $\beta = 0$  the range of the bistatic radar is equal to the range of the monostatic radar.

The Eq.4.7 gives the angle resolution for a monostatic SAR. Where  $D$  is the dimension of the synthetic aperture antenna [39].

With reference to Figure 5.3, we should note that transmitting from point  $A$  and receiving from point  $B$  is equivalent to transmit and receive from the median point  $C$ . In this way, we can see the bistatic GB-SAR is a "Pseudo-monostatic" geometry.

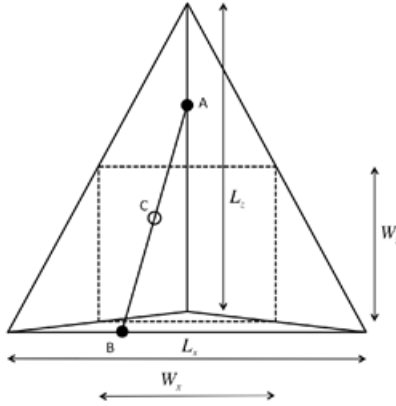


Figure 5.5: Geometry for angle resolution of Bistatic SAR

Although for a constant location of the vertical antenna, the locus of points of the bistatic mode associated with the horizontal movement of the antenna explaining an arc, the total locus of the medium points (by considering all the vertical positions) is the small dotted rectangle. Hence, the bistatic resolution in the azimuth direction,  $\Delta\phi_b$ , and in the elevation direction,  $\Delta\Theta_b$ , is computed as follows [42]:

$$\Delta\phi_b \approx \frac{\lambda}{2W_x} \quad \Delta\Theta_b \approx \frac{\lambda}{2W_z} \quad (5.4)$$

Where  $W_x$  and  $W_z$  are two sides of the small dotted rectangle in Figure 5.5. By assuming that the lower position of the complementary antenna is near to the horizontal scan,  $W_z \approx L_z/2$ . Accordingly the Eq.5.4 can be written as follows:

$$\Delta\phi_b \approx \frac{\lambda}{L_x} \quad \Delta\Theta_b \approx \frac{\lambda}{L_z} \quad (5.5)$$

In other words, the azimuth resolution of the bistatic images is worse than monostatic images by a factor 2.

### 5.7 Radar Interferometry

In process of forming a SAR image, the result is a matrix of complex numbers. It is noteworthy that the phase is usually eliminated and only the magnitude is shown. Interferometry is obtained by using coherent data at instants of time or from distinct viewpoints. SAR interferometry (InSAR) is a technique for exploiting coherent data included a phase difference of two SAR images, which is taken from different viewpoints or at instants of time [43, 44].

The features of information that may be extracted can be defined by the exact nature of the two images. Typically, images were taken in a cross-track (from different observing geometries) leads to the topography of imaged scene and images that obtained in an along-track (from similar geometries but with a slight time delay) lead to the determination of the velocity of moving objects. An interferometric data set is often obtained in repeat-pass mode. In this case, when it retraces a path as closely as possible a radar platform collects two datasets. The major problem in these collections is the suffering from temporal decorrelation and atmospheric distortion derived from the difference in acquisition times of the two datasets [45, 46].

The interferometric technique is based on measuring the relative range differences by comparing the phase terms of two images, indicated as master and slave. For each pixel, the phase difference is computed by the argument of the pointwise multiplicities complex master image  $M$ , comprising the in-phase and quadrature components  $I$  and  $Q$ , in the corresponding conjugate

of the slave image  $S^*$ . Figure 5.6 shows the interferometric measurements of acquisitions obtained at the same position at two different instants of time,  $\Delta T = t_1 - t_0$ . The displacement,  $d$ , of the deformation for each pixel is as follows:

$$d = -\frac{\lambda}{4\pi} \arg(M.S^*) = -\frac{\lambda}{4\pi} \Delta\phi \quad (5.6)$$

Where  $\lambda$  is the wavelength, "arg" displays the argument function of complex numbers and  $\Delta\phi$  is the phase difference of each pixel between the two SAR images which is in the interval  $[-\pi, \pi]$ .

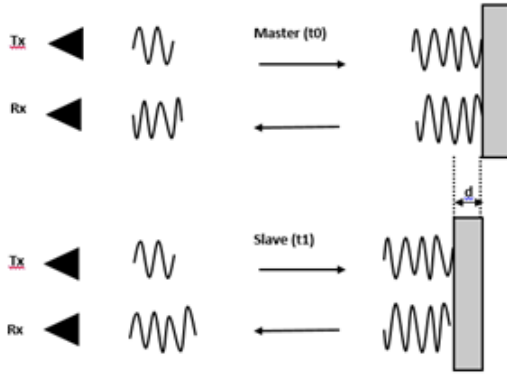


Figure 5.6: Interferometric measurements of acquisitions obtained at the same location at two different instants of time,  $t_1-t_0$

In order to calculate the interferogram, they must be acquired in the same position. The system must be carefully shifted in duplicate measurements, and the images recorded in the post-processing. Since the compared images are obtained at different moments of time, the conditions of atmospheric must be considered. Therefore, the changes in the diffraction index, because of humidity, pressure, and temperature, will result in a change in the speed of wave propagation, which may cause an error in the range measurements. The phase differences are rewritten by using the atmospheric contributions and ambiguity errors as follows [47]:

$$\Delta\phi = \Delta\phi_t + \Delta\phi_{atm} + \Delta\phi_{noise} - 2\pi n \quad (5.7)$$

Where  $\Delta\phi$  represents the interferometric phase,  $\Delta\phi_t$  is true phase difference,  $\Delta\phi_{atm}$  is the atmospheric section,  $2\pi n$  is the phase ambiguity where  $n$  is the integer phase ambiguity, and  $\Delta\phi_{noise}$  is noise. Range changes are assessed by using SAR interferometry. The complex interferogram is as follow:

$$I = M.S^* \quad (5.8)$$

Where,  $I$ , is the interferogram,  $M$  is the Master image,  $S$  is the Slave image and  $\langle.\rangle^*$  is the complex conjugate.

Figure 5.7 shows interferogram maps of two SAR images. This interferogram map shows the phase shift spatially between two SAR images when they obtained from the same area at different times.

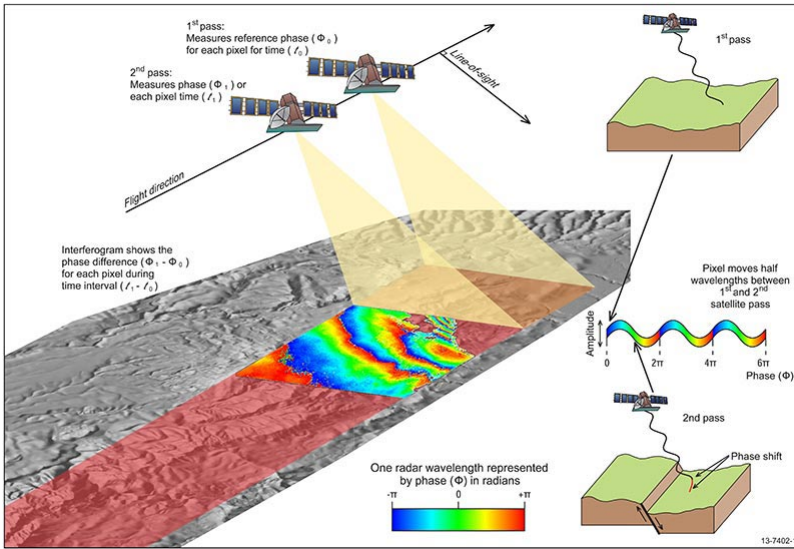


Figure 5.7: Interferometric measurements of acquisitions (Geoscience Australia)

## 5.8 The Bistatic Focusing Algorithm

General speaking, the result of a measurement is a matrix  $E_{i,m,n}$  of  $N_f \times N_x \times N_z$  complex numbers ( $I_{i,m,n} + jQ_{i,m,n}$ , where  $I_{i,m,n}$  is in-phase and  $Q_{i,m,n}$  is quadrature components at  $i$ -th frequency ( $1 < i < N_f$ ) in the

$m$ -th position of x-axis ( $1 < m < N_x$ ) and the  $n$ -th position of z-direction ( $1 < n < N_z$ ).

$$E_{i,m,n} = I_{i,m,n} + jQ_{i,m,n} \quad (5.9)$$

The images can be focused in the 3D space in front of the radar, by taking into account the path radar head-complementary antenna -image point. With referred to Figure 5.3, the basic formula for obtaining a three-dimensional image  $I(x, y, z)$  is the following [42]:

$$I(x, y, z) = \frac{1}{N_f N_x N_z} \sum_{i,m,n} E_{i,m,n} e^{j \frac{2\pi}{c} f_i (R(x,y,z,m,n))} \quad (5.10)$$

$$R(x, y, z, m, n) = R_1 + R_2 + d \quad (5.11)$$

Where  $R_1$  is the distance between the image-point and the  $n$ -th position of the supplementary antenna,  $R_2$  is the distance between the image-point and  $m$ -th position of the radar along the rail in x-axis, finally,  $d$  is the length of cable between the antenna of the monostatic GB-SAR and supplementary antenna.

By using Eq.5.10 images result with high side lobes. Therefore we applied suitable windows to the matrix  $E_{i,m,n}$  to reduce side-lobes in range and cross-range before to focus it. For instance, by using a Kaiser window with  $\beta = 5$  the side-lobes was reduced in range and cross-range of about 30 – 40 dB (along an x-axis: Azimuth and z-axis: Elevation). The Eq.5.10 is computationally heavy, so we have used the focusing algorithm that reduces computational calculations without a considerable reduction in the accuracy and precision. The modified focusing algorithm which is used is an improved version of the back-propagation algorithm described in [19]. First zero-padding and IFFT are applied along  $i$ -index of factor  $F$ . It means that each column of matrix  $E_{i,m,n}$  along frequency will have  $FN_f$  elements. Thus, the focusing algorithm can be written as follows:

$$I(x, y, z) = \frac{1}{N_x N_z} \sum_{i,m,n} E_{m,n} u(R(x, y, z, m, n)) \quad (5.12)$$

$$u(R, m, n) = e^{j \frac{2\pi}{c} f_1 R} IFFT_{n(R)}(E_{i,m,n}, FN_f) e^{j \frac{\pi}{c} \frac{B_w}{2} (R - (k)R - 1) \Delta R} \quad (5.13)$$

$$k(R(x, y, z, m, n)) = integer\left(\frac{R(x, y, z, m, n)}{\Delta R}\right) \quad (5.14)$$



$$\Delta R = \frac{c}{2N_f F \Delta f} = \frac{N_f - 1}{FN_f} \frac{c}{B_w} \quad (5.15)$$

Where  $\Delta R$  is the range step and  $f_1$  is the first frequency of bandwidth  $B_w = FN_f - f_1$  and  $\Delta f$  is the frequency step. The precision of algorithm is related to the padding factor  $F$ . The better result can be achieved with the larger factor. We used  $F = 50 - 100$ .

### 5.9 The Bistatic Radar Prototype

A GB-SAR prototype has been assembled for testing the working principle (see Figure 5.8).

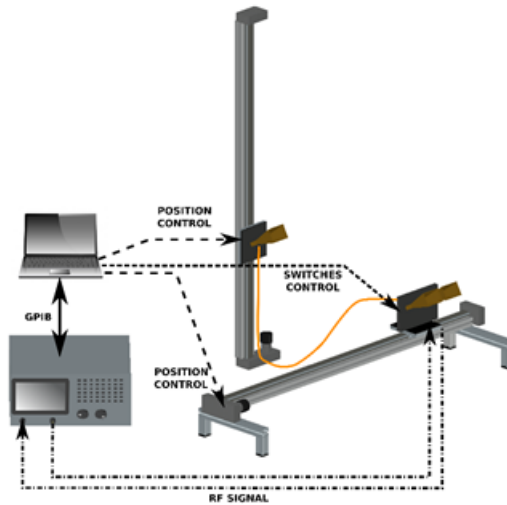


Figure 5.8: Sketch the GB-SAR prototype

A vector network analyzer (VNA) HP8720D operated as transceiver providing a continuous wave stepped-frequency signal (CWSF) in X-band with central frequency  $f_c = 10 \text{ GHz}$  and bandwidth  $B_w$ . With respect to Figure 5.9 the VNA output power was  $0 \text{ dBm}$ , the one-way cable loss was  $-5 \text{ dB}$ , TX amplifier gain was  $10 \text{ dB}$ . The RX receiver gain was  $20 \text{ dB}$ . Two RF cables linked the VNA to the frontend moving along the horizontal mechanical axis. Two single pole double-throw (SPDT) switches provided a direct

path between the transmitter and the receiver in order to perform calibrated measurements. A third SPDT switched between the two TX antennas. For every single step along the horizontal mechanical rail, the radar accomplishes the two acquisitions (monostatic and bistatic). A monostatic acquisition is complete after  $N_x$  steps when the radar head has swept the horizontal axis, while the bistatic acquisition is complete only after  $N_z$  horizontal scans, i.e. after  $N_x \times N_z$  steps. The two mechanical axes spanned up to  $1.50\text{ m}$  along x-axis and up to  $1.50\text{ m}$  along z-axis.

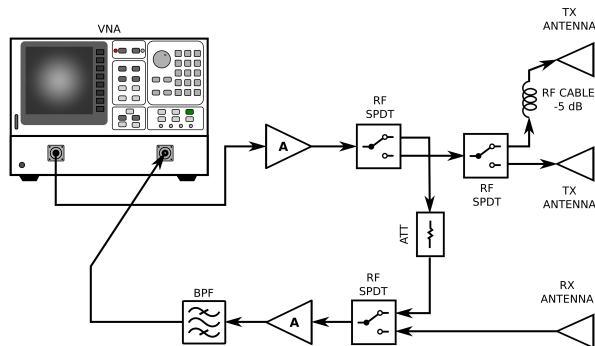


Figure 5.9: Block scheme of radar front-end

### 5.10 Experimental Test

The radar was installed in the garden of the University of Florence to test the equipment in a controlled environment. Figure 5.10, represents the map of the test field. The experiment was performed twice with two different targets. The first test was carried out with two corner reflectors (CR) in front of the radar. A corner reflector of  $0.4\text{ m}$  side was placed on the tip of  $3.0\text{ m}$  high wood pole. The pole was about in front of the radar in  $17.1\text{ m}$  distance. A second corner reflector of  $0.27\text{ m}$  side was placed on a tripod (height from ground:  $1.2\text{ m}$ ) on the right side of the radar. Figure 5.11, illustrates both tested CR.

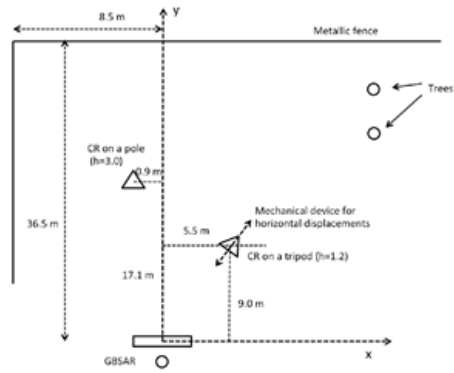


Figure 5.10: Map of the test field



Figure 5.11: Picture of both tested CR

The radar parameters are listed in Table 5.1.

Table 5.1: Radar parameter in the first test

$B_w$	$L_x$	$L_z$	$N_x$	$N_z$	$y_0$	$z_0$	$L_0$
160 MHz	1.5 m	1.02 m	150	102	0.63 m	0.19 m	4.00 m

Figure 5.12, displays one of many monostatic images that have been acquired during the complete 3D bistatic acquisition. The acquisition time of every single monostatic image was 25 minutes while the complete 3D bistatic acquisition is almost about 42 hours. In monostatic images both the corner reflector on the pole and the corner reflector on the tripod are visible. It is obvious that it is not possible to estimate their heights. During the bistatic test, the second CR was located on a tripod and could be moved along the direction of view, by exploiting a mechanical device with 0.1 mm nominal accuracy.

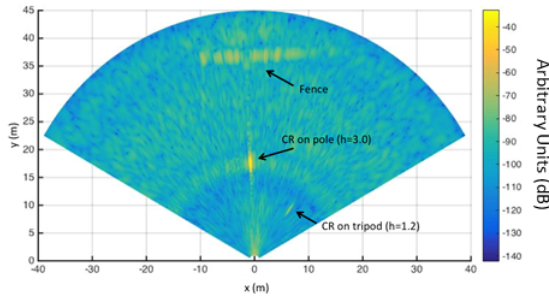


Figure 5.12: Monostatic image

Figure 5.13, shows the nominal and the measured displacement of the corner reflector during 102 acquisitions. The mean error was 0.13 mm.

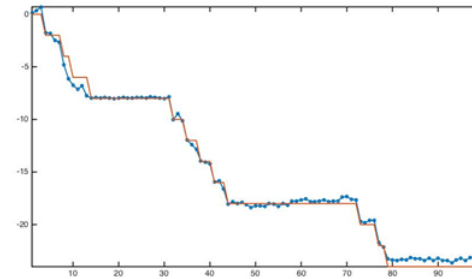


Figure 5.13: Measured and nominal displacement of the CR on the tripod

Figure 5.14 and Figure 5.15 show the bistatic images when the whole 3D

bistatic acquisition was complete. The bistatic focused image has been done in two different heights. Figure 5.14 shows the bistatic image focused in the horizontal plane  $z = 3.0 \text{ m}$ , while Figure 5.15, shows the bistatic image focused in the horizontal plane  $z = 1.0 \text{ m}$ . As shown in Figure 5.14, the CR on the tripod, the pole, and the metallic fence can be seen while in the upper plane ( $z = 3$ ) plane the CR on the tip of the pole is only visible and the CR on the tripod is not visible and the metallic fence exhibits just a weak light.

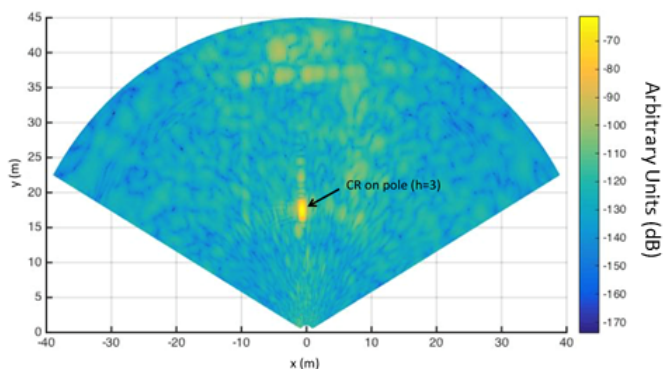


Figure 5.14: Bistatic image focused in the horizontal plane  $z=3.0 \text{ m}$

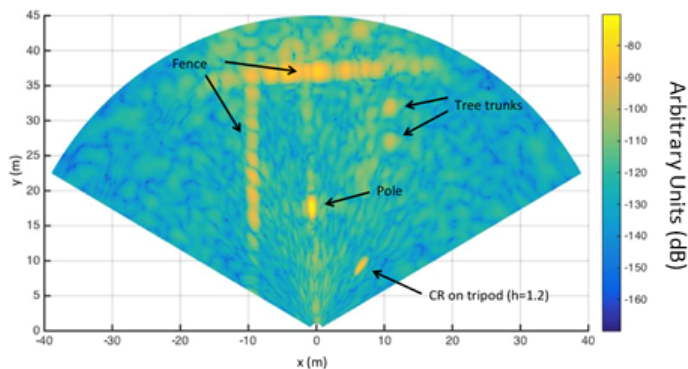


Figure 5.15: Bistatic image focused in the horizontal plane  $z=1.0 \text{ m}$

Figure 5.16 shows the bistatic image focused in the vertical plane at  $x = -1 \text{ m}$ . The radar fence and CR on the tip of the pole at  $3.00 \text{ m}$  height are visible.

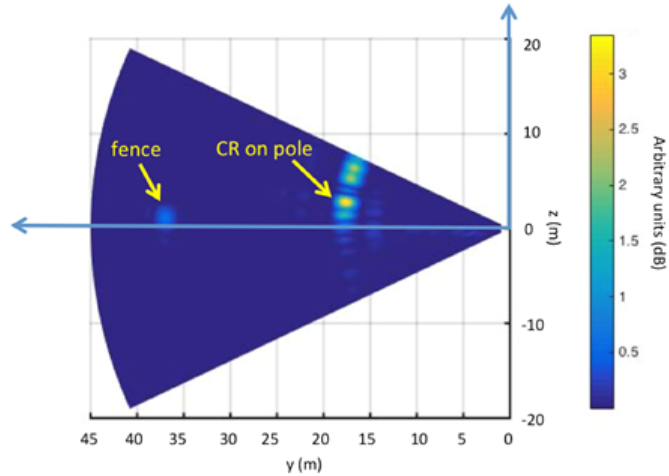


Figure 5.16: Bistatic image focused in the vertical plane  $x=-1.0 \text{ m}$

The second test was accomplished for a seven-storey building, in order to test the equipment in a more realistic scenario. The distance between the radar and building was 140. Figure 5.17 shows the view of the building. The radar parameter in this case listed at table 5.2.

Table 5.2: Radar parameter in the second test

$B_w$	$L_x$	$L_z$	$N_x$	$N_z$	$y_0$	$z_0$	$L_0$
80 MHz	1.5 m	1.5 m	150	150	0.62 m	0.21 m	4.00 m



Figure 5.17: Picture of building

The monostatic image is shown in Figure 5.18. The facade of the building is visible by the clear slant lines.

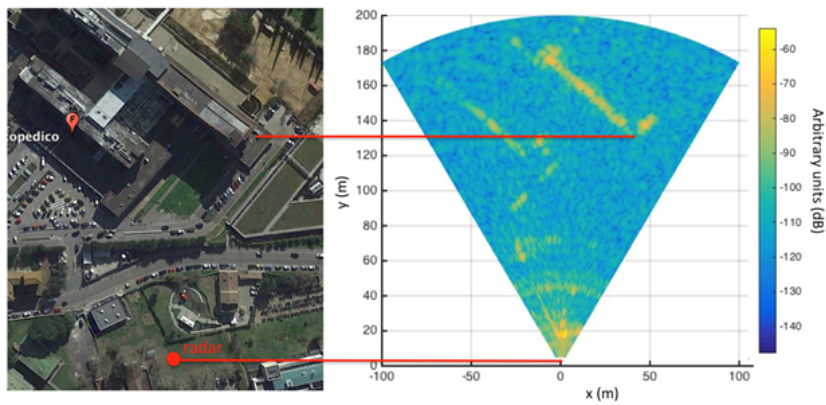


Figure 5.18: Monostatic image of building

Figure 5.19 shows the bistatic image focused in a horizontal plane at  $z = 10$  with respect to the radar. The image is good but, as anticipated, the resolution is worse.

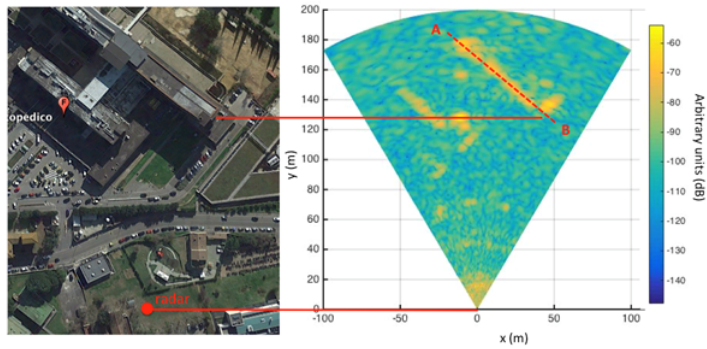


Figure 5.19: Bistatic image of building focused in the horizontal plane at  $z=10$  m

Figure 5.20 shows the bistatic image focused in the vertical plane. Crossing the two points (A and B) in Figure 5.20 indicate the side wall of the building which focused on the vertical plane.

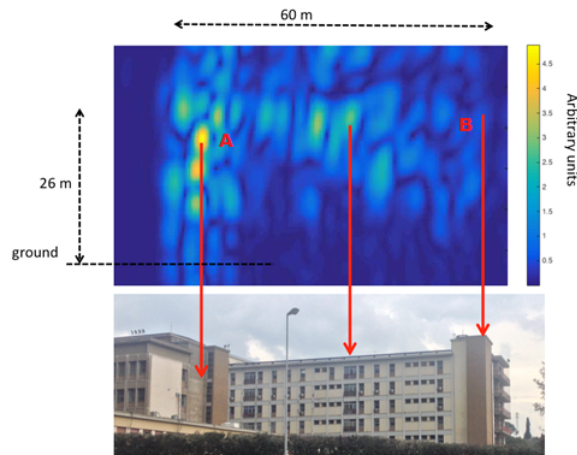


Figure 5.20: Bistatic image focused in the vertical plane



Finally, the 3D bistatic image is obtained by focusing on the whole tridimensional space in front of the radar. Figure 5.21 and Figure 5.22 illustrate the 3D bistatic images, the facade of the building is an evident target in the 3D space when a threshold is applied in an amplitude equal to 1.7% of the maximum value.

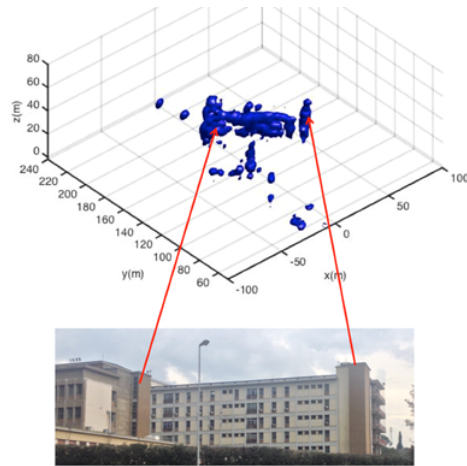


Figure 5.21: Bistatic 3D image

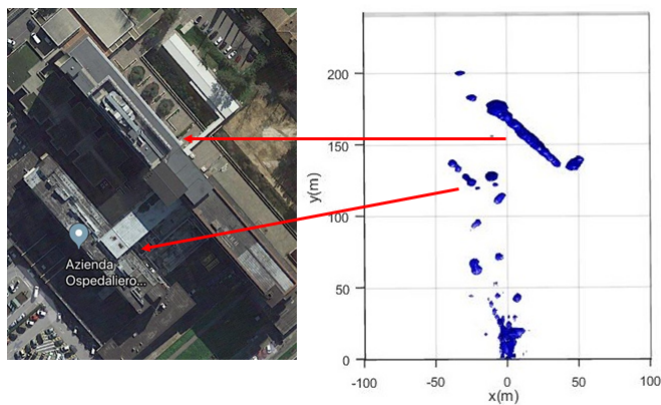


Figure 5.22: Bistatic 3D image in xy direction

### 5.11 Conclusion

In this study, a new approach to bistatic radar imaging was presented. A bistatic radar technique by means of a moving transponder was utilized to acquire a high resolution 3D bistatic SAR images in long times (several hours), which simultaneously acquire 2D images in short times (about a half hour). Another significant approach of this paper is that the suggested imaging technique can be used for interferometry in each horizontal plane. It is worth mentioning that this novel radar configuration has been obtained as an upgrade of a linear monostatic GB-SAR.

# Chapter 6

## Compressive Sensing Applied To Ground Based Synthetic Aperture Radar

*One of the most intriguing processes in some aspects of signal processing, statistics, and computer science is data compression. The Shannon/ Nyquist theorem is the basis for sampling signals or images, through which the sampling rate should be at least twice the maximum frequency available in its bandwidth. Compressive Sensing (CS), however, is a new approach which promises to recover images and signals from a small number of random samples or measurements data better than the traditional way. Compressive sensing is able to compress data when the signal is sparse. This chapter presents an overview of the CS aspects, especially for its application to GB-SAR [48, 49].*

### 6.1 Shannon-Nyquist theorem

The Shannon/ Nyquist theorem is the conventional method of sampling signals or images, through which the sampling rate should be at least twice the maximum frequency available in its bandwidth. In order to obtain a high-quality SAR image and to prevent the spatial aliasing problem in radar applications, the SAR measurement should meet some requirements provided by the Nyquist sampling theorem. The Nyquist Sampling Rate should be considered the lowest possible sampling rate. When we consider a spatial sampling, the step  $\Delta x$  should be less or equal than a quarter of the minimum wavelength of the radar signal. This requirement is:

$$\Delta x = \frac{\lambda_{min}}{4} \tag{6.1}$$

Where,  $\lambda_{min}$ , is the minimum wavelength of the signal and the  $\Delta x$  indicates the maximum distance between two data acquisition points. If the measurement breaks these requirements, the SAR image has ambiguity, which may create artifacts. By considering a continuous wave step frequency (CWSF) radar, a signal is constantly transmitted with increasing frequency, and the reflected signal is recorded to be processed for generating the radar image. Hence, the frequency response measured by the radar is sampled in the frequency domain with sampling interval  $\Delta f$ . Accordingly to Nyquist:

$$\Delta f = \frac{c}{2R_m} \tag{6.2}$$

Where  $c$  is the speed of light, and  $R_m$  is the unambiguous range in the radar image. A wide bandwidth is required for the radar signal to obtain a high range resolution [50, 51].

## 6.2 Compressive Sensing

An alternative method is recently emerged for sampling and reconstructing data which is called "compressive sensing". This theory expresses that the signals and the images can be reconstructed from much below data that is usually required by the Nyquist theorem. In fact, CS theory is able to reconstruct signals and images with a few samples. To make this possible, CS relies on two requirements: sparsity and incoherency [49, 52].

### 6.2.1 Sparsity and Compressible Signals

Sparsity depends on the signal of interest. compressive sensing relies on the fact that many natural signals are sparse or compressible if they are expressed by a suitable basis ( $\Psi$ ). Consider  $x$  is a one-dimensional, discrete time signal with length  $N$  in  $R^N$ , i.e. a  $N \times 1$  column vector. Each  $x$  signal in  $R^N$  can be displayed in terms of a basis matrix  $\Psi$  which is orthonormal. The size of basis matrix is  $N$  with the vectors  $\{\Psi_i\}_{i=1}^N$ . Therefore the signal  $x$  can be written in  $\Psi$  domain as:

$$x = \Psi s \qquad x = \sum_{i=1}^N s_i \Psi_i \qquad (6.3)$$

Where  $s$ ,  $N \times 1$ , is the vector of weighting coefficients. With respect to the Eq.6.3, it is obvious that  $x$  and  $s$  are equivalent representations of the signal when  $x$  is in the time or space domain and  $s$  is in the  $\Psi$  domain. If the Eq.6.3 has just a few large coefficients and many small coefficients, the signal  $x$  is compressible. In other words, the signal  $x$  is  $k$ -sparse if only  $k$  elements of vector  $s$  are greater than zero, and the others are quite or almost zero. It means that a large proportion of the coefficients are discarded without loss of information [53].

### 6.2.2 Incoherence

Incoherence is related to the property of the sensing matrix or measurement matrix ( $\Phi$ ), which determines the capability to recovery  $\Phi$ . In other words, incoherency measures the maximum similarity between row and column vectors of two matrix  $\Phi$  and  $\Psi$ . The incoherence property ( $\mu$ ) is:

$$\mu(\Phi, \Psi) = \sqrt{N}. \max_{1 \leq k, j \leq N} |\langle \Phi_k, \Psi_j \rangle| \qquad (6.4)$$

Where  $N$  indicates the number of elements in the signal,  $k$  and  $j$  are indices of column and row. Incoherence is limited to  $\mu(\Phi, \Psi) \in [1, \sqrt{N}]$ . When  $\Phi = \Psi$ ,  $\mu(\Phi, \Psi) = \sqrt{N}$  and if  $\mu(\Phi, \Psi) = 1$  the  $\Phi$  and  $\Psi$  are maximally incoherent. For reconstructing a sparse signal a low similarity is needed between  $\Phi$  and  $\Psi$ , therefore, the incoherence property determines the number of samples  $M$ , which are needed to reconstruct the sparse signal from the existing measurements by:

$$M \geq C.\mu^2(\Phi, \Psi).S.\log N \qquad (6.5)$$

Where  $S$  is the number of nonzero components,  $C$  is some positive constant, and  $N$  is the size of the sparse signal. When  $\mu(\Phi, \Psi) = 1$  fewer samples are needed to reconstruct signal but if  $\mu(\Phi, \Psi) = \sqrt{N}$ , there is no guarantee to recover the signal from a limited number of samples. It should be noted

that the signal can be reconstructed with probability exceeding  $1 - \delta$  if  $M \geq C \cdot \mu^2(\Phi, \Psi) \cdot S \cdot \log \frac{N}{\delta}$ , where  $\delta$  is the isometry constant. It means that when the coherence is small the fewer samples are required. Eq.6.5, shows  $M \log N$  samples are needed to reconstruct a sparse signal if  $\mu = 1$  [49,53,54].

### 6.3 Compressive Sensing Algorithm

By considering a length- $N$ , real-value signal  $x$ , according to the CS a sampled vector  $y$ , with the size of  $M \times 1$  can be written as [49,53,55]:

$$y = \Phi x + d \tag{6.6}$$

Where  $\Phi$  is an  $M$  measurement matrix, where  $M$  is the number of measurements ( $M \ll N$ ). The  $d$  denotes additive noise. The signal  $x$  is  $k$ -sparse in the basis matrix,  $\Psi$ . The basis matrix with size  $N \times N$  is determined as the relation between the signal in its sparse domain with the signal in the measurement domain. So, the signal  $x$  in a sparse domain is as follows:

$$x = \Psi s \tag{6.7}$$

Where  $s$  is the vector of weighting coefficients with the size of  $N \times 1$ . It is worth mentioning that only  $k$  elements of vector  $s$  are bigger than zero, and the others are quite or almost zero. Considering the second requirement of the CS, incoherency, which is a relationship between the measurement matrix and the basis matrix, the sampling process is carried out by selecting some samples of the signal in its measurement domain. Therefore, by substituting the Eq.6.7 in the Eq.6.6, the sampled vector can be written as:

$$y = \Phi \Psi \times s + d \tag{6.8}$$

Where  $\Phi$  should be incoherent with  $\Psi$  and  $\Theta = \Phi \Psi$  with size  $M \times N$  is called the dictionary. The purpose of CS is to reconstruct the  $N \times 1$  sparse signal  $x$  from these  $M$  measurements ( $M < N$ ), although acquiring the  $s$  or equivalent  $x$  from  $y$  sampled vector is an ill-posed problem. According to the CS technique, a signal can be recovered by minimizing  $l_1$ -norm as described as follow:

$$\hat{x} = \underset{\tilde{x}}{\operatorname{argmin}} \|\tilde{x}\|_{l_1} \quad \text{such that} \quad \Phi \tilde{x} = y \quad (6.9)$$

### 6.3.1 Basis Matrix

The first CS stage for SAR imaging is to determine the measurement domain and the sparse domain of the signal. As mentioned previously, the relationship between these two domains can be determined by Basis matrix. In SAR imaging, the signal is sampled in the spatial-frequency domain which is achieved by a one-dimensional vector. The sparse signal is considered by a one-dimensional  $x$  vector. The Basis matrix  $\Psi$  can be obtained from the relationship between  $s$  and  $x$ . Hence, the  $\Psi$  matrix can be represented as [51]:

$$s = \Psi x \quad (6.10)$$

The selection of the appropriate basis matrix is one of the important concepts in the CS, where the echo signal is sparse, even though the presence of noise and clutter is considered. Generally, there are different basis matrices with the different characteristics for various applications such as discrete Fourier transform (DFT), Fast Fourier transform (FFT), and Waveform families. It is noteworthy that, designing an appropriate waveform plays the main role in forming a suitable dictionary in the CS theory for the received signal in radar [48]. Wavelets families are described in below.

#### 6.3.1.1 Wavelet Families

Several families of wavelets which are used for Basis matrix are presented in the following [56, 57]:

- Haar
- Daubechies
- Biorthogonal
- Coifflets
- Symlets Discrete Meyer

**Haar:** Any debate of wavelets starts with Haar wavelet, the first and simplest type. The Haar wavelet is discontinuous and resembles a step function which is shown in Figure 6.1.

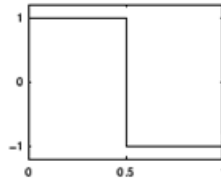


Figure 6.1: Haar wavelet shape

**Daubechies:** One of the most important wavelets is called compressed orthogonal wavelets which are indicated by  $dbN$ . Where  $N$  is the order, and  $db$  the "surname" of the wavelet. The significant point is that the  $db1$  wavelet is the same as Haar wavelet. Figure 6.2 illustrates the picture of all Daubechies wavelet families.

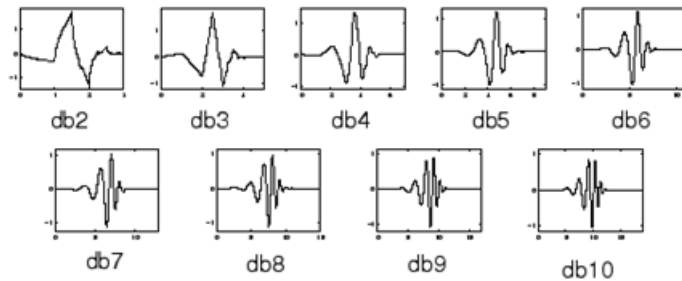


Figure 6.2: Daubechies wavelet families

**Biorthogonal:** This family of wavelets has a linear phase property that is needed to reconstruct the signal and image. They are shown in Figure 6.3. Using the two wavelets, one for decomposing (left side) and the other for reconstruction (right side), instead of the same single one.

**Coiflets:** The Coiflet wavelet function shows the disappearance or degradation time. In  $coifN$ ,  $N$  is the number of vanishing for both the wavelet and scaling functions. The Coif wavelet function has  $2N$  moments equal to 0 and the scaling function has  $2N - 1$  moments equal to 0. (Figure 6.4).



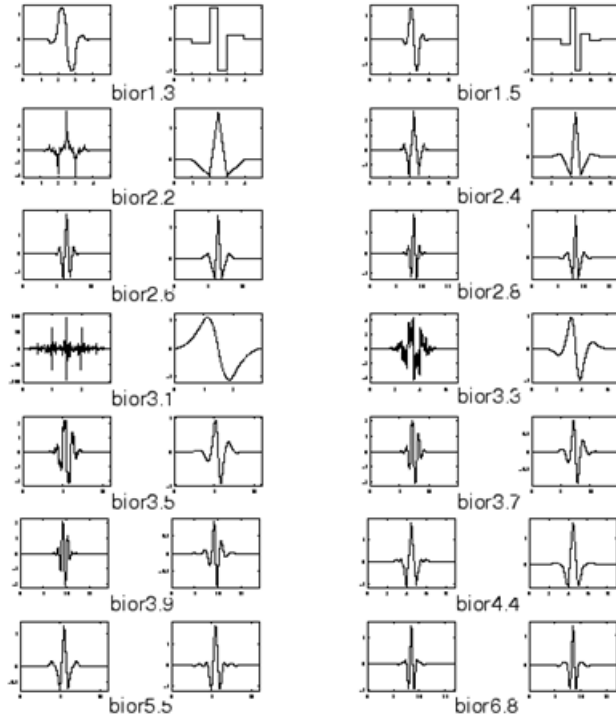


Figure 6.3: Biorthogonal Wavelet shape

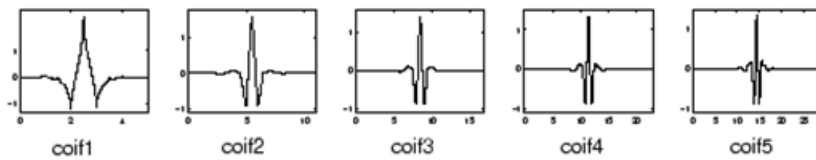


Figure 6.4: Coiflets Wavelet shape

**Symlets:** The symlets (Figure 6.5) are almost symmetrical wavelets suggested by Daubechies as modifications to the db family. The attributes of the two wavelet families are resembling.

**Discrete Meyer:** Figure 6.6 shows the Discrete Meyer wavelet. The Meyer wavelet is defined in the frequency domain.

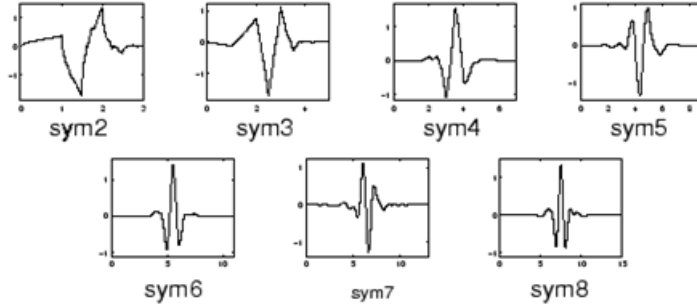


Figure 6.5: Symlets Wavelet shape

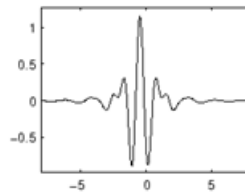


Figure 6.6: Meyer Wavelet shape

### 6.3.2 Measurement Matrix

Selecting the measurement matrix is the second important stage of CS. This is essential because the measurement matrix should be incoherent with the sparse basis matrix. Two different sampling schemes which can be used in radar measurements are depicted in Figure 6.7. The horizontal axis represents the antenna position along the tracking line. The blue box shows the selected measurement data to be used in the CS processing. The first sampling layout which is generated by a random matrix is shown in Figure 6.7(a), where the measurement points and antenna position points are randomly selected. It should be noted that the random matrix is incoherent with any sparse basis with high probability. On the other hand, by using this sampling layout the number of the measurement points is not significantly decreased, even if the number of data is extremely reduced. It is desirable since in a radar system, decreasing the measurement point is more important for decreasing the data acquisition time, mainly in a 2D scanning. Figure 6.7(b) shows the second sampling layout which is generated by selecting the specific positions for antennas along the tracking line when only these places

are allowed, to select the measurement points. This layout shows good results as well as a significant reduction in the acquisition time. This sampling layout has two advantages. First, the number of measurement points can be remarkably decreased. Second, the equipment implementation will be simpler. Contents are one of the remarkable features of the measurement matrix. There are two digits: ‘1’ and ‘0’, when ‘1’ shows the value for the selecting sample and ‘0’ in the other mode. The measurement process is accomplished by multiplying the sampling matrix  $\Phi$  by both sides of Eq.6.10, when the measurement matrix  $\Phi$  is a two-dimensional matrix. According to the CS theory, the multiplication between  $\Phi$  and  $\Psi$  gives a two-dimensional matrix which is  $\Theta = \Phi\Psi$ , it is named the dictionary, with size  $M$ . where  $M$  indicates the selected samples data and  $N$  indicates all antenna positions [53].

$$\Phi s_m = \Phi\Psi x_m \tag{6.11}$$

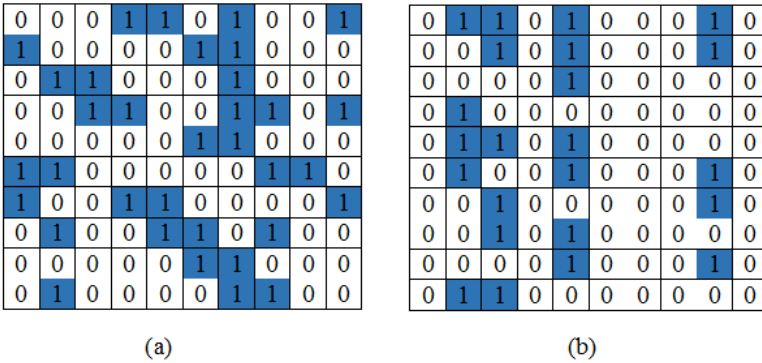


Figure 6.7: sampling matrix in CS

### 6.3.3 Compressive Sensing Recovery Algorithm

In the CS theory, the purpose is to reconstruct  $N \times 1$  sparse signal  $x$  from these  $M$  measurements. Although acquiring  $s$  or equivalent  $x$  from the sampled vector,  $y$ , is an ill-posed problem because of  $M < N$ . According to the CS theory, it can be solved by solving a convex optimization problem while  $x$  is sparse. Various reconstruction algorithms can be used in Compressive

Sensing. The first reconstruction algorithm is classical optimization-based which is called  $l_1$ -norm and the second one is a greedy reconstruction algorithm which is called Orthogonal Matching Pursuit (OMP) [58].

### 6.3.3.1 $l_1$ -Minimization

$l_1$ -norm algorithm recovers the signal by solving the convex optimization problem by using:

$$\hat{s} = \operatorname{argmin} \|\tilde{s}\|_{l_1} \quad \text{such that} \quad \Theta \tilde{s} = y \quad (6.12)$$

Where  $\|\hat{s}\|_{l_1} = \sum_{i=1}^N |s_i|$ . Eq.6.12 is reliable in noiseless measurements. In SAR application there are noise and clutter, therefore the noise parameter must be considered in the problem. In noisy case, the sampled vector  $y$  is determined in Eq.6.6 and  $l_1$ -norm is defined as follow:

$$\hat{s} = \operatorname{argmin} \|\tilde{s}\|_{l_1} \quad \text{such that} \quad \|y - \Theta \tilde{s}\|_{l_2}^2 \leq \beta^2 \quad (6.13)$$

Where  $l_2$ -norm is defined as  $\|s\|_{l_2} = \sqrt{\sum_{i=1}^N s_i^2}$ . The residual term  $y = \Theta \tilde{s}$  must be small. It is worth noting that solving the  $l_1$ -norm problem via convex optimization produces computational complexity [53, 59].

### 6.3.3.2 Orthogonal Matching Pursuit (OMP)

The algorithms based on convex optimization, such as  $l_1$ -norm, has computational complexity, Therefore other algorithms which are not based on convex optimization has been proposed, such as Greedy pursuit algorithms or orthogonal matching pursuit (OMP). OMP creates an approximation by going through an iterative process which is faster and easier than convex optimization. In the OMP, the nonzero elements of  $x$  are recovered consecutive at each iteration, where the approximation of the signal  $x$  is initialized by  $x = 0$ . Suppose that  $s$  is a  $k$ -sparse signal of  $x$  with length  $N$ .  $\Phi$  is referred to a measurement matrix with a size of  $M \times N$ , where its columns are  $\Phi_d$  when  $d = 1, \dots, N$ . The sampled vector  $y = \Phi x$  is  $M$ -dimensional. It should be noted that a signal recovery is a problem that leads to a sparse approximation. Therefore, if the signal  $x$  has just  $k$ -nonzero elements, it is possible to say that the sampled vector  $y$  is a linear composition of  $k$ -columns of  $\Phi$  matrix. It means that according to the sparse approximation concept,

$s$  vector has  $k$ -term representation over the  $\Phi$  matrix. To recognize the ideal signal  $s$ , we need to distinguish which columns of  $\Phi$  take part in the sampled vector  $y$ . In the OMP algorithm, for each iteration, there is a most strongly correlated column of  $\Phi$  with  $y$ . After that, its contribution to  $y$  is reduced and the same process is applied to the residual iteratively. The OMP expresses that, after  $k$ -iteration, the correct set of columns of  $(\varphi_d^i s)$  will be recognized. The OMP algorithm is described as the following algorithm:

*OMP Algorithm:*

*INPUT:*

- \*  $t$ = Iteration number
- \*  $k$ = Sparsity level of the signal  $x$
- \*  $\Phi$  = An  $M \times N$  measurement matrix
- \*  $y$ = An  $M$ -dimensional sampled vector

*OUTPUT:*

- \*  $\hat{x}$ = Estimate of the signal  $x$
- \*  $\Phi_t$ = The matrix of chosen columns
- \*  $A_k$ = An index set of  $k$  elements from  $\{1, \dots, N\}$
- \*  $a_k$ = An  $M$ -dimensional approximation of the sampled data  $y$
- \*  $r_k = y - a_k$ = An  $M$ -dimensional residual vector

*INITIAL VALUES:*

Suppose the initial values are as follows

- \*  $t = 1$
- \*  $A_k = \emptyset$
- \*  $\Phi_0 = \emptyset$
- \*  $r_0 = y$

*METHOD:*

1. Find the index that solves the simple optimization problem such as  $\lambda_t$ , when it represented the column of  $\Phi$  which is most strongly correlated with the residual  $r_{t-1}$ .

$$\lambda_t = \operatorname{argmax}_{d=1,\dots,N} |\langle r_{t-1}, \varphi_d \rangle| \quad (6.14)$$

2. Augment the index set and the matrix of chosen columns.

$$A_t = A_{t-1} U \{ \lambda_t \} \quad (6.15)$$

$$\Phi_t = [\Phi_{t-1} \varphi_{\lambda_t}] \quad (6.16)$$

3. Solving a least squares problem to acquire a new signal estimation:

$$x_t = \operatorname{argmin}_{\hat{x}} \|y - \Phi_t \hat{x}\|_{l_2} \quad (6.17)$$

4. Calculating the new approximation of the sampled data to define the new residual.

$$a_t = \Phi_t x_t \quad (6.18)$$

$$r_t = y - a_t \quad (6.19)$$

5. By increasing  $t$ , return to step 1 and it will continue with a new iteration until  $t < k$ .

It is worth noting that, the residual  $r_t$  is orthogonal to columns of the matrix  $\Phi_t$ . For each new iteration ( $t$ ), when the residual of the prior iteration ( $t-1$ ) is nonzero, a new column of  $\Phi$  is selected and the matrix  $\Phi_t$  has full column degree (it means that it has independent columns). Hence, the signal estimate  $x_t$ , which is a solution in Step 4, is unique. Therefore, the approximation  $a_t$  and the residual  $r_t$  are unique. At the end of the algorithm, the estimate  $\hat{x}$  of the signal  $x$  has nonzero input at the elements listed in the index set  $A_t = A_k$ , since  $t = k$  is the last iteration [60].

#### 6.4 Compressive Sensing Applied To Radar

Since large bandwidth is used more frequently by modern radar systems, they need to use a high sampling rate, hence, in many cases, these systems include phased array configurations with a large number of transmitter-receiver components. Conversely, often the ultimate aim of a radar system is to approximate only a finite number of target parameters. In this way, there is an attempt to find a better solution for using radar signal acquisition, as well as processing with fewer data and power requirement. Recently, the compressive sensing (CS) as a means of reducing the acquisition time or obtaining a better efficiency with a decreased set of measurements has attracted the interest of many researchers in various fields. The present study reports one of the applications of compressive sensing in remote sensing and radar systems. In radar system, compared with the conventional techniques, CS is able to obtain a more accurate range-Doppler resolution. However, CS needs to use a suitable sparse signal, to design a measurement system, and to implement a suitable signal recovery method [48].

#### 6.5 Implementation of Compressive Sensing to SAR Imaging

In SAR system, the radar signal transmits an electromagnetic wave to the target and records the reflected signal from the target in the tracking area. Along the tracking line, the SAR process is carried out at various observation points. In traditional processing, the distance between each observation points has a sufficient agreement with the Nyquist criterion. The received signal from the target with reflection coefficient  $\sigma$  is as follows:

$$E_r = \sigma A e^{-j2kr} \tag{6.20}$$

Where  $A$  is the amplitude of the back scattered signal,  $k$  is propagation constant, and  $r$  is the two-way distance from the Tx and Rx antennas to the target. For a CWSF radar signal, the back scattered signal is acquired at several frequencies points. The received signal at  $m$ -th frequency point is:

$$E_r(m) = \sigma A e^{-j2k_m r} = \sigma A e^{-j \frac{4\pi}{c} f_m r} \tag{6.21}$$

In CWSF radar, the data is obtained at various observation points along the tracking line. The radar moves along an x-axis in the orthogonal direction

with respect to the range resolution. Therefore, SAR data is acquired along the x-axis. The echo signal is obtained at both spatial and frequency domain and it is represented by complex numbers as follows:

$$E(m, i) = I_{m,i} + jQ_{m,i} \tag{6.22}$$

Where  $I$  indicates the in-phase and  $Q$  indicates the quadrature components of the received signal for each  $f_m$  frequency and for each  $i$  antenna position. The SAR data can be focused to achieve radar image of a target which is located at point  $p$  as follow:

$$I(p) = \frac{1}{N_p N_f} \sum_{i=1}^{N_p} \sum_{m=1}^{N_f} E_{i,m} e^{\frac{4\pi}{c} f_m R_i} \tag{6.23}$$

Where  $N_f$  is the number of frequencies and  $N_p$  is the number of positions of the radar antenna and  $c$  is the speed of light. The distance between the target  $p$  and  $i$  position of antenna is  $R_i$  Eq.6.20 requires a lot of processing time. Therefore, CS can be applied to the radar system to use only a few samples. In this case, CS is a possible technique to decrease the acquisition time which promises to speed up the radar acquisition. Compressive sensing, however, is a new approach asserts that it can reconstruct signals from a small number of random measurements data better than the traditional way [51].

### 6.6 The radar prototype

The GB-SAR prototype which is assembled for testing is shown in Figure 6.8. The radar operates step-by-step both in frequencies and position. The radar head moves on a rail along a horizontal plane.

A vector network analyzer (VNA) HP8720D operated as transceiver providing a continuous wave stepped-frequency signal (CWSF) in X-band with central frequency  $f_c = 10 \text{ GHz}$  and bandwidth  $B_w$ . With respect to Figure 6.9 the VNA output power was  $0 \text{ dBm}$ , the one-way cable loss was  $-5 \text{ dB}$ , TX amplifier gain was  $10 \text{ dB}$ . The RX receiver gain was  $20 \text{ dB}$ . Two RF cables linked the VNA to the front end moving along the horizontal mechanical axis. Two single pole double-throw (SPDT) switches provided a direct path between the transmitter and the receiver in order to perform the calibrated measurements. The aim of the calibration is to avoid the movements of the



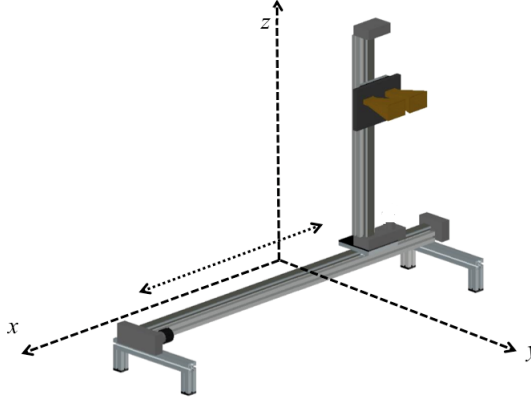


Figure 6.8: Sketch the GB-SAR prototype

cables could affect the phase of the measurement. The antennas are two equal horns linearly polarized, with a rectangular aperture  $5.5\text{ cm} \times 7.5\text{ cm}$ , designed for operating in the band  $8 - 12\text{ GHz}$ . A Band Pass Filter in the same band defines the noise bandwidth. Finally, a Low Pass Filter at the end of the receiver chain cuts possible harmonic frequencies that amplifiers can introduce.

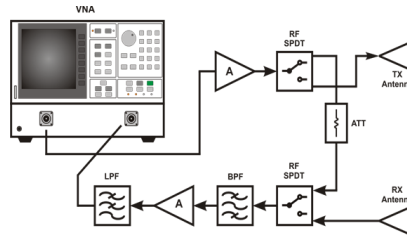


Figure 6.9: Block scheme of radar front-end

### 6.7 The CS Theory and Focusing Algorithm

For applying the CS, a pattern of  $N_m$  antennas has been selected randomly from the x-axis of the echo matrix. For each frequency, the sampled vector  $y$  is as follows:

$$y = \Phi E \tag{6.24}$$

Where  $E$  is a vector  $N_x \times 1$  taken from the echo matrix and  $\Phi$  is a random matrix, the values of which are between 0 and 1. The  $\Phi$  matrix is a measurement matrix with the size of  $M \times N_x$ . The non-zero elements are selected randomly for each row of the measurement matrix from the allowed position of the antenna pattern along x-line. The vector  $E$  is represented as a sparse signal which is determined in the measurement domain by Basis matrix  $\Psi$  with size  $N_x \times N_x$  according to Eq.6.25. The  $\Psi$  is called the Basis where it is generated by two types of Transform.

$$E = \Psi s \tag{6.25}$$

First, the basis is  $\Psi = fft(I)$ , where  $fft(.)$  is the Fast Fourier Transform and  $I$  is the  $N_x \times N_x$  identity matrix, the second one is  $\Psi = haar(I)$ , where the  $haar(.)$  is a wavelet type transformation. The  $s$  is  $N_x \times 1$ , which is the vector of weighting coefficients. By substituting Eq.6.24 and Eq.6.25 the sampled vector would be:

$$y = \Theta s \tag{6.26}$$

Where  $\Theta = \Phi\Psi$  is a  $M \times N_x$  matrix. The vector  $E$  has to be reconstructed from the sampled vector, but since a vector of length  $N_x$  is sampled with a set of  $M$  measurement ( $M < N_x$ ), it is generated normally an ill-posed problem. The orthogonal matching pursuit (OMP) and  $l_1$ -norm algorithms can be solved this problem. After reconstruction, the data have been focused by using an Inverse Fast Fourier transform that considers the electromagnetic path between the radar and any image point [27].

### 6.8 Experimental Test

Investigation of the CS algorithm in real scenario was carried out based on three different data. The first test was carried out with a corner reflector (CR) in front of the radar. Figure 6.10 shows the radar equipment which was installed in the garden at University of Florence. A corner reflector of 0.5 m side was placed on a tripod in front of the radar.

The radar parameters are listed in Table 6.1.



Figure 6.10: Picture of Experimental Environment

Table 6.1: Radar parameter in the first test

$B_w$	$L_x$	$N_x$	$N_f$	$F_{min}$	$F_{max}$
155 MHz	1.8 m	180	801	9.915 GHz	10.075 GHz

Figure 6.11 displays the obtained image without CS. Figure 6.12 and Figure 6.13 show the results with a compression of 50% and 30% with their  $\Phi$  measurement matrix when *Haar* wavelet transform is used as basis matrix and  $l_1$ -norm algorithm is applied for the recovery method.

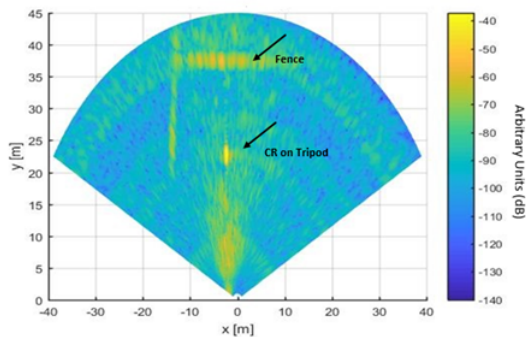


Figure 6.11: Monostatic image of CR without CS

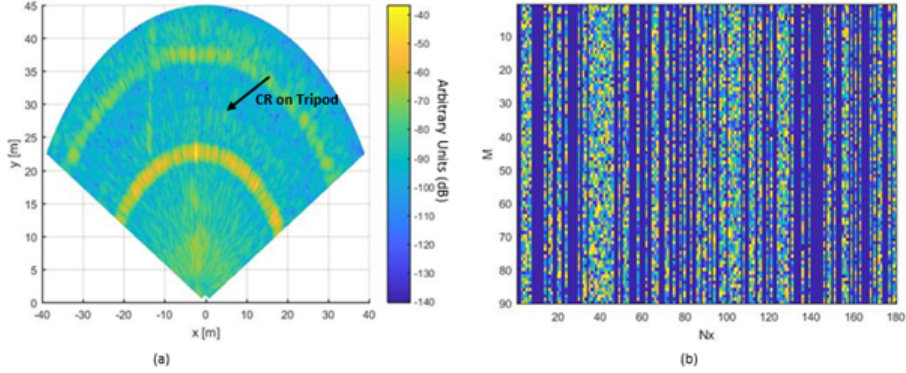


Figure 6.12: Monostatic image of CR (a) radar image using 50% of the antennas' position (b) the pattern of  $\Phi$  Haar wavelet with  $l_1$ -norm

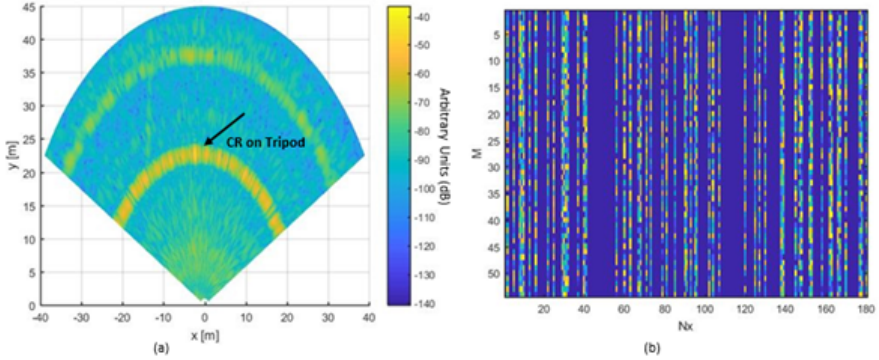


Figure 6.13: Monostatic image of CR (a) radar image using 30% of the antennas' position (b) the pattern of  $\Phi$  Haar wavelet with  $l_1$ -norm

The Peak Signal Noise Ratio ( $PSNR$ ) was measured in two cases, it was  $PSNR_{50\%} = 28.32 \text{ dB}$  and  $PSNR_{30\%} = 21.27 \text{ dB}$ .

Figure 6.14 shows the monostatic image of CR when Haar wavelet transformation is used for the basis matrix and  $OMP$  is used for recovering the signal with a compression of 50% and 30%.

In this case, the measured  $PSNR$  was  $PSNR_{50\%} = 28.19 \text{ dB}$  and  $PSNR_{30\%} = 21.41 \text{ dB}$ .

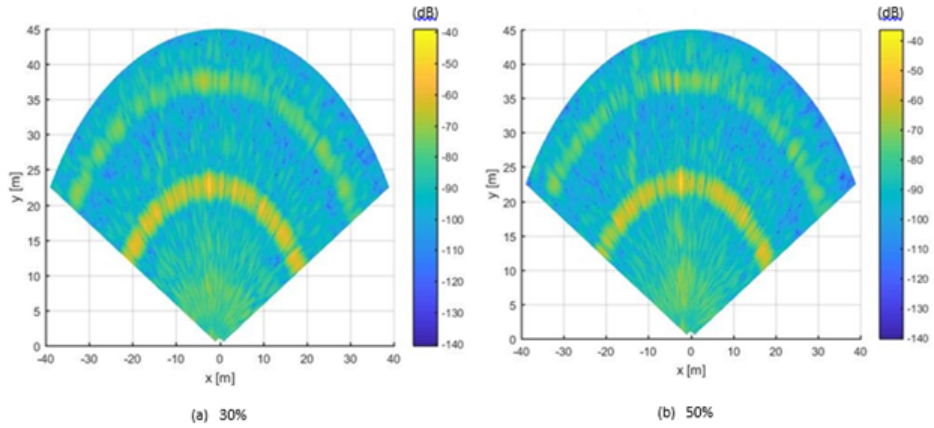


Figure 6.14: Monostatic image of CR (a) using 30% of the antennas' position (b) using 50% of the antennas' position- *Haar* wavelet with *OMP*

Figure 6.15 and Figure 6.16 show the monostatic image of CR when *FFT* transformation is used for basis matrix and  $l_1$ -norm and *OMP* are used for recovering the signal respectively, with a compression of 50% and 30%.

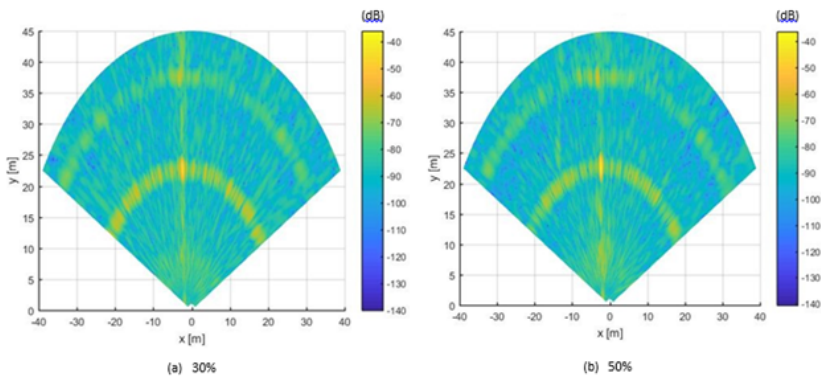


Figure 6.15: Monostatic image of CR (a) using 30% of the antennas' position (b) using 50% of the antennas' position- *FFT* with  $l_1$ -norm

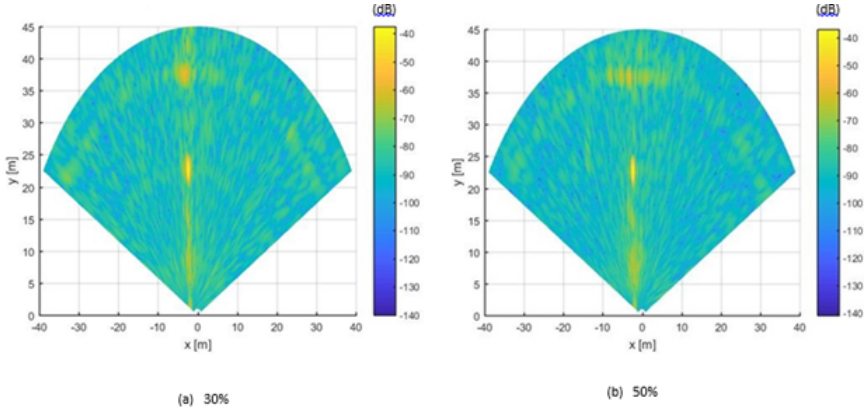


Figure 6.16: Monostatic image of CR (a) using 30% of the antennas' position (b) using 50% of the antennas' position- *FFT* with *OMP*

The *PSNR* was  $PSNR_{50\%} = 34.32 \text{ dB}$  and  $PSNR_{30\%} = 28.07 \text{ dB}$  in case of  $l_1$ -norm algorithm and  $PSNR_{50\%} = 38.87 \text{ dB}$  and  $PSNR_{30\%} = 37.13 \text{ dB}$  in case of *OMP* algorithm.

By considering the obtained images of the CS theory, the CR is visible in each image, but it is not possible to recognize the shape of the fence. It is worth mentioning that the result achieved by applying *FFT* and *OMP* for recovering the signal are more satisfactory.

For estimating interferogram, the Corner Reflector on the tripod is moved along the view direction by using a micrometric positioner with  $0.1 \text{ mm}$  accuracy. Figure 6.17 shows the measured and the nominal displacement of the corner reflector during 20 acquisitions.

Figure 6.18 shows the measured displacement of the corner reflector by using 50% and 30% compression data and no-CS, respectively. As can be seen, the movements without compressive sensing, with 50% and 30% of antennas' position are almost similar. As shown in Figure 6.19, the mean error was  $0.2 \text{ mm}$  for CS using 30%.

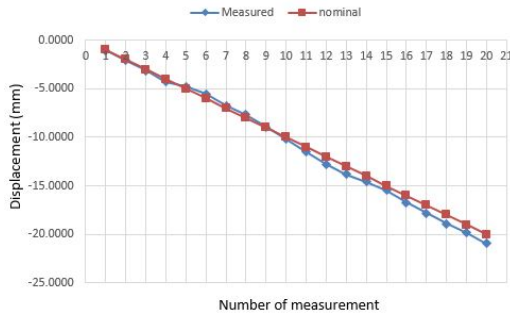


Figure 6.17: Measured and nominal displacement of the CR on the tripod without using CS

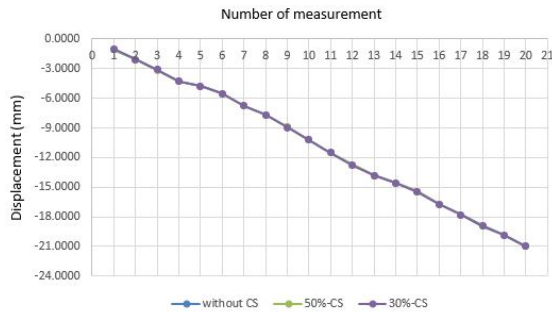


Figure 6.18: Measured displacement of the CR on the tripod without using CS and using 50% and 30% the antennas' position

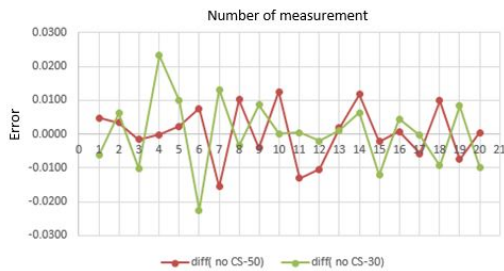


Figure 6.19: An error of movement without using CS and using 50% and 30% of the antennas' position

In order to assess the CS in a more realistic scenario, the second test was accomplished for a seven-storey building. The distance between the radar and building was 140 m. Figure 6.20 shows the view of the building which is presented also in the previous chapter. The radar parameters are listed in Table 6.2.

The monostatic image of the building without compressive sensing is shown in Figure 6.21. The facade of the building is visible by a clear slant line.

Table 6.2: Radar parameter in the second test

$B_w$	$L_x$	$N_x$	$N_f$	$F_{min}$	$F_{max}$
80 MHz	1.5 m	150	401	9.915 GHz	10.075 GHz



Figure 6.20: Picture of building

Figure 6.22 and Figure 6.23 show the results with a compression of 50% and 30% of data, when *Haar* wavelet transform is used for the basis matrix and  $l_1$ -norm and *OMP* algorithms are applied for recovering the signal.



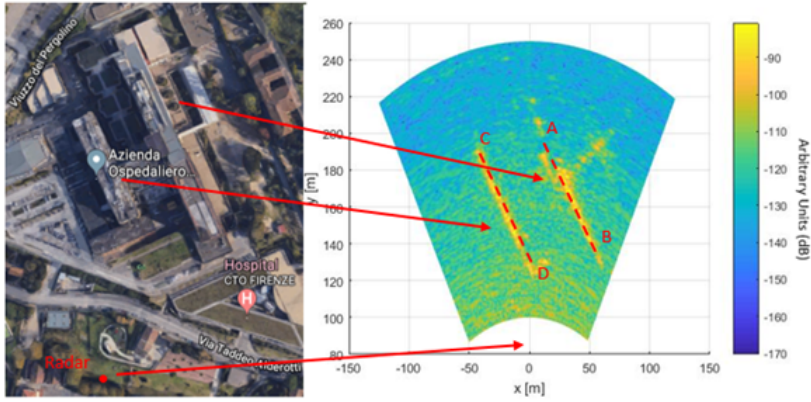


Figure 6.21: Monostatic image of building without CS

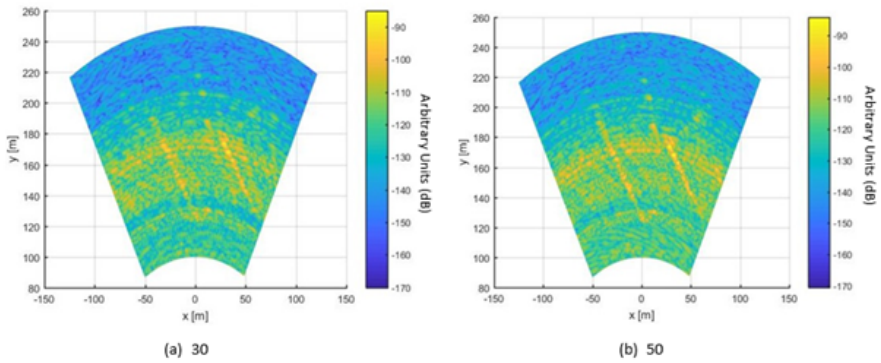


Figure 6.22: Monostatic image of building (a) using 30% of the antennas' position (b) using 50% of the antennas' position- *Haar* wavelet with  $l_1$ -norm

When *Haar* wavelet is used for the basis and  $l_1$ -norm is recovery algorithm the  $PSNR_{50\%} = 22.7332 \text{ dB}$  and  $PSNR_{30\%} = 19.0007 \text{ dB}$  and when *OMP* is used for recovering the signal the  $PSNR_{50\%} = 21.5877 \text{ dB}$  and  $PSNR_{30\%} = 18.4278 \text{ dB}$ .

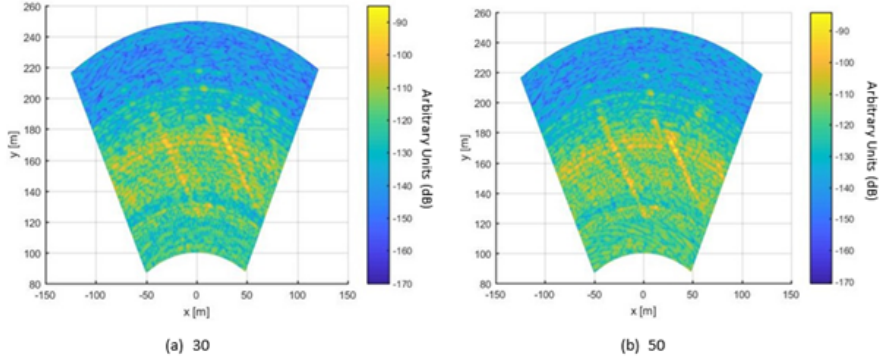


Figure 6.23: Monostatic image of building (a) using 30% of the antennas' position (b) using 50% of the antennas' position- Haar wavelet with OMP

Figure 6.24 and Figure 6.25 show the results with a compression of 50% and 30% of data when  $FFT$  is transform and  $l_1$ -norm and OMP algorithms are applied for the recovery method. The  $PSNR$  was measured, when  $FFT$  is a basis matrix, the  $PSNR$  was  $PSNR_{50\%} = 15.6193 \text{ dB}$  and  $PSNR_{30\%} = 9.3301 \text{ dB}$  in case of  $l_1$ -norm algorithm and the  $PSNR_{50\%} = 10.7188 \text{ dB}$  and  $PSNR_{30\%} = 1.8038 \text{ dB}$  in case of OMP algorithm.

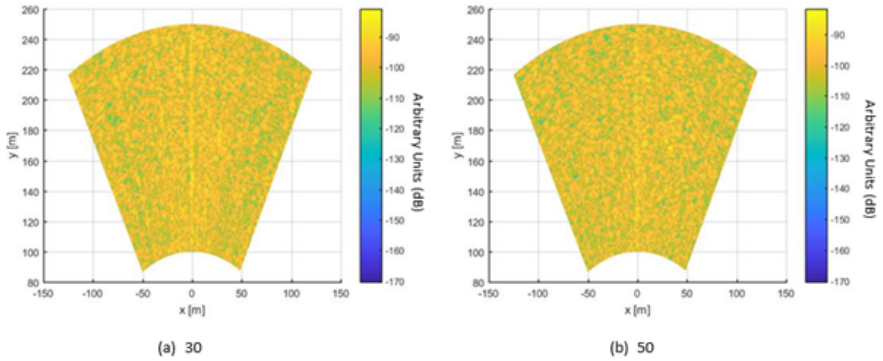


Figure 6.24: Monostatic image of building (a) using 30% of the antennas' position (b) using 50% of the antennas' position-  $FFT$  with  $l_1$ -norm

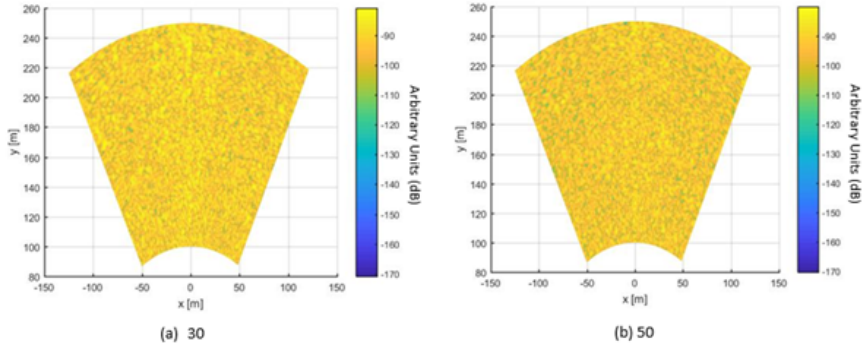


Figure 6.25: Monostatic image of building (a) using 30% of the antennas' position (b) using 50% of the antennas' position-*FFT* with *OMP*

By considering the obtained images of the building with compressive sensing, it should be noted, when the target has a distributed shape, *Haar* wavelet transform provides a better result than *FFT*. It means that selecting a proper basis matrix and effective retrieval method contributes to the quality of good images. Hence, an exhaustive study was carried out on the wavelets families, *FFT* and *DCT*, when they consider as a basis matrix. The results were recovered by three different methods. Table 6.3 and Table 6.4 show the results of *PSNR* by using 30% and 50% compression of the antennas' position, respectively.

<i>CS</i>	$L_1$ (dB)	$L_2$ (dB)	$OMP$ (dB)
dct	11.0409	10.8544	5.9259
fft	9.3301	9.977	1.8038
haar	19.0007	19.0007	18.4278
db2	18.3384	18.3224	18.8452
db3	18.1307	18.1314	18.8593
db4	17.8392	17.8302	17.8478
db5	17.9132	17.9262	19.119
db6	17.9147	17.9149	18.9843
db7	17.7919	17.7541	18.4877
db8	14.6955	14.6972	16.1694
db9	17.0459	17.0401	16.3172
db10	17.0337	17.051	17.6907
bior1.3	18.7818	18.786	17.5756
bior2.2	18.1309	18.1303	18.2721
bior2.6	17.6715	17.6782	18.5815
bior3.1	20.1043	20.1017	19.1599
bior3.5	17.4931	17.5359	17.3313
bior3.9	17.7734	17.7989	16.4458
bior5.5	17.8045	17.831	19.1065
coif1	18.3339	18.3409	17.9571
coif2	17.8489	17.8487	17.8594
coif3	18.2984	18.2988	18.735
coif4	17.8651	17.894	18.8879
coif5	18.0039	17.9991	18.6603
sym2	18.3384	18.3224	18.8452
sym3	18.1307	18.1314	18.8593
sym4	18.1545	18.2596	17.9977
sym5	17.838	17.8171	18.7612
sym6	17.4721	17.4448	18.0388
sym7	17.2217	17.2236	18.3354
sym8	16.9046	16.9292	17.8637
legall5.3	18.0609	18.0636	18.4653
dmey	17.4611	17.4615	16.9531

Table 6.3: Compressive Sensing Table of using 30% of the antennas' position for building

<i>CS</i>	$L_1$ (dB)	$L_2$ (dB)	$OMP$ (dB)
dct	16.4694	16.5898	8.1905
fft	15.6193	15.3028	10.7188
haar	22.7332	22.7332	21.5877
db2	21.4979	21.5236	22.7824
db3	21.6060	21.6154	22.7174
db4	21.5545	21.5751	20.9904
db5	21.0083	21.0168	21.6048
db6	20.8953	20.8962	21.3903
db7	20.4838	20.5181	20.6709
db8	19.1624	19.1747	19.1508
db9	19.1131	19.1339	17.8064
db10	19.8216	19.8292	19.2719
bior1.3	22.2686	22.2724	21.4909
bior2.2	21.9067	21.9161	22.4213
bior2.6	21.3160	21.3181	22.3640
bior3.1	21.2703	21.3071	20.5589
bior3.5	20.1213	20.1241	19.6286
bior3.9	20.7904	20.8029	19.4132
bior5.5	22.1297	22.1372	22.7607
coif1	21.7780	21.7641	21.7434
coif2	21.9786	21.9567	21.9029
coif3	21.7671	21.7713	21.7665
coif4	20.2061	20.2107	21.8819
coif5	21.3760	21.3770	21.6747
sym2	21.4979	21.5236	22.7824
sym3	21.6060	21.6154	22.7174
sym4	21.4512	21.4376	21.1772
sym5	21.3588	21.3771	20.1905
sym6	21.1219	21.1189	20.9575
sym7	21.7925	21.8042	21.5175
sym8	21.4652	21.4690	20.0479
legall5.3	22.0343	22.0382	22.6399
dmey	20.5452	20.5902	19.1599

Table 6.4: Compressive Sensing Table of using 50% of the antennas' position for building

The last study was to test the theory of CS in a natural scenario. The radar test was conducted on the "Belvedere Glacier" during the summer of 2006. The Belvedere Glacier, east face of Monte Rosa has been investigated several times due to the threat of outburst of Glacier in the Macugnaga village. Figure 5.25 shows the picture of Belvedere Glacier with the radar line of sight highlighted. The measurement performed with the aim of assessing the reliability of a C-band ground-based SAR (GB-SAR) interferometer to monitor an Alpine glacier reported in [32,61–63]. The radar parameters are listed at table 6.5.

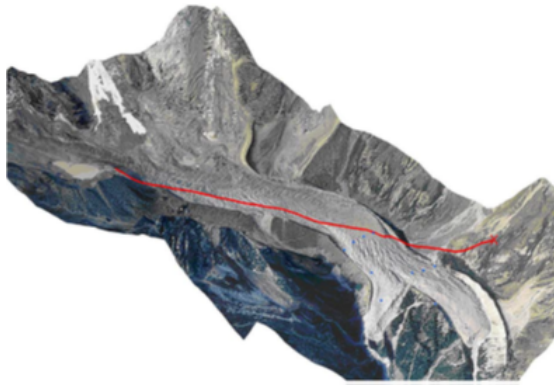


Figure 6.26: Picture of Belvedere Glacier with the radar line of sight highlighted [61–63]

Table 6.5: Radar parameter in the third test

$B_w$	$L_x$	$N_x$	$N_f$	$F_{min}$	$F_{max}$
20 MHz	1.7 m	141	801	5.97 GHz	5.99 GHz

The radar equipment was placed on the left side of the glacier's valley, just above the moraine, at 2000 m. Figure 6.27 shows the SAR instrumentation, the observed area and a power supply system for generating electricity for the radar system, which is consisted of solar panels, wind generators, and batteries.



Figure 6.27: The radar equipment: on the left side of the GB-SAR system, on the right side of the solar and wind power supply system [61]

Figure 6.28 displays one of the many monostatic radar images that have been acquired during the radar measurements, which are utilized for doing interferogram.

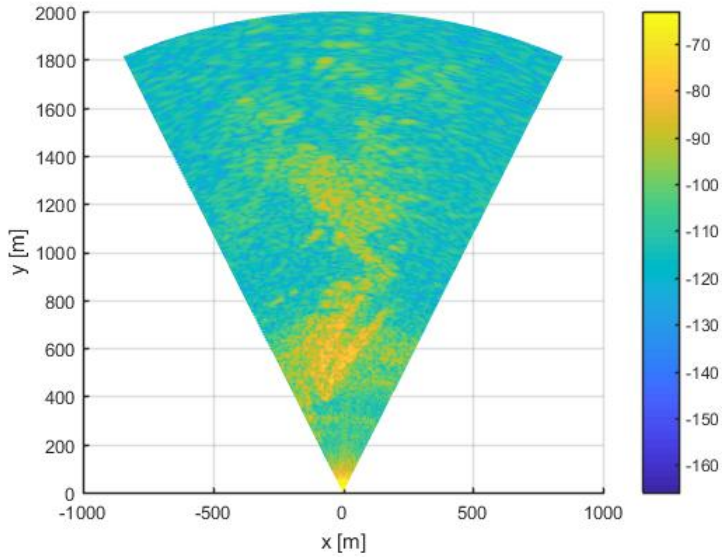


Figure 6.28: Monostatic image of Belvedere Glacier

In order to use the compressive sensing, a small part of the observation area was investigated. The range was between 350 *m* to 1000 *m*. The azimuth is limited between ‘65’ *deg* and ‘115’ *deg*. The monostatic image of the Belvedere Glacier in the mentioned zone without compressive sensing is shown in Figure 6.29. Since the basis matrix of the CS is an identity matrix, only 128 samples of the scan line of GB-SAR were used (Figure 6.29).

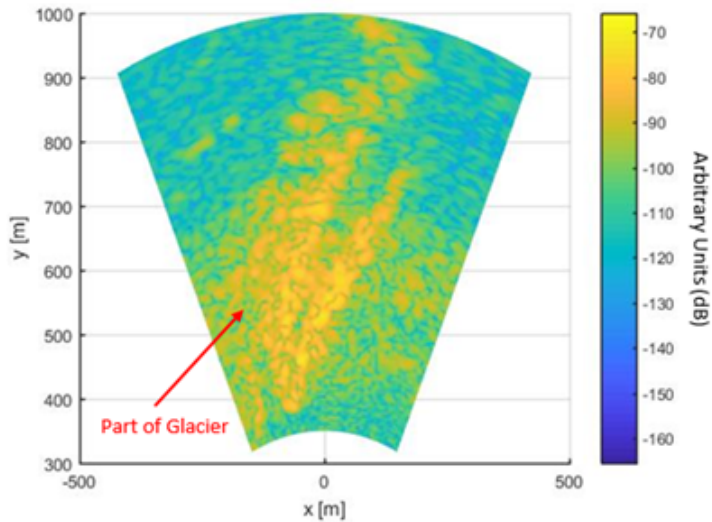


Figure 6.29: Monostatic image of Glacier without CS

Figure 6.30 and Figure 6.31 show the results with a compression of 50% and 30% of data when *Haar* wavelet transform is used as basis matrix and  $l_1$ -norm and *OMP* algorithms are applied for recovering the signal.

Figure 6.32 and Figure 6.33 show the results with a compression of 50% and 30% of the antennas’ position ,when *FFT* transform is used and  $l_1$ -norm and *OMP* algorithms are applied for recovering the signal.

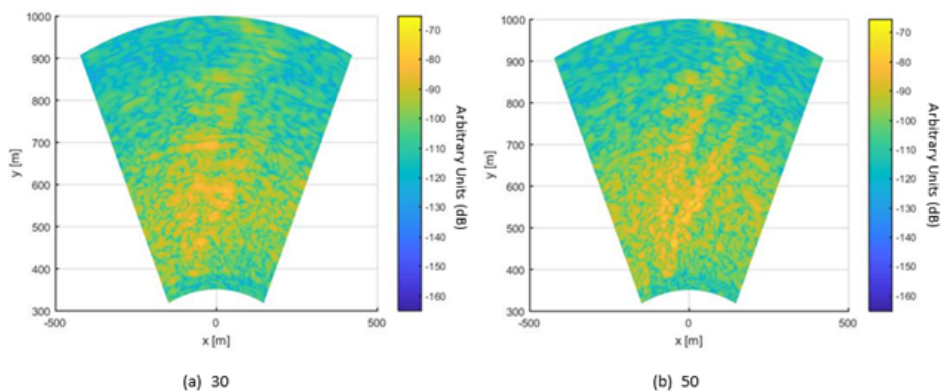


Figure 6.30: Monostatic image of Glacier (a) using 30% of the antennas' position (b) using 50% of the antennas' position- *Haar* wavelet with  $l_1$ -norm

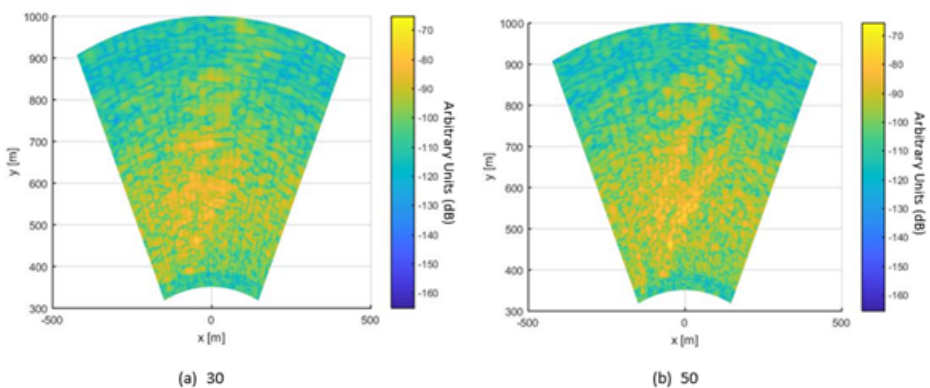


Figure 6.31: Monostatic image of Glacier (a) using 30% of the antennas' position (b) using 50% of the antennas' position- *OMP*



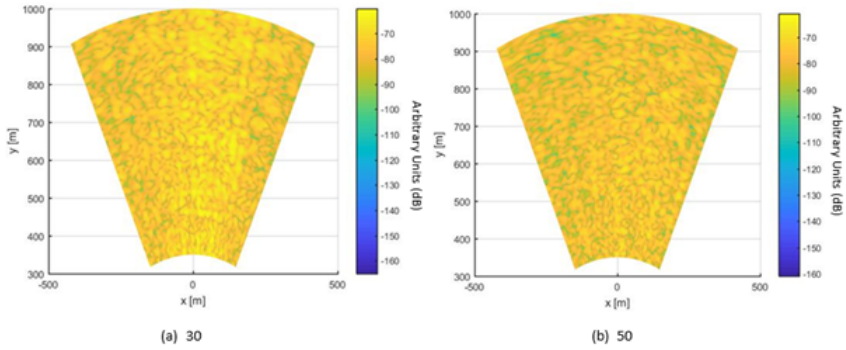


Figure 6.32: Monostatic image of Glacier (a) using 30% of the antennas' position (b) using 50% of the antennas' position- *FFT* with  $l_1$ -norm

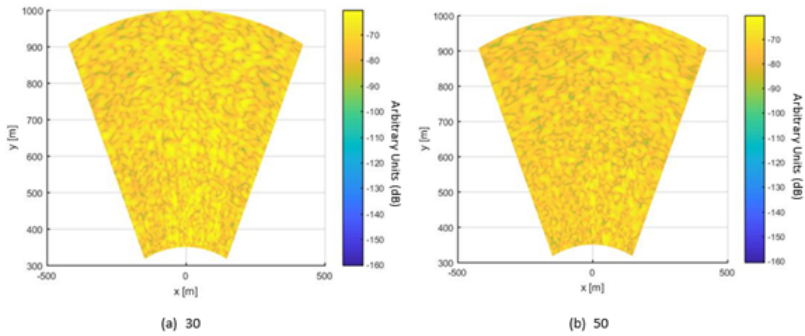


Figure 6.33: Monostatic image of Glacier (a) using 30% of the antennas' position (b) using 50% of the antennas' position- *FFT* with *OMP*

Table 6.6. and Table 6.7. show the results of *PSNR* of this data by using 30% and 50% compression of data respectively.

<i>CS</i>	$L_1$ (dB)	$L_2$ (dB)	<i>OMP</i> (dB)
dct	1.3383	1.3920	0.2054
fft	-5.0873	-4.9257	-4.0629
haar	15.0919	15.0209	16.5230
db2	8.2055	8.2636	14.0875
db3	5.6429	5.7500	14.0233
db4	8.7495	8.7473	8.5646
db5	7.1667	7.1900	10.5339
db6	3.7929	3.8632	11.7711
db7	8.6767	8.6749	5.5842
db8	1.7835	1.7672	0.9231
db9	5.5266	5.5185	-3.2285
db10	-2.9625	-2.9017	2.1600
bior1.3	11.4541	11.4091	8.5745
bior2.2	9.9317	9.9232	13.9860
bior2.6	6.9107	7.0118	13.0361
bior3.1	7.4951	7.4648	8.4639
bior3.5	7.2054	7.2095	10.6511
bior3.9	6.0756	6.5284	7.5641
bior5.5	4.1123	4.0862	14.0159
coif1	10.5841	10.6132	14.2655
coif2	7.9847	7.9911	14.5470
coif3	6.5554	6.5566	10.1588
coif4	5.7573	5.7538	11.5725
coif5	9.4924	9.4931	3.4222
sym2	8.2055	8.2636	14.0875
sym3	5.6429	5.7500	14.0233
sym4	10.0979	10.0955	14.0254
sym5	4.8284	4.5095	3.6331
sym6	7.3665	7.3655	7.3665
sym7	2.4419	2.4464	11.3972
sym8	6.9995	7.0009	11.3443
legall5.3	9.4305	9.3954	14.6227
dmey7	5.6006	5.6074	11.7809

Table 6.6: Compressive Sensing Table of using 30% of the antennas' position for Glacier

<i>CS</i>	$L_1$ (dB)	$L_2$ (dB)	<i>OMP</i> (dB)
dct	-2.2605	-3.5027	-2.7650
fft	-1.6705	1.8543	-0.9232
haar	20.5339	20.5339	21.1556
db2	13.5283	13.5273	19.2770
db3	9.5444	9.5442	18.8316
db4	4.0529	4.0960	13.0510
db5	5.5569	5.6934	11.1427
db6	2.8945	2.8718	17.5110
db7	11.2636	11.2413	10.6683
db8	2.6221	2.6412	8.8252
db9	6.6917	6.7429	10.2514
db10	2.3173	2.3313	3.2894
bior1.3	13.9569	13.9521	10.2678
bior2.2	14.3683	14.3948	19.1659
bior2.6	9.8380	9.8647	18.1534
bior3.1	6.6547	6.6425	5.1604
bior3.5	4.8110	4.8134	2.9276
bior3.9	3.3077	3.2704	-3.0073
bior5.5	10.5554	10.5197	14.6206
coif1	10.9854	11.1096	19.7177
coif2	12.1661	12.1605	19.6570
coif3	9.4757	9.4762	18.7172
coif4	11.6506	11.6483	14.4558
coif5	5.8691	5.8791	11.3583
sym2	13.5283	13.5273	19.2770
sym3	9.5444	9.5442	18.8316
sym4	11.1430	11.1869	17.3890
sym5	9.5243	9.5132	9.7779
sym6	12.4844	12.4941	12.9386
sym7	9.3514	9.3729	16.8559
sym8	13.6382	13.5881	12.1787
legall5.3	11.7616	11.7891	15.7480
dmey	6.8303	6.8385	10.7182

Table 6.7: Compressive Sensing Table of using 50% of the antennas' position for Glacier

Figure 6.34 depicts an interferometric map obtained through a C-band GB-SAR to analyse the glacier dynamics. Figure 6.35, Figure 6.36 and Figure 6.37 show the interferometric map with a compression of 100% and 50% and 30%.

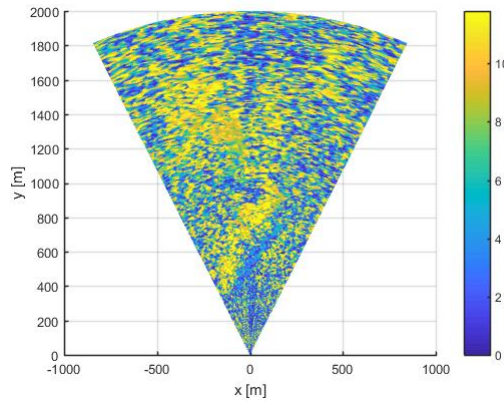


Figure 6.34: Interferometric map of the glacier without using CS

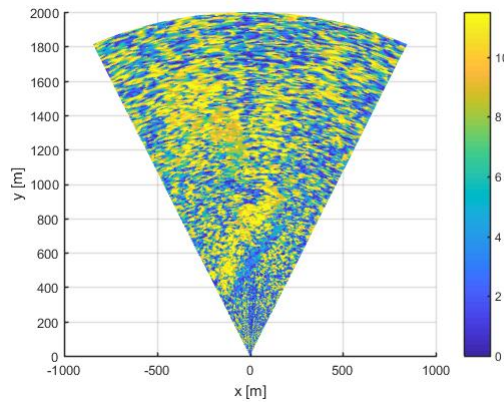


Figure 6.35: Interferometric map of the glacier by using 100% of the antennas' position

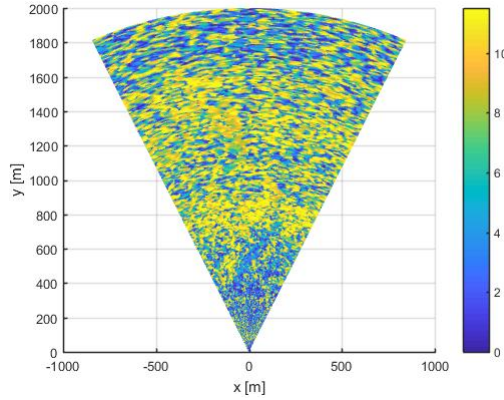


Figure 6.36: Interferometric map of the glacier by using 50% of the antennas' position

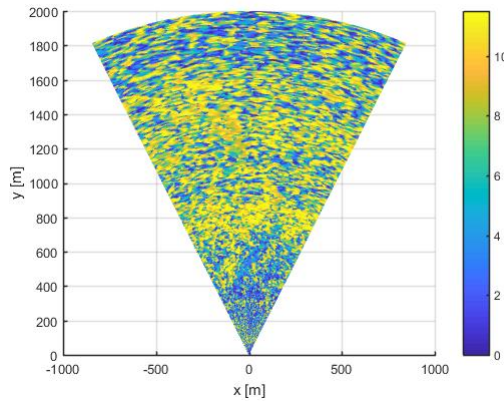


Figure 6.37: Interferometric map of the glacier by using 30% of the antennas' position

In order to verify the ability of the CS to detect a displacement, a small area inside the glacier slider was considered. Figure 6.38 shows the obtained plots without CS and applied CS with 100%, 50% and 30% of the data. As can be seen, the movements without using compressive sensing, with 100%, 50% and 30% of antennas' position are almost similar. Figure 6.39 shows the mean error of displacement in both case of without CS and using CS

algorithm. It was 0.95 mm for CS using 30%.

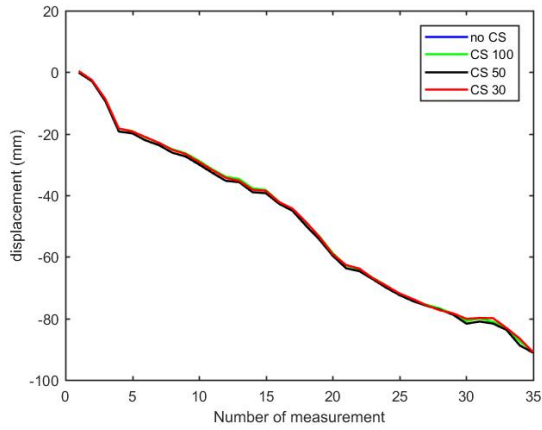


Figure 6.38: Measured displacement of a small area inside the glacier

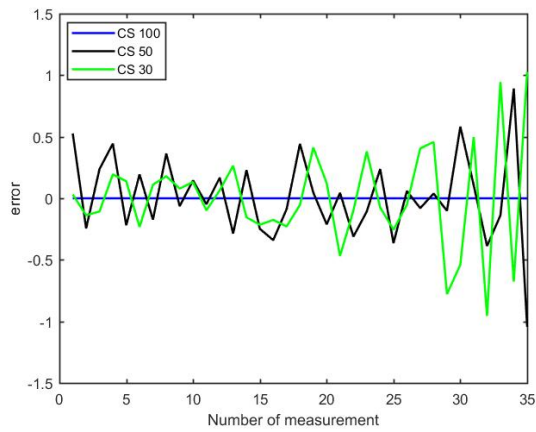


Figure 6.39: An error of movement of glacier without using CS and using 100%, 50% and 30% of the antennas' position

## 6.9 Conclusion

In this study, the CS technique is investigated in different scenarios. By testing different kinds of base matrices and different recovery methods, a remarkable result is that the CS technique is able to reconstruct SAR images in good quality ( $PSNR > 20$  dB) only using 30% of data. Another significant result is that the plot of displacement recovered using 100%, 50% and 30% of data is almost similar to the plot which is obtained without the CS method. These results are the starting point to design multi-band input and multi-band output radar (MIMO), which is able to use the CS techniques.

# Chapter 7

## Conclusion

This chapter summarizes the main contributions of the thesis that led to innovation in radar configurations and radar processing methods. It introduces some related topics for future research.

The RCS measurements of a toy and a professional quadcopter have been provided. The interest in the accurate estimation of the radar cross section (RCS) distribution of drones is owing to their serious threat to flights safety these days. It should be noted that, design specifications of some anti-drone radars consider at least RCS of  $0.01m^2$ , whilst this is about 30% of the average RCS of toy drone that we measured. This drone is the smallest size of the drone in the market. On the other hand, a professional quadcopter has an RCS at least ten times larger than a toy drone. A remarkable result of measured RCS of two drones is that the mean value of RCS in the vertical and horizontal polarization is approximately equal. It is worth mentioning that, the Swerling distribution is in good agreement with the RCS statistical distribution of the drones that we tested, besides the simulated results are compatible with experimental results.

The Inverse Synthetic Aperture Radar (ISAR) is a powerful and well-established technique for obtaining both 2D and 3D images of the radar target. Hence, a 2D and 3D ISAR processing has also been developed for drone imaging, the obtained images of which are clear and recognizable so that the parts of drones can

be identified. Unfortunately, the side lobes of the point spread function (PSF) can spoil the ISAR images sharply. Use of the aperture window is a way to reduce the effect of this distortion. Aperture windowing is performed by using a summation of the ISAR images relative to 4 arcs of  $180^\circ$ . In this way, the ripple due to the cross-range lobes can be removed.

A novel Ground-based Synthetic Aperture Radar (GBSAR) system which is able to acquire both monostatic and bistatic images is also presented. A bistatic radar technique by means of a moving transponder was employed to obtain high-resolution 3D bistatic SAR images in long times (several hours). The same system simultaneously obtains 2D monostatic images in short times (about a half-hour). The 3D capability is suitable for imaging of targets in complex scenarios, where the altitude along the z-axis is not an unambiguous function of the (x,y) plane. It is worth mentioning that this recent radar configuration is obtained as an upgrade of a linear monostatic GBSAR, and the suggested imaging technique can be used for interferometry in each horizontal plane.

Another significant achievement of this thesis is to provide a compression method of data acquisition. Therefore, compressive sensing (CS) is presented as a possible technique for speeding up the acquisition time. In other words, the CS approach could reduce the number of acquisition points, and the measurement time by using only a random pattern of the antennas positions. In this thesis, the CS technique is investigated in different scenarios. By testing different kinds of base matrices and different recovery methods, a significant result is that the CS technique is able to reconstruct SAR images in good quality ( $PSNR > 20dB$ ) using only 30% of data. Moreover, the displacement measured by applying 100%, 50% and 30% of the data is equal to the result without using the CS method.

In the upcoming researches, the aim is to design a multi-input and multi-output radar (MIMO) with the ability to use compressive sensing to speed up the acquisition and computation time.



# Appendix A

## Publications

This research activity has led to several publications in international journals and conferences. These are summarized below.<sup>1</sup>

### International Journals

1. Pieraccini M., **Rojhani N.**, Miccinesi L., “Compressive Sensing for Ground Based Synthetic Aperture Radar”, Remote Sensing, 2018.
2. Pieraccini M., Miccinesi L.,**Rojhani N.** “A GBSAR Operating in Monostatic and Bistatic Modalities for Displacement Vector”, IEEE Geoscience and Remote Sensing Letters, July 2017.
3. Pieraccini M., Miccinesi L., **Rojhani N.** “RCS and ISAR of small UAVs”, IEEE Aerospace and Electronic Systems Magazine, September 2017

### International Conferences and Workshops

1. **Rojhani N.**, Pieraccini M., Sarbazi Golazari S., “A Compact TEM Horn Antenna for Ground Penetrating Radar”, IEEE ICACCI-18 IEEE International Conference on Advances in Computing, Communications Informatics,2018.
2. Pieraccini M.,**Rojhani N.**, Miccinesi L., “Ground Based Synthetic Aperture Radar with 3D Imaging Capability”, 15th European Radar Conference, EuRAD-2018.

---

<sup>1</sup>The author’s bibliometric indices are the following:  $H$ -index = 3, total number of citations = 21 (source: Google Scholar on Month 12, 20118).

3. Miccinesi L., **Rojhani N.**, Pieraccini M., “Compressive Sensing for No-Contact 3D Ground Penetrating Radar”, 2018 41st International Conference on Telecommunications and Signal Processing (TSP), Athens, Greece, August-2018.
4. Pieraccini M., **Rojhani N.**, “Testing of bridges and towers through interferometric radar”, 3rd International and 7th National Conference on Modern Materials and Structures in Civil Engineering, Iran-2018.
5. Pieraccini M., Miccinesi L., **Rojhani N.**, “Comparison between Horn and Bow-tie Antennas for Through-the-Wall Applications”, 2018 IEEE Conference on Antenna Measurements Applications (CAMA)-2018.
6. Pieraccini M., Miccinesi L., **Rojhani N.**, “A free-space technique for measuring the complex dielectric constant of sawdust”, 2018 IEEE Conference on Antenna Measurements Applications (CAMA)-2018.
7. **Rojhani N.**, Sarbazi Golazari S., Nasrin Amiri., Farrokh Hojjat Kashani., “CPW-Fed Circular Polarized Square Slot Antenna for GPS Applications”, 2018 IEEE International RF and Microwave Conference (RFM)-2018.
8. Pieraccini M., **Rojhani N.**, Miccinesi L., “Comparison between horn and bow-tie antennas for Ground Penetrating Radar”, 9th international workshop on advanced ground penetrating radar, IWAGPR 2017, July 2017.
9. Pieraccini M., **Rojhani N.**, Miccinesi L., “2D and 3D-ISAR Images of a Small Quadcopter”, 14th European Radar Conference, EuRAD 2017.
10. Pieraccini M., **Rojhani N.**, Miccinesi L., “Ground Penetrating Radar with Contact Horn Antennas”, proceeding at 32nd URSI GASS, Montreal, August 2017, conference abstract.
11. Sarbazi Golazari S., **Rojhani N.**, Amiri N., “Multiband low profile printed monopole antenna for future 5G wireless application with DGS”, 2017 IEEE 4th International Conference on Knowledge-Based Engineering and Innovation (KBEL), December 2017.

### Patent

1. Radar ad apertura sintetica basato a terra (GBSAR) con antenne multiple in trasmissione e ricezione (MIMO) e facente uso della tecnica di elaborazione detta Compressive Sensing (CS), [numero di brevetto per invenzione : n. 10201800006797].
2. Radar Terrestre Tridimensionale Interferometrico ad Apertura Sintetica, [numero di brevetto per invenzione : n.102017000145769].

## Bibliography

- [1] M. I. Skolnik, “Introduction to radar,” *Radar handbook*, vol. 2, 1962.
- [2] M. A. Richards, J. Scheer, W. A. Holm, and W. L. Melvin, *Principles of modern radar*. Citeseer, 2010.
- [3] B. R. Mahafza, *Radar Systems Analysis and Design Using MATLAB Second Edition*. Chapman and Hall/CRC, 2005.
- [4] R. J. Sullivan, “Microwave radar: Imaging and advanced concepts(book),” *Norwood, MA: Artech House, Inc, 2000.*, 2000.
- [5] G. T. Ruck, D. E. Barrick, W. D. Stuart, and C. K. Krichbaum, *Radar Cross Section Handbook. Volumes 1 & 2*. Plenum Press, New York, 1970.
- [6] J. J. Crispin, *Methods of radar cross-section analysis*. Elsevier, 2013.
- [7] K. F. Warnick and W. C. Chew, “Convergence of moment-method solutions of the electric field integral equation for a 2-d open cavity,” *Microwave and Optical Technology Letters*, vol. 23, no. 4, pp. 212–218, 1999.
- [8] C. Ozdemir, *Inverse synthetic aperture radar imaging with MATLAB algorithms*, vol. 210. John Wiley & Sons, 2012.
- [9] J. Crispin and A. Maffett, “Radar cross-section estimation for simple shapes,” *Proceedings of the IEEE*, vol. 53, no. 8, pp. 833–848, 1965.
- [10] A. Wessling, “Radar target modelling based on rcs measurements,” 2002.
- [11] M. Soumekh, *Synthetic aperture radar signal processing*, vol. 7. New York: Wiley, 1999.
- [12] J. Curlander and R. McDonough, “Synthetic aperture radar (vol. 396),” 1991.
- [13] V. Chen and M. Martorella, “Inverse synthetic aperture radar,” *Scitech Publishing 2014, and references therein*, 2014.
- [14] W. G. Carrara, “Soptlight synthetic aperture radar,” *Signal Processing Algorithms*, 1995.
- [15] C.-c. Chen and H. C. Andrews, “Multifrequency imaging of radar turntable data,” *IEEE Transactions on Aerospace and Electronic Systems*, no. 1, pp. 15–22, 1980.

- [16] C.-C. Chen and H. C. Andrews, "Target-motion-induced radar imaging," *IEEE Transactions on Aerospace and Electronic Systems*, no. 1, pp. 2–14, 1980.
- [17] Z. Zhu and Z. She, "One-dimensional isar imaging of multiple moving targets," in *Aerospace and Electronics Conference, 1994. NAECON 1994., Proceedings of the IEEE 1994 National*, pp. 171–174, IEEE, 1994.
- [18] J. C. Stover, *Optical scattering: measurement and analysis*, vol. 2. SPIE optical engineering press Bellingham, 1995.
- [19] Y. Zhong-cai, S. Jia-ming, and W. Jia-chun, "Validity of effective-medium theory in mie scattering calculation of hollow dielectric sphere," in *Antennas, Propagation & EM Theory, 2006. ISAPE'06. 7th International Symposium on*, pp. 1–4, IEEE, 2006.
- [20] U. Brummund and B. Mesnier, "A comparative study of planar mie and rayleigh scattering for supersonic flowfield diagnostics," in *Instrumentation in Aerospace Simulation Facilities, 1999. ICIA SF 99. 18th International Congress on*, pp. 42–1, IEEE, 1999.
- [21] T.-H. Chu, D.-B. Lin, and Y.-W. Kiang, "Microwave diversity imaging of perfectly conducting object in the close near-field region," in *Antennas and Propagation Society International Symposium, 1989. AP-S. Digest*, pp. 82–85, IEEE, 1989.
- [22] R. Bhalla and H. Ling, "Isar image formation using bistatic data computed from the shooting and bouncing ray technique," *Journal of electromagnetic waves and applications*, vol. 7, no. 9, pp. 1271–1287, 1993.
- [23] D. R. Wehner, "High resolution radar," *Norwood, MA, Artech House, Inc., 1987, 484 p.*, 1987.
- [24] D. L. Mensa, "High resolution radar cross-section imaging," *Boston, MA, Artech House, 1991, 280 p.*, 1991.
- [25] M. Pieraccini, D. Tarchi, H. Rudolf, D. Leva, G. Luzi, G. Bartoli, and C. Atzeni, "Structural static testing by interferometric synthetic radar," *NDT & E International*, vol. 33, no. 8, pp. 565–570, 2000.
- [26] M. Pieraccini, F. Papi, and S. Rocchio, "Sar imagery by rotosar," in *Microwaves, Communications, Antennas and Electronic Systems (COMCAS), 2015 IEEE International Conference on*, pp. 1–5, IEEE, 2015.
- [27] M. Pieraccini and L. Miccinesi, "Arcsar: Theory, simulations, and experimental verification," *IEEE Transactions on Microwave Theory and Techniques*, vol. 65, no. 1, pp. 293–301, 2017.
- [28] C. A. Wiley, "Pulsed doppler radar methods and apparatus," July 20 1965. US Patent 3,196,436.

- [29] I. G. Cumming and F. H. Wong, "Digital processing of synthetic aperture radar data; artech house," *Inc.: Norwood, MA, USA*, 2005.
- [30] G. Franceschetti and R. Lanari, *Synthetic aperture radar processing*. CRC press, 2018.
- [31] K. Takahashi, M. Matsumoto, and M. Sato, "Continuous observation of natural-disaster-affected areas using ground-based sar interferometry," *IEEE Journal of Selected Topics in Applied Earth Observations and Remote Sensing*, vol. 6, no. 3, pp. 1286–1294, 2013.
- [32] G. Luzi, M. Pieraccini, D. Mecatti, L. Noferini, G. Macaluso, A. Tamburini, and C. Atzeni, "Monitoring of an alpine glacier by means of ground-based sar interferometry," *IEEE Geoscience and Remote Sensing Letters*, vol. 4, no. 3, pp. 495–499, 2007.
- [33] G. Luzi, L. Noferini, D. Mecatti, G. Macaluso, M. Pieraccini, C. Atzeni, A. Schaffhauser, R. Fromm, and T. Nagler, "Using a ground-based sar interferometer and a terrestrial laser scanner to monitor a snow-covered slope: Results from an experimental data collection in tyrol (austria)," *IEEE Transactions on Geoscience and Remote Sensing*, vol. 47, no. 2, pp. 382–393, 2009.
- [34] V. T. Vu, D. N. Nehru, M. I. Pettersson, and T. K. Sjölgren, "An experimental ground-based sar system for studying sar fundamentals," in *Synthetic Aperture Radar (AP SAR), 2013 Asia-Pacific Conference on*, pp. 424–427, IEEE, 2013.
- [35] Q. Ul-Ann, "Bistatic synthetic aperture radar processing," 2014.
- [36] M. E. Davis, *Advances in bistatic radar*, vol. 2. SciTech Publishing, 2007.
- [37] S. Duque, P. López-Dekker, and J. J. Mallorqui, "Single-pass bistatic sar interferometry using fixed-receiver configurations: Theory and experimental validation," *IEEE Transactions on Geoscience and Remote Sensing*, vol. 48, no. 6, pp. 2740–2749, 2010.
- [38] Y. L. Neo, *Digital processing algorithms for bistatic synthetic aperture radar data*. PhD thesis, University of British Columbia, 2007.
- [39] D. V. Nezhlin, V. Kostylev, A. Blyakhman, A. Ryndyk, and A. Myakinkov, *Bistatic radar: principles and practice*. Wiley Online Library, 2007.
- [40] M. Jackson, "The geometry of bistatic radar systems," in *IEE Proceedings F (Communications, Radar and Signal Processing)*, vol. 133, pp. 604–612, IET, 1986.
- [41] Y. L. Neo, *Geometry and Processing Algorithms for Bistatic SAR-PROGRESS REPORT*. PhD thesis, The University of British Columbia, 2005.
- [42] M. Pieraccini and L. Miccinesi, "Bistatic ground-based synthetic aperture radar," in *EUSAR 2018; 12th European Conference on Synthetic Aperture Radar*, pp. 1–5, VDE, 2018.

- [43] R. Bamler and P. Hartl, “Synthetic aperture radar interferometry,” *Inverse problems*, vol. 14, no. 4, p. R1, 1998.
- [44] P. A. Rosen, S. Hensley, I. R. Joughin, F. K. Li, S. N. Madsen, E. Rodriguez, and R. M. Goldstein, “Synthetic aperture radar interferometry,” *Proceedings of the IEEE*, vol. 88, no. 3, pp. 333–382, 2000.
- [45] G. Krieger, H. Fiedler, and A. Moreira, “Bi-and multistatic sar: Potentials and challenges,” in *Proc. EUSAR*, vol. 34, pp. 365–370, 2004.
- [46] A. S. Goh, *Bistatic synthetic aperture radar data processing and analysis*. PhD thesis, 2012.
- [47] G. Luzi, M. Pieraccini, D. Mecatti, L. Noferini, G. Guidi, F. Moia, and C. Atzeni, “Ground-based radar interferometry for landslides monitoring: atmospheric and instrumental decorrelation sources on experimental data,” *IEEE transactions on geoscience and remote sensing*, vol. 42, no. 11, pp. 2454–2466, 2004.
- [48] M. A. Hadi, S. Alshebeili, K. Jamil, and F. E. A. El-Samie, “Compressive sensing applied to radar systems: an overview,” *Signal, Image and Video Processing*, vol. 9, no. 1, pp. 25–39, 2015.
- [49] E. J. Candès and M. B. Wakin, “An introduction to compressive sampling,” *IEEE signal processing magazine*, vol. 25, no. 2, pp. 21–30, 2008.
- [50] M. J. Pelgrom, “Analog-to-digital conversion,” in *Analog-to-Digital Conversion*, pp. 325–418, Springer, 2013.
- [51] R. Karlina, *Compressive sensing applied to high resolution imaging by synthetic aperture radar*. PhD thesis, Tohoku University, 2013.
- [52] Y. C. Eldar and G. Kutyniok, *Compressed sensing: theory and applications*. Cambridge University Press, 2012.
- [53] R. G. Baraniuk, “Compressive sensing [lecture notes],” *IEEE signal processing magazine*, vol. 24, no. 4, pp. 118–121, 2007.
- [54] E. Candes and J. Romberg, “Sparsity and incoherence in compressive sampling,” *Inverse problems*, vol. 23, no. 3, p. 969, 2007.
- [55] H. Markarian and S. Ghofrani, “High-tv based cs framework using map estimator for sar image enhancement,” *IEEE Journal of Selected Topics in Applied Earth Observations and Remote Sensing*, vol. 10, no. 9, pp. 4059–4073, 2017.
- [56] <https://it.mathworks.com>, “introduction-to-the-wavelet-families.”
- [57] L. Debnath, *Wavelets and signal processing*. Springer Science & Business Media, 2012.
- [58] S. Foucart and H. Rauhut, *A mathematical introduction to compressive sensing*, vol. 1. Birkhäuser Basel, 2013.

- 
- [59] X. X. Zhu and R. Bamler, "Tomographic sar inversion by  $l_1$ -norm regularization—the compressive sensing approach," *IEEE Transactions on Geoscience and Remote Sensing*, vol. 48, no. 10, pp. 3839–3846, 2010.
- [60] J. A. Tropp and A. C. Gilbert, "Signal recovery from random measurements via orthogonal matching pursuit," *IEEE Transactions on information theory*, vol. 53, no. 12, pp. 4655–4666, 2007.
- [61] D. Mecatti, L. Noferini, G. Macaluso, M. Pieraccini, G. Luzi, C. Atzeni, and A. Tamburini, "Remote sensing of glacier by ground-based radar interferometry," in *Geoscience and Remote Sensing Symposium, 2007. IGARSS 2007. IEEE International*, pp. 4501–4504, IEEE, 2007.
- [62] L. Noferini, D. Mecatti, G. Macaluso, M. Pieraccini, and C. Atzeni, "Monitoring of belvedere glacier using a wide angle gb-sar interferometer," *Journal of Applied Geophysics*, vol. 68, no. 2, pp. 289–293, 2009.
- [63] M. Pieraccini, L. Noferini, D. Mecatti, G. Macaluso, G. Luzi, and C. Atzeni, "Digital elevation models by a gbsar interferometer for monitoring glaciers: the case study of belvedere glacier," in *Geoscience and Remote Sensing Symposium, 2008. IGARSS 2008. IEEE International*, vol. 4, pp. IV–1061, IEEE, 2008.